

UC Santa Barbara

UC Santa Barbara Electronic Theses and Dissertations

Title

Remote Hydroacoustic and Infrasonic Detection and Characterization of Anak Krakatau Eruptive Activity Leading To, During, and Following the December 2018 Major Flank Collapse and Tsunami

Permalink

<https://escholarship.org/uc/item/8q91520w>

Author

Rose, Kaelynn

Publication Date

2020

Peer reviewed|Thesis/dissertation

University of California
Santa Barbara

**Remote Hydroacoustic and Infrasonic Detection and
Characterization of Anak Krakatau Eruptive
Activity Leading To, During, and Following the
December 2018 Major Flank Collapse and Tsunami**

A thesis submitted in partial satisfaction
of the requirements for the degree

Master of Science
in
Earth Science

by

Kaelynn Marie Rose

Committee in charge:

Professor Robin S. Matoza, Chair
Professor Toshiro Tanimoto
Professor Zachary Eilon

December 2020

The Thesis of Kaelynn Marie Rose is approved.

Professor Toshiro Tanimoto

Professor Zachary Eilon

Professor Robin S. Matoza, Committee Chair

December 2020

Remote Hydroacoustic and Infrasonic Detection and Characterization of Anak
Karakatau Eruptive Activity Leading To, During, and Following the December 2018
Major Flank Collapse and Tsunami

Copyright © 2020

by

Kaelynn Marie Rose

Acknowledgements

I would like to express my thanks and appreciation to the numerous people who have supported me and this work over the past two years. I would like to first thank my advisor, Professor Robin Matoza, for the opportunity to work on such an exciting project at UCSB, as well as his invaluable support and guidance throughout this process. This work would not have been possible without his mentorship, expertise, enthusiasm for volcanology and seismo-acoustics, and insightful suggestions at each fork in the road. I would also like to thank Professor Zach Eilon and Professor Toshiro Tanimoto for serving on my thesis committee, for their great questions and suggestions during seminars which encouraged me to dig deeper, and for their thoughtful feedback on this document.

This work was made possible by the Virtual Data Exploitation Centre (vDEC – <https://www.ctbto.org/specials/vdec>) platform of the CTBTO that allows access to IMS data for civilian and scientific applications. The views presented in this work are those of the authors and do not necessarily represent the views of the CTBTO or any other institution mentioned herein. This work was supported by NSF grant EAR-1847736 awarded to Matoza. This research used data from seismic network code IM (International Monitoring System) downloaded from the IRIS DMC (<http://www.iris.edu>). Data analysis and plotting included the use of ObsPy (Beyreuther et al., 2010), PMCC (Le Pichon et al., 2010) and GMT (Wessel & Smith, 1991). I gratefully acknowledge the European Space Agency (ESA) for the Sentinel-1 and Sentinel-2 satellite imagery datasets. Thank you to the Earth Research Institute (ERI) for the use of their high-performance computing systems.

I am grateful to my fellow geophysics graduate students, especially Rodrigo de Negri for sharing his knowledge, helping me download mountains of data, and for being an unparalleled seismology TA, Richard Sanderson for his heroic PMCC and code debug-

ging help, as well as Sean Maher and Hugo Ortiz for suggestions and office chalkboard conversations which undoubtedly made this research better. I would also like to thank my other geophysics office-mates, Aaron Anderson, Scott Condon, Jon Petruska, Jiong Wang, and Han Xiao for their constant help and advice, and for all of the laughs in the office.

I would also like to express my thanks and appreciation to Peter Green for his fearless technical support, Yann Ricard for his guidance through the graduate program process, and the rest of the UCSB Earth Science Department staff and faculty for helping make my two years at UCSB successful and enjoyable.

I am also grateful to my fellow UCSB Earth Science graduate students, whose friendship and camaraderie made my experience at UCSB wonderful, whether we were doing research, taking classes, going to the beach or to trivia nights, or just hanging around the department.

Finally, I would like to thank all of my friends and family for their unwavering support. To Nick, for his continuous love, encouragement, and confidence in me, and for listening to my enthusiastic commentary about the rocks on every hike. To my brother, Aaron, for going adventuring with me. To my parents, Janet and David, for supporting me in every endeavor, motivating me to study science, and teaching me to love the natural world. Thank you for everything you have done that helped me climb this mountain.

Abstract

Remote Hydroacoustic and Infrasonic Detection and Characterization of Anak Krakatau Eruptive Activity Leading To, During, and Following the December 2018 Major Flank Collapse and Tsunami

by

Kaelynn Marie Rose

Eruptions at submarine and partially submerged volcanoes are often difficult to detect, yet pose a significant hazard to coastal populations, ships, and aircraft. Hydroacoustic and infrasonic waves generated by explosive eruptions can propagate thousands of kilometers in atmospheric and oceanic waveguides. We employ a selection of remote moored hydroacoustic (H08S, 3,307 km; H01W, 3,720 km) and infrasonic (IS06, 1,156 km; IS07, 3,475 km; IS52, 3,638 km) stations of the International Monitoring System (IMS) to investigate the new eruptive phase of Anak Krakatau volcano in the Sunda Strait of Indonesia which began in June 2018. A climactic eruption phase on 22 December 2018 triggered the collapse of the southwest flank and summit, generating a large tsunami which struck the coastlines of Sumatra and Java [Global Volcanism Program, 2019]. We perform array processing for a new eruptive phase from June 2018 through January 2019, using the Progressive Multi-Channel Correlation (PMCC) algorithm. Coherent explosive eruption (co-eruptive) signals arriving from the back-azimuth of Anak Krakatau were recorded at two infrasound stations (IS06, 1,156 km and IS52, 3,638 km) of the IMS network during the main eruption phase and flank collapse, but were not detected hydroacoustically. We also investigate intermittent infrasound signal from smaller eruptive activity prior to the flank collapse and tsunami. The signals of interest are associated between the two stations and correspond to eruption reports from

the Indonesian Center for Volcanology and Geological Disaster Mitigation (PVMBG). We detect a 12-day swarm of hydroacoustic signals starting 24 days before the main collapse event that were part of the sustained eruptive sequence at Anak Krakatau, recorded at IMS hydroacoustic station H08S (3,307 km) and partially recorded at station H01W (3,720 km). We interpret an evolution in signal content in the weeks directly preceding the climactic eruption phase, as resulting from intermittent subaerial (infrasonic) and submarine (hydroacoustic) detections, to entirely subaerial content at the start of the climactic phase. We perform waveform cross-correlation and clustering analysis to assess the similarity of infrasound events and the similarity of hydroacoustic events, grouping similar events into families for each signal type. Infrasonic events recorded during the main infrasound-generating eruption phase are similar (with 61.8% of events assigned to the largest 4 event families using a threshold ρ of 0.65), indicating repetitive explosions at Anak Krakatau from the same source mechanism and similar long-range propagation conditions. Hydroacoustic event families are less similar, indicating a possible range of submarine eruption processes and signal types occurring at Anak Krakatau including submarine explosions, bursting magmatic gas bubbles, or shallow volcanic earthquakes. This study underscores the potential of using remote acoustic technology to detect and characterize eruptions at submarine or partially submerged volcanoes.

Contents

Abstract	vi
1 Introduction	1
2 Background and Motivation	3
2.1 Infrasound Propagation	4
2.2 Hydroacoustic Propagation	7
2.3 The International Monitoring System Network	13
2.4 Anak Krakatau Geologic Setting and Eruption History	16
2.5 Anak Krakatau 2018-2019 Eruptive Activity	18
3 Array Processing and Spectrogram Analysis	21
3.1 The PMCC Method	21
3.2 Infrasound Data and Chronology	22
3.3 Hydroacoustic Data and Chronology	33
3.3.1 Infrasound and Hydroacoustic Signal Comparison	41
3.3.2 Marine Seismic Survey Clutter	43
3.3.3 A Check of the PMCC Method	45
4 Waveform Cross Correlation and Clustering	47
4.1 Infrasound Waveform Similarity	48
4.1.1 Infrasound Event Selection	48
4.1.2 Infrasound Event Cross-Correlation	53
4.1.3 Infrasound Event Clustering	54
4.1.4 Discussion	60
4.2 Hydroacoustic Waveform Similarity	62
4.2.1 Hydroacoustic Event Selection	62
4.2.2 Hydroacoustic Event Cross-Correlation	64
4.2.3 Hydroacoustic Event Clustering	65

4.2.4	Hydroacoustic Envelopes	71
4.2.5	Discussion	74
5	Conclusion	81

Introduction

Eruptions at submarine volcanoes or partially submerged volcanoes (i.e., volcanoes which rise from the seafloor where some part of the upper volcanic edifice has emerged above the sea surface as an island) are often difficult to detect and observe, due to their remoteness and the challenges of working in a submarine environment. Yet, these eruptions can pose a significant hazard to coastal populations, ships and aircraft. Hydroacoustic and infrasound monitoring are emerging as useful tools for studying submarine or partially submerged volcanic eruptions, as acoustic waves can travel thousands of kilometers in ocean and atmospheric waveguides [Ewing and Worzel, 1948; Munk, 1974; Georges and Beasley, 1977; Sutherland and Bass, 2004; Jensen et al., 2011]. These acoustic signals may be used to constrain eruption location, duration, and source mechanisms of eruptions in some cases, with potential application to eruption early warning systems (e.g., Ulivieri et al. [2013], Matoza et al. [2017], Ripepe et al. [2018]).

The goal of this research is to provide a comprehensive case study of the Anak Krakatau eruptive activity leading up to, during, and after the major flank collapse, using remote (> 250 km range) infrasound and hydroacoustic signals. We compare these signals with observed eruption activity and satellite imagery to place the signals in context with the eruption chronology, and investigate whether the signals can be related to physical eruption source mechanisms. A new eruptive phase began in June 2018 and cul-

minated in the catastrophic collapse of the volcanic flank and generation of a destructive tsunami on December 22, 2018 [Global Volcanism Program, 2018a, 2019]. After the flank collapse the volcano continued to erupt from the submerged vent, producing Surtseyan activity, ash plumes, explosions, and lava flows [Global Volcanism Program, 2019].

The June 2018 through January 2019 Anak Krakatau eruptive activity was chosen for this study for two reasons: (1) Anak Krakatau is a partially submerged volcano with the bulk of its edifice underwater, and has previously generated both subaerial and submarine eruptions [Global Volcanism Program, 1972, 2018a], making it a good candidate to inspect for infrasound and hydroacoustic signals; and (2) This eruptive activity included a major flank collapse, a volcanogenic tsunami, and prolonged Surtseyan eruptive activity, which are relatively rare in the geophysical record [Paris et al., 2014; Tepp et al., 2019b]. Additional observations of these processes may improve understanding of the relationships between source mechanisms and seismo-acoustic signal and enable future remote identification of these events (e.g., Green et al. [2013], Matoza et al. [2018], Lyons et al. [2020]).

We analyze hydroacoustic and infrasound data for 8 months from the beginning of the new eruptive phase in June 2018 through January 2019. We conduct PMCC array processing to determine the back-azimuth of arrival and other signal characteristics, and inspect waveforms and spectrograms for evidence of eruptive activity. To determine the similarity of the signals, we perform waveform cross-correlation and clustering analysis to classify event signals into families, and propose possible source mechanisms for major signal families. This case study highlights the role that infrasonic and hydroacoustic technology can play in the remote detection and characterization of eruptive activity at submarine and partially submerged volcanoes.

Background and Motivation

The Smithsonian Institution’s Global Volcanism Program (GVP) identifies 1,422 volcanoes worldwide as ‘potentially active’, meaning that they have confirmed historical eruptions or are thought to have erupted during the Holocene [Global Volcanism Program, 2013]. Of these active volcanoes, 40-50 are erupting at any given time, and most are subaerial. Although submarine volcanoes are thought to account for approximately 85% of Earth’s volcanism and 25% of its explosive volcanism [White et al., 2003], only 119 of the known active volcanoes listed by GVP are submarine volcanoes [Global Volcanism Program, 2013]. This is because eruptions at submarine or partially submerged volcanoes are often difficult to observe, and many of these eruptions likely go undetected due to their remoteness and lack of local monitoring instrumentation.

Infrasound and hydroacoustic signal analysis techniques have the potential to detect eruptions where they might otherwise go unnoticed (e.g., Green et al. [2012], Matoza et al. [2019]). These methods are finding increasing utility for volcanic hazard mitigation, as submarine or partially submerged eruptions pose numerous threats including tephra fall [Moore et al., 1966; Thorarinsson, 1967; Mastin and Witter, 2000], explosions and ballistics [Dietz and Sheehy, 1954; Thorarinsson, 1967; Oshima et al., 1991; Mastin and Witter, 2000; Coombs et al., 2019], pyroclastic flows and base surges [Moore, 1967; Sigurdsson et al., 1991; Trofimovs et al., 2008], lahars [Mastin and Witter, 2000], and

mass wasting [Moore et al., 1966, 1989; Heinrich et al., 2001; Caplan-Auerbach et al., 2001]. Volcanic eruptions can also trigger landslides and flank collapse at the erupting volcano or at nearby islands, generating destructive tsunamis [Masson et al., 2006]. Shallow (<200m depth) high-intensity submarine eruptions can break the ocean surface and produce subaerial ash plumes several kilometers high (e.g., Green et al. [2013]; Manga et al. [2018]; Coombs et al. [2019]), which can be extremely hazardous to aircraft as the ash can melt and re-solidify in aircraft engines and result in catastrophic engine failure [Przedpelski and Casadevall, 1991]. Additionally, pumice rafts formed by submarine eruptions can be hazardous to ships that intake water, clogging seawater valves and stalling engines [Global Volcanism Program, 1986], and explosions from shallow submarine eruptions have been known to destroy ocean-going vessels [Dietz and Sheehy, 1954]. During the July 2012 eruption of Havre volcano in the Kermadec Arc, Havre emitted 1.2 km^3 of rhyolite pumice which formed a pumice raft hundreds of kilometers wide [Jutzeler et al., 2014; Carey et al., 2018]. Thus, it is important to be able to detect and monitor erupting volcanoes globally, including those that are submarine, partially submerged, or located long distances from major human populations.

2.1 Infrasound Propagation

Volcanoes produce sound through a variety of processes, including volcanic explosions, jetting, pyroclastic flows, mass wasting, and passive degassing [Matoza et al., 2019]. Volcanoes tend to emit the most acoustic energy in the infrasound range [Campus and Christie, 2010], which is atmospheric sound of frequencies from ~ 0.01 to 20 Hz, below the lower threshold of human hearing. Other sources of atmospheric infrasound include animals [Payne et al., 1986], air and spacecraft [Balachandran and Donn, 1971; Donn, 1978], chemical and nuclear explosions [Grover, 1968; Mutschlecner et al., 1999], microbaroms

[Garcés et al., 2004], ocean surf [Garcés et al., 2003], and many other sources [Campus and Christie, 2010]. The propagation of infrasound waves through the atmosphere depends on the temperature profile, wind speeds, and composition of the atmosphere. Incorporating temperature and wind into the equation for the speed of sound in an ideal gas results in an equation for effective sound speed in the atmosphere [Evers and Haak, 2010]:

$$c_{\text{eff}} = \sqrt{\gamma_g RT} + \hat{n} \cdot \mathbf{u} \quad (2.1)$$

where γ_g is the ratio of specific heats, R is the gas constant for air, T is the absolute temperature, and $\hat{n} \cdot \mathbf{u}$ uses an inner-product to project the wind velocities \mathbf{u} in the direction of the wavefront normal \hat{n} .

Infrasound can travel thousands of kilometers in atmospheric ducts between Earth’s surface and upper atmosphere, making it possible to detect these signals at long source-receiver distances [Liszka, 1974; Georges and Beasley, 1977; Sutherland and Bass, 2004; Campus and Christie, 2010]. The atmosphere is divided into several layers, which are characterized by changes in temperature (Figure 2.1). While local infrasound propagates from source to receiver through the lower troposphere only, regional and global infrasound will likely have propagated through the stratosphere, mesosphere, or thermosphere before it is refracted back to the ground [Drob et al., 2010]. The majority of regional and global infrasound ($\sim 80\%$) propagates through the stratosphere, as the thermosphere has higher signal attenuation due to low atmospheric particle density and loss of acoustic energy to the upper atmosphere [Sutherland and Bass, 2004; Le Pichon et al., 2009].

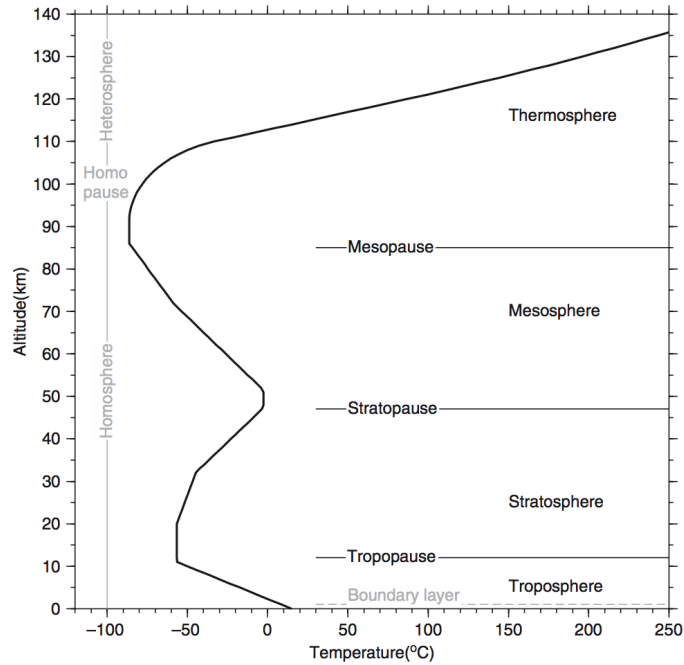


Figure 2.1: Figure reproduced from Evers and Haak [2010] showing atmospheric temperature profile with altitude, from the U.S. Standard Atmosphere [NOAA et al., 1976].

Long range propagation of infrasound occurs because low frequencies experience lower attenuation in the atmosphere compared with higher frequencies [Sutherland and Bass, 2004], and also because a combination of vertical temperature gradients and strong horizontal winds (Equation 2.1) result in the creation of atmospheric low-sound-velocity waveguides which efficiently duct infrasound to long distances. Drob et al. [2010] identifies two major infrasonic ducts, one in the stratosphere at $\sim 35\text{-}55$ km in which most long-range infrasound propagates, and one in the lower thermosphere at $\sim 90\text{-}120$ km which experiences much higher attenuation (Figure 2.2). Though infrasound ducted at long range through the stratosphere experiences multi-pathing and scattering due to variations in atmospheric temperature and wind velocity, acoustic source characteristics can sometimes still be determined (e.g., Fee et al. [2010], Dabrowa et al. [2011], Matoza et al. [2011a], and Fee et al. [2013]) and eruptions may be located by tracing the direc-

tion of signal arrival at multiple stations (e.g., Matoza et al. [2017] and Matoza et al. [2018]). Since erupting volcanoes tend to be powerful, stationary sources of infrasound, infrasound technology has emerged in recent years as a useful tool to detect and locate volcanic eruptions at local to remote distances.

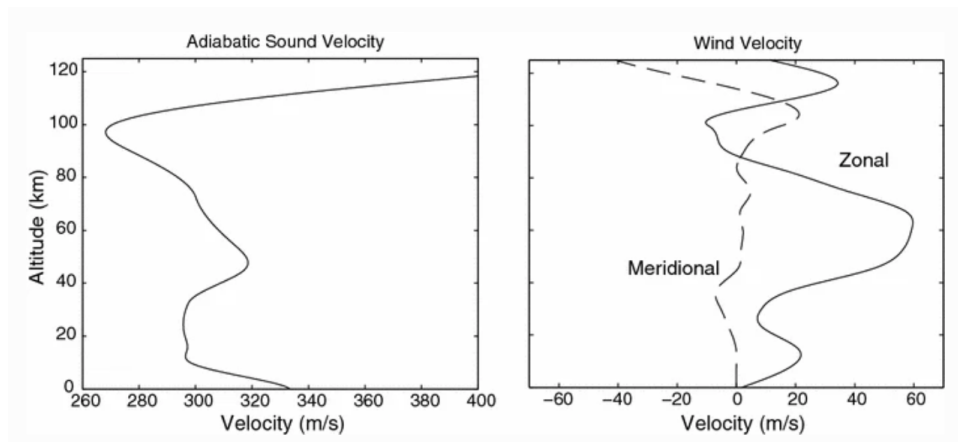


Figure 2.2: Figure reproduced from Drob et al. [2010] showing climatological profiles. The left panel shows adiabatic sound velocity, and the right panel shows zonal and meridional wind velocity from empirical models (developed by Hedin et al. [1996] and Picone et al. [2002]) for January 1, 2005 at 00:00 UTC.

2.2 Hydroacoustic Propagation

Hydroacoustics is the study of sound and its behavior in water. Submarine sound is produced by many natural sources, such as animals (schools of fish [Rose and Leggett, 1988], whales [D’Vincent et al., 1985], etc.), storms [Davy et al., 2014], earthquakes [Guilbert et al., 2005], and volcanic eruptions (e.g., Chadwick et al. [2008], Green et al. [2013], Metz et al. [2016]). Anthropogenic ocean sound is generated by human activities, and includes noise from shipping and recreational traffic [Urick, 1984], coastal construction [Denes et al., 2016], fossil fuel or mineral exploration and extraction [Hildebrand, 2009], and naval activities [Parsons, 2017]. Anthropogenic ocean noise appears to be increasing over time as populations grow [Committee on Potential Impacts of Ambient Noise in

the Ocean on Marine Mammals, 2003; McDonald et al., 2006], which is of growing environmental concern due to its negative ecological effects on acoustically sensitive marine animal species which rely on hearing for vital functions such as avoidance of predators and sensory perception (e.g., Simpson et al. [2016], McCauley et al. [2017]).

Underwater sound is energy that is transmitted by water molecules passing energy to adjacent molecules, and therefore travels faster and more efficiently through denser media. Thus, the speed of sound in seawater is much higher (approximately 1500 m/s) than the speed of sound through air (~ 343 m/s at the ground surface at 20°C air temperature). The speed of sound in the ocean is dependent on several variables, including water temperature, salinity, and pressure, an increase in any of which will also increase the speed of a sound wave propagating through the water. The speed of sound in seawater (c , in meters per second) is typically calculated using a simplified empirical function of temperature (T , in $^\circ\text{C}$), salinity (S , dissolved weight of salts in parts per thousand), and depth (z , in meters), given by Medwin [1975]:

$$c = 1449.2 + 4.6T - 0.055T^2 + 0.00029T^3 + (1.34 - 0.01T)(S - 35) + 0.016z \quad (2.2)$$

Volcanogenic hydroacoustic waves can propagate with high efficiency and low attenuation in the ocean water column due to the presence of the Sound Fixing and Ranging (SOFAR) channel waveguide, also known as the deep sound channel (DSC) axis (Figure 2.3, Jensen et al. [2011]; Ewing and Worzel [1948]). The crossing of inverse temperature and pressure gradients in the ocean results in an axis (~ 1 km deep at temperate latitudes [Johnson and Norris, 1968]) where sound propagates at its lowest velocity. As determined by Snell's Law, this axis of minimum velocity causes an incident sound wave crossing this axis at an angle other than vertical to be refracted and transmitted at decreasing angles until it bends toward the axis once more, acting as a waveguide and focusing the sound

along the axis direction [Ewing and Worzel, 1948]. The canonical function for calculating an idealized deep water sound speed profile, known as the Munk profile, is given by Munk [1974]:

$$c(z) = 1500.0 [1.0 + \epsilon (\tilde{z} - 1 + e^{-\tilde{z}})] \quad (2.3)$$

where ϵ is a perturbation coefficient equaling 0.00737, and \tilde{z} is the scaled depth given by $\tilde{z} = \frac{2(z-1300)}{1300}$. The Munk Profile is useful for describing the general features of deep sound channel propagation at temperate latitudes.

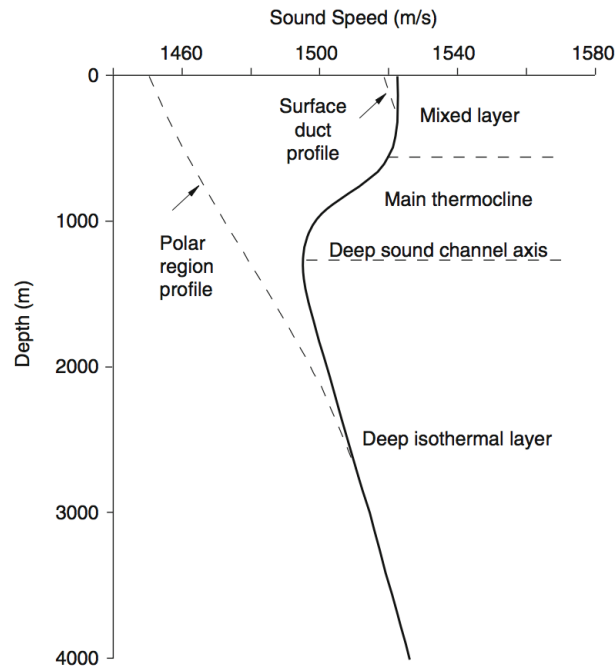


Figure 2.3: Figure reproduced from Jensen et al. [2011] showing generic sound speed profiles for polar regions (left-hand dashed line), low-altitude regions (solid line), and surface ducts (right-hand dashed line), showing the depth of the SOFAR channel axis at the minimum sound speed location.

The SOFAR waveguide allows signals to propagate exclusively by refraction, so minimal sound signal power is lost through reflection of the wave against the sea surface or seafloor (Figure 2.4, Jensen et al. [2011]). This low rate of attenuation allows waves

trapped within the SOFAR waveguide to be transmitted great distances, with the longest recorded range of a submarine volcanic signal propagating through the SOFAR channel to a source-receiver distance of 15,835 km, from a volcano in the South Pacific Ocean to an IMS hydroacoustic station in the South Atlantic Ocean (Figure 2.5, Metz et al. [2016]). These global-distance detections highlight the potential of the IMS hydroacoustic stations to be used in remotely detecting submarine volcanic activity on a global scale, although this global detectability can also be a limitation since noise also propagates efficiently and must be separated from signals of interest.

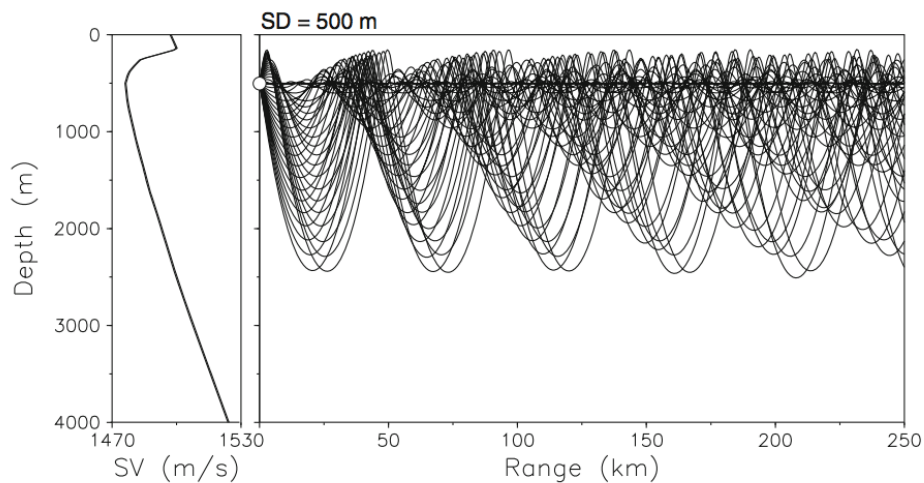


Figure 2.4: Figure reproduced from Jensen et al. [2011] showing SOFAR channel propagation without interaction with sea surface or seafloor boundaries in the Norwegian Sea for a source at 500 m, the axis of the SOFAR channel at this latitude.

Hydroacoustic signals were first detected from a submarine volcanic eruption in 1952 by the U.S. Navy, when trans-Pacific explosion signals from Myojin volcano near Japan were detected on Navy hydrophones located off California [Dietz and Sheehy, 1954]. That same year, hydrophones deployed by the U.S. Navy and researchers recorded hydroacoustic signals produced during the birth of Bàrcena volcano, located at the southern end of San Benedicto Island, 350 km south of the southern end of Baja California [Snodgrass

and Richards, 1956]. Erupting volcanoes are a common source of submarine hydroacoustic signals, and may be identified by their stationary location and capacity for continuous signal emission, whereas many other sources are transitory in time and location. Despite immense hydrostatic pressure which increases by 100 kPa for every 10 m of depth, both basaltic and silicic volcanoes can produce explosive submarine eruptions at depths up to 1-2 kilometers [Helo et al., 2011; White et al., 2015; Dziak et al., 2015].

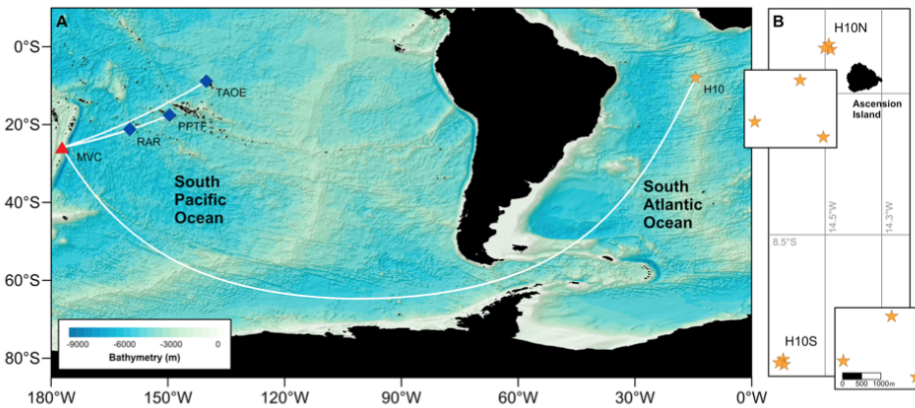


Figure 2.5: Figure reproduced from Metz et al. [2016]. Panel (A) shows a bathymetry map of Monowai volcano (red triangle), with explosive volcanic eruption signals recorded at three broadband seismic stations (blue diamonds) located nearby in the South Pacific Ocean and IMS hydroacoustic station at a distance of 15,717 to 15,834 km from the volcano in the South Atlantic Ocean. Panel (B) shows the hydrophone station configuration of IMS station H10, where H10N is the northern triplet and H10S is the southern triplet in the array.

Explosive volcanic processes such as explosions caused by magma-seawater interactions, jetting of material, or pyroclastic activity may generate powerful hydroacoustic signals which propagate outward from the volcanic source [Chadwick et al., 2008; Green et al., 2013; Dziak et al., 2015; Metz et al., 2016]. In addition to explosive activity, hydroacoustic waves may be excited by reverberations of gas in magma pathways, dome collapse, and mass wasting events such as flank collapses or underwater landslides [Caplan-Auerbach and Duennebier, 2001; Dziak and Fox, 2002a; Chadwick et al., 2008; Dziak et al., 2015; White et al., 2015]. As an example of IMS capability to detect hydroacoustic signal

from erupting submarine volcanoes, Figure 2.6 gives examples of hydroacoustic events from South Sarigan seamount in the Marianas Arc captured by IMS hydrophone H11N in the Pacific Ocean at a distance of 2,260 km. This demonstrates IMS hydrophone network may be a useful tool in detecting volcanic signals at long range and offering interpretations of how physical eruption processes at the submarine volcano relate to hydroacoustic signal characteristics.

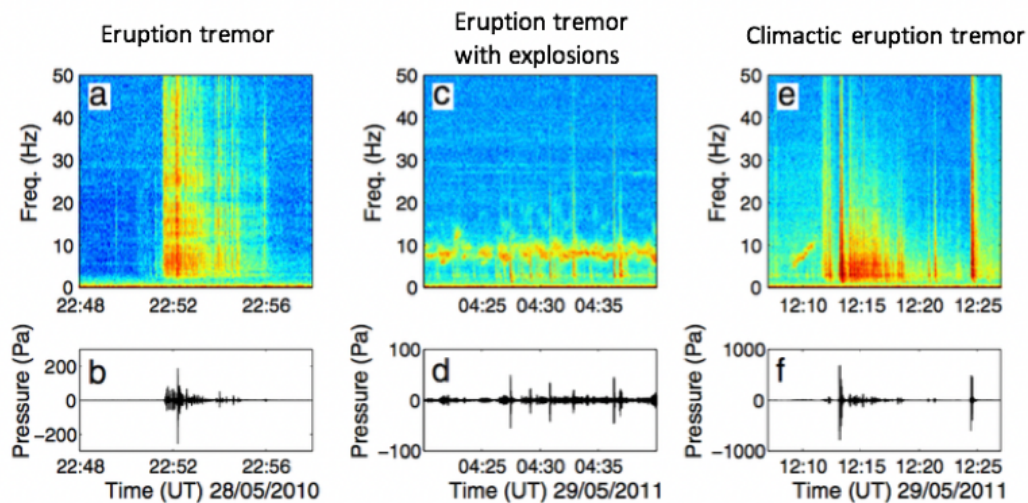


Figure 2.6: Example of hydroacoustic waveforms and spectrograms from the 2010 eruption of South Sarigan volcano, recorded at IMS hydrophone station H11N (located 2,260 km from South Sarigan). Eruption tremor is present on May 28, followed by sustained 10 Hz tremor and explosions (distinct spectral pulses) on May 29. The last spectrogram and waveform show the 12 minute climactic eruption signal which generated 30% of the overall hydroacoustic signal power, attributed to two large magmatically driven explosions. Figure reproduced from Green et al. [2013].

Another type of hydroacoustic monitoring is possible using seismic stations based on land. When volcanic activity produces hydroacoustic waves that propagate through the water column and reach the sides of steeply sloping islands or continents, the hydroacoustic energy can couple into the solid rock, producing tertiary seismic waves known as *T-phases* [Tolstoy and Ewing, 1950]. Previously unknown submarine volcanoes have been discovered using T-phases, such as the discovery of Macdonald seamount by Norris and

Johnson [1969] and the detection of volcanoes related to the Society hotspot in French Polynesia [Talandier and Kuster, 1976; Talandier and Okal, 1984, 1987]. T-phases have also been used to investigate signals from strong submarine earthquakes, for example as described in de Groot-Hedlin [2020] where seismometers captured T-phase signals from two earthquakes at distances up to 1,134 km inland from the coastline. This study does not use T-phase seismic stations, but rather relies on moored hydrophone stations to detect hydroacoustic signal.

Due to the challenges of observing volcanoes in a submarine environment, the study of submarine explosive volcanism is still in its infancy. Only two active deep-ocean submarine eruptions have been visually observed: the eruption of NW Rota-1 volcano in the Mariana Arc in 2006 [Chadwick et al., 2008], and the eruption of West Mata volcano near Samoa in 2009 [Resing et al., 2011]. Thus, there are many questions still unanswered about the source mechanisms of submarine explosive eruptions, how these eruptions produce acoustic energy, and how they differ from subaerial eruptions.

2.3 The International Monitoring System Network

The newly constructed International Monitoring System (IMS) infrasound and hydroacoustic networks are valuable sources of global infrasonic and hydroacoustic data. The Comprehensive Nuclear Test Ban Treaty (CTBT) of 1996 proposed a ban on nuclear detonations in all environments, with the mandate that a global system of monitoring stations would be installed as part of the compliance and verification regime, and would consist of seismic, infrasound, hydroacoustic, and radionuclide stations. The station locations were chosen for optimal global coverage to detect nuclear explosions as small as 1 kiloton anywhere on Earth [Christie and Campus, 2010]. At the time of writing, the IMS infrasound network currently consists of 50 infrasound stations that have been

constructed and certified out of a planned 60 stations. Each IMS infrasound station consists of four or more infrasonic sensors forming an array with 1-3 km aperture (Figure 2.7). The sensors are high-sensitivity microbarometers which record fluctuations in micro-pressure caused by infrasound waves propagating in the atmosphere at a sampling rate of 20 Hz and flat sensor response in the passband of 0.02 to 4 Hz [Christie and Campus, 2010]. The IMS monitoring stations transmit data via satellite antennas to the International Data Center (IDC) of the Comprehensive Nuclear Test Ban Treaty Organization (CTBTO) in Vienna, Austria, where it can be used to locate and characterize events.

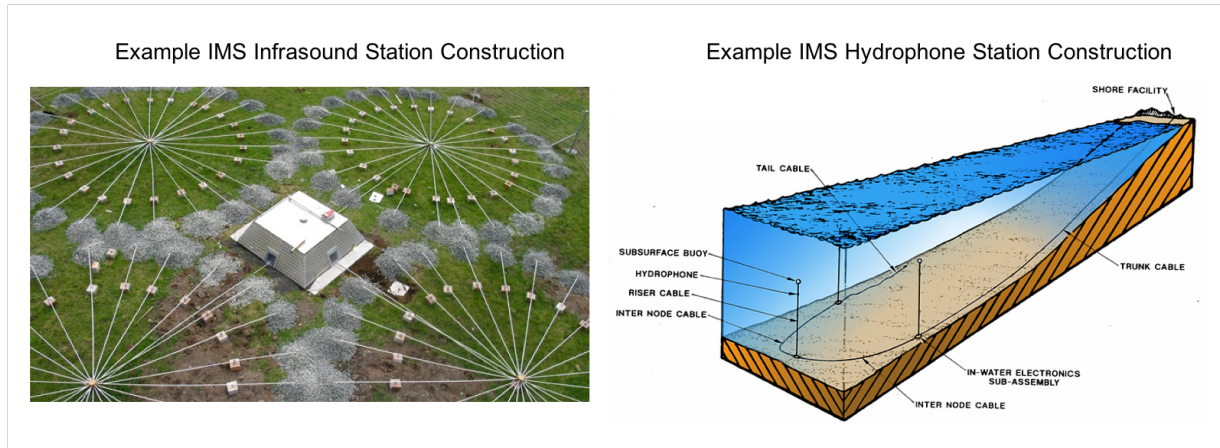


Figure 2.7: Left: Arrays of IMS infrasound station IS49. Each array element uses spatial pipe structures which connect inlet ports to a manifold to reduce wind noise. Right: an IMS hydroacoustic station's underwater construction. Image credit: CTBTO.

The IMS hydroacoustic network contains eleven hydroacoustic arrays composed of one to two sensor triplets, spaced throughout Earth's oceans. Six of the hydroacoustic stations, including H01 and H08 used in this study, are moored hydrophones that are positioned at the depth of the SOFAR channel axis (approximately 0.5 km to 1.5 km deep, dependent on latitude) to intercept long-distance hydroacoustic signals. The other five

stations consist of seismic sensors positioned on small islands with steeply sloping flanks to detect T-phases [Lawrence, 2004]. The hydroacoustic stations used in this study are all moored hydrophone stations, which consist of 1 to 2 sensor triplets recording continuous data at a sampling rate of 250 Hz (Figure 2.7). The hydrophones are suspended by subsurface floats and anchored to the ocean floor. Seabed anchored fiber-optic cables connect the sensors to shore facilities 50-100 km away which then transmit signals to the IDC.

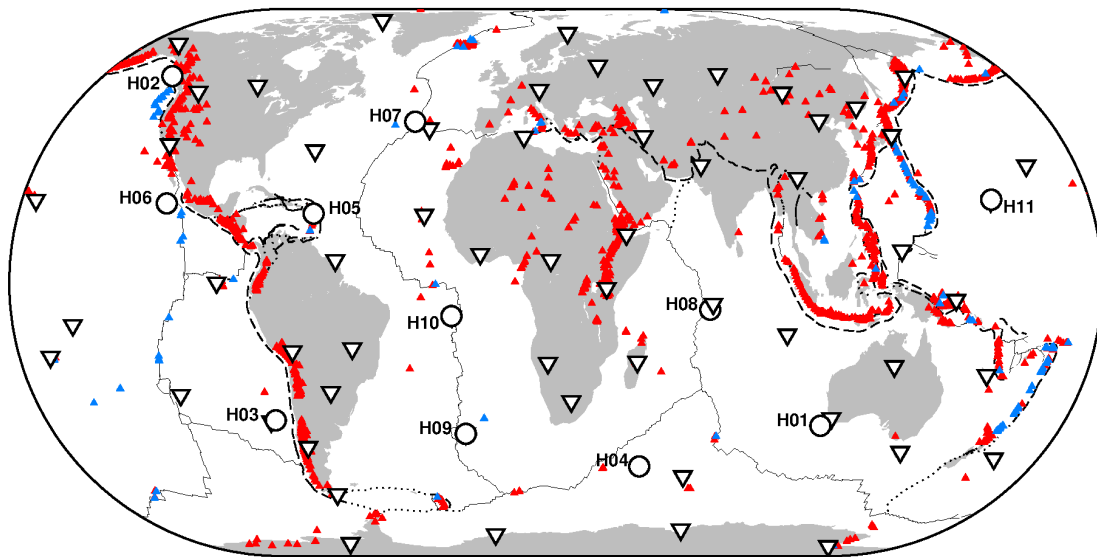


Figure 2.8: Station locations of the International Monitoring System global infrasound network (white inverted triangles) and global hydroacoustic network (white circles). Hydroacoustic stations are labeled with their station names. Locations of global potentially active volcanoes are represented by colored triangles, with subaerial or partially submerged volcanoes represented with red triangles and fully submarine volcanoes represented by blue triangles (though it is likely that many other active submarine volcanoes exist but have not yet been identified) [Global Volcanism Program, 2013].

The station locations of the IMS network infrasound and hydroacoustic networks are shown on Figure 2.8 along with the locations of volcanoes identified by the GVP as being potentially active in the Holocene [Global Volcanism Program, 2013]. Because the true extent of seafloor volcanism is unknown, there may be thousands to millions

of undiscovered seafloor volcanoes which are not shown. Volcanic infrasound is now regularly detected, and hydroacoustic signal occasionally detected, at IMS stations and used to determine eruption characteristics (e.g., Fee et al. [2010]; Matoza et al. [2011a,b]; Green et al. [2013]; Metz et al. [2016]; Matoza et al. [2018]). Recently, new methods have been developed to systematically search multi-year IMS infrasound data to detect global volcanic signals, as a step toward creating a global early warning system for volcanic eruptions and better catalog Earth’s explosive volcanism [Matoza et al., 2017].

2.4 Anak Krakatau Geologic Setting and Eruption History

Anak Krakatau (“child of Krakatau” in Indonesian) is a highly active volcano located on the rim of the caldera formed by the 1883 paroxysmal eruption of Krakatau in the Sunda Strait, Indonesia. The Krakatau volcanic complex is the result of arc volcanism caused by subduction of the Australian plate beneath the Sunda plate, directly below Krakatau, and crustal thinning caused by the extensional faulting and rifting of the Sunda Strait (Figure 2.9, Dahren et al. [2011]). The 1883 eruption culminated in a sequence of large magmatically driven explosions that generated catastrophic pyroclastic flows and a tsunami in the Sunda Strait [Self and Rampino, 1981], which together are thought to have killed over 36,000 people [Auker et al., 2013]. The 1883 tsunami generation mechanism is debated; pyroclastic flows entering the ocean [Self and Rampino, 1981] or violent submarine explosions [Yokoyama, 1981] have been proposed as the source of the tsunami. The eruption destroyed most of the volcanic edifice, forming a partially-submarine caldera. Anak Krakatau began forming on the northeast rim of the caldera during an eruption in 1927, and first emerged above sea level in 1928 [Stehn, 1929].

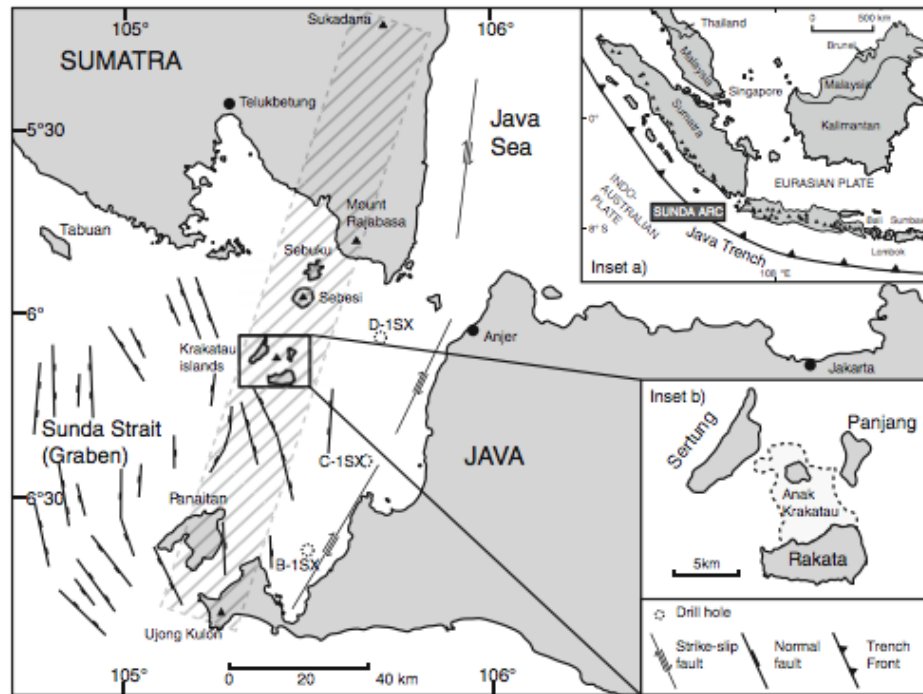


Figure 2.9: Structural map of the Sunda Strait region, showing location of Krakatau complex in the Sunda Strait between Java and Sumatra, and the location of Anak Krakatau. The hatched rectangle represents a north-south trending chain of quaternary volcanic centers. The extensive faulting and rifting of the Sunda Strait graben is a consequence of the clockwise rotation of the island of Sumatra relative to the island of Java since the late Cenozoic by approximately 20° . Figure reproduced from Dahren et al. [2011].

The volcano continued erupting frequently, with at least 40 recorded episodes of Strombolian to Vulcanian style eruptive activity characterized by heightened seismic activity, explosions, ash plumes, incandescent ejecta, lava flows, and fire fountaining [Global Volcanism Program, 2019]. A submarine eruption on the volcano's south flank was observed by eyewitnesses on April 11, 1972 [Global Volcanism Program, 1972], and lava domes were reported in 2011, 2012, and 2017 [Global Volcanism Program, 2011, 2012, 2017]. By October 2018 the cone had grown to 338 m above sea level [Global Volcanism Program, 2018a]. Anak Krakatau was mainly active on its southwest side toward the center of the 1883 caldera, making the southwest volcanic flanks unstable. Numerical simulations published in 2012 indicated that a hypothetical flank collapse toward the southwest

could generate a tsunami that would reach the islands surrounding Anak Krakatau within 1 minute and the coastal cities of Sumatra and Java within 35-45 minutes of the collapse [Giachetti et al., 2012].

2.5 Anak Krakatau 2018-2019 Eruptive Activity

After 15 months of quietude, a new eruptive phase began on June 18, 2018, indicated by an increase in seismic activity [Global Volcanism Program, 2018a]. Ash plumes from the volcano were first visible on June 21, 2018, followed by the first incandescence observed on July 1, 2018. Lava flows reached the sea on September 22, 2018, and frequent explosions, ash plumes, and incandescent material were observed through December of 2018 [Global Volcanism Program, 2019]. On December 22, 2018, there was a significant increase in eruptive activity, with 423 explosions observed in one six-hour period from 12:00 to 18:00 local time by the PVMBG [PVMBG via Detik News, 2018]. At 21:03 local time, the southwest side and summit of the volcano collapsed into the ocean as a result of the eruption, resulting in a tsunami first detected at 21:27 local time. The tsunami hit the coastlines of Banten and Lampung, traveling up to 330 m inland with a maximum surveyed runup of 13.5 m [Muhari et al., 2019]. Estimates by Ye et al. [2020] indicate that the flank collapse slide volume was small ($\sim 0.2 \text{ km}^3$), and did not produce short-period seismic waves strong enough to trigger a tsunami warning from the existing Indonesian tsunami warning system which was designed to detect tsunamis from earthquake sources [Strunz et al., 2011]. Indonesian authorities reported 437 deaths, and tens of thousands of injuries as a result of the tsunami [Global Volcanism Program, 2019]. As a result of the December 22 partial collapse, the vent was submerged under tens of meters of seawater. Surtseyan activity and base surges were observed from December 23, 2018 through January 9, 2019 when a rim of tephra formed around the vent. The

rim created a barrier between the vent and the ocean, forming a crater lake above the vent (Figure 2.10). The flank collapse reduced the height of the volcano from 338 to 110 m. Since the tsunamigenic event, eruption activity has continued at a smaller scale at Anak Krakatau. Intermittent ash plumes, explosions, and seismic events recorded on Anak Krakatau's seismic network were reported throughout 2019 to April 2020, and in mid-April 2020 Strombolian activity accompanied a lava flow from the crater which filled the crater lake, covering the vent [Global Volcanism Program, 2020]. The eruption is continuing at the time of writing.

Several geophysical studies and reconstructions of the 2018 flank collapse and tsunami have now been made. Williams et al. [2019] analyzed high-resolution satellite imagery and eyewitness accounts to estimate the volume of the flank collapse, and suggested that the collapse consisted of multiple failures (though only the first generated a tsunami). Walter et al. [2019] identified a high-frequency seismic event (a possible explosion or volcanic earthquake) that occurred only ~ 115 s before the flank collapse, which they suggest was involved in the failure or possibly even triggered it.

The study also used a variety of other methods including satellite imagery analysis, drone photogrammetry, tsunami modeling, SO_2 monitoring, and infrasound to suggest that increased flank motion, thermal emissions, and short seismic events were precursors of the climactic eruption, and that the assessment of these at volcanoes could aid future warning systems. Perttu et al. [2020] used seismic, acoustic, satellite, and eyewitness observations to compile a timeline of the climactic eruption sequence, indicating that the flank collapsed in one event which was observed on regional infrasound stations but not on regional hydroacoustic stations. Ye et al. [2020] investigated the seismic signals generated by the flank collapse, calculating the force amplitude and estimating the sliding volume ($< \sim 0.2 \text{ km}^3$) to be closely comparable with the $\sim 0.1 \text{ km}^3$ suggested by Williams et al. [2019].

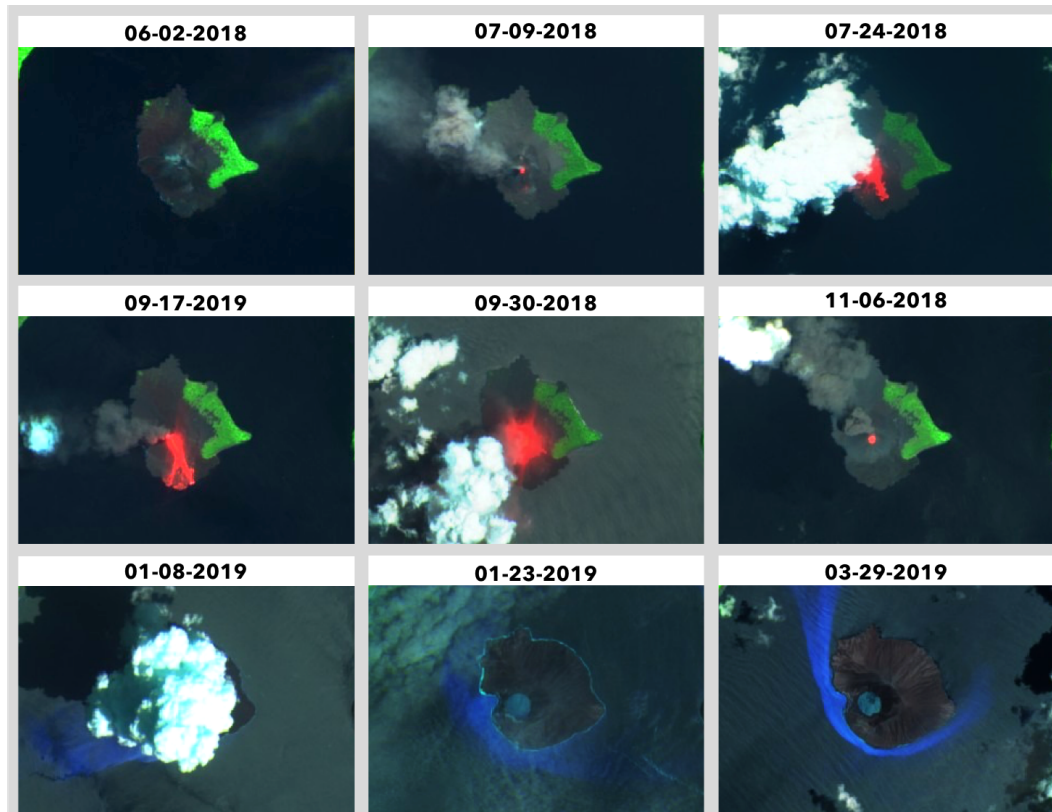


Figure 2.10: Sentinel-2 thermal satellite images of Anak Krakatau from just before the start of the new eruptive phase in June 2018 to three months after the flank collapse in March 2019. The intact volcanic flank and cone are shown in the June 2, 2018 image. Ash plumes and lava flows are then visible until November 2018, but clouds and ash obscured satellite imagery until after the flank collapse and tsunami on December 22, 2018. The first clear image of Anak Krakatau after the flank collapse is on January 1, 2019 which shows a large steam plume from Surtseyan eruption activity, followed by two images of the new edifice morphology and crater lake in January and March 2019. This short wave infrared spectral range (SWIR) satellite imagery is compiled from bands 12, 8A, and 4 of the Sentinel-2 satellite and was obtained using Sentinel Hub Playground [Modified Copernicus Sentinel Data, 2019].

Here, we present context for the broader scale of the eruption by extending the analysis of infrasound and hydroacoustic signals beyond the major flank collapse and Surtseyan activity, to include all activity since the start of the new eruptive phase in June 2018. In addition, we present new waveform similarity analyses to complement existing research on volcanic processes which may have generated infrasound and hydroacoustic signals from the climactic eruption event.

Array Processing and Spectrogram Analysis

3.1 The PMCC Method

We conduct array processing using the Progressive Multi-Channel Correlation (PMCC) algorithm [Cansi, 1995] to detect hydroacoustic and infrasound signals at each IMS station and determine the back-azimuth. PMCC is a time-domain cross-correlation method that calculates signal arrival time delays (δt) between the sensor pairs at a specified array and measures the *consistency* of the signal between the sensor triplets using the relation:

$$r_{ijk} = \Delta t_{ij} + \Delta t_{jk} + \Delta t_{ki} \quad (3.1)$$

If a signal has a consistency r that is below a specified value between i,j,k sensors, the PMCC algorithm regards it as a coherent detection and temporarily records the wave characteristics. The algorithm repeats this calculation for a number of additional time windows and frequency bands until a full list of detections with corresponding arrival times, arrival azimuths, frequencies, velocities, amplitudes, and other characteristics is generated (Figure 3.1). PMCC progressively adds additional subsets of array stations

to the calculation. If the addition of progressive subsets results in strong variation of the azimuth, velocity, or time for a detection, PMCC rejects the detection, but if all subset combinations are consistent the detection is logged as a ‘pixel’ [Cansi, 1995; Cansi and Klinger, 1997; Le Pichon and Cansi, 2003]. The final outputs of the PMCC are a ‘families’ file listing each family of detections and pixels contributing to each family, and a ‘bulletin’ file listing a short description of each family [Alyotech, 2014].

The PMCC method is the signal detector in use by the IDC and has frequently been used for processing of infrasound data, but has not commonly been applied to hydroacoustic data. Therefore in preliminary work for this study we tested the method using published eruption case studies to calibrate the parameters specifically to hydroacoustic data (e.g., choosing appropriate wave velocity, frequency, number of bands, etc.), making this one of the only demonstrations of the PMCC method for hydroacoustic data of which we are aware.

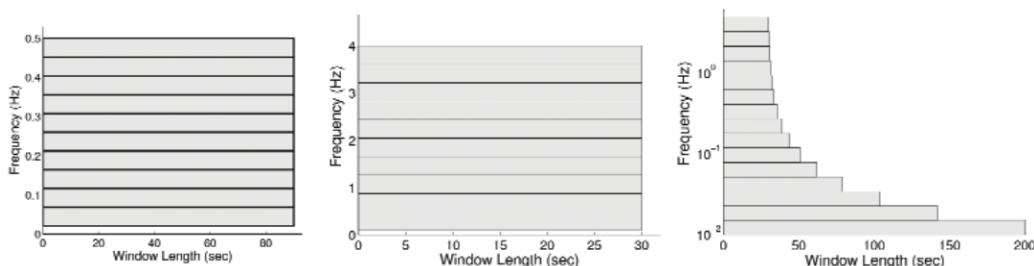


Figure 3.1: Figure reproduced from Le Pichon et al. [2010], with panels a) and b) showing two different window length and frequency band configurations, and panel c) showing how PMCC combines them into a single configuration using a log-spaced filter and variable window length.

3.2 Infrasound Data and Chronology

The three closest IMS infrasound stations to Anak Krakatau are stations IS06, IS07, and IS52, at respective distances of 1,156 km, 3,475 km, 3,638 km from the volcano (Figure 3.2). IS06 is located in the Cocos islands, IS07 is located in Warramunga, Northwest

Territories, Australia, and IS52 is located in the British Indian Ocean Territory, Chagos Archipelago. Stations IS06 and IS07 are operated by Australia, and station IS52 is operated by the United Kingdom. We analyze infrasound data from these three stations from the start of the eruptive phase in June 2018 through January 2019 in this study.

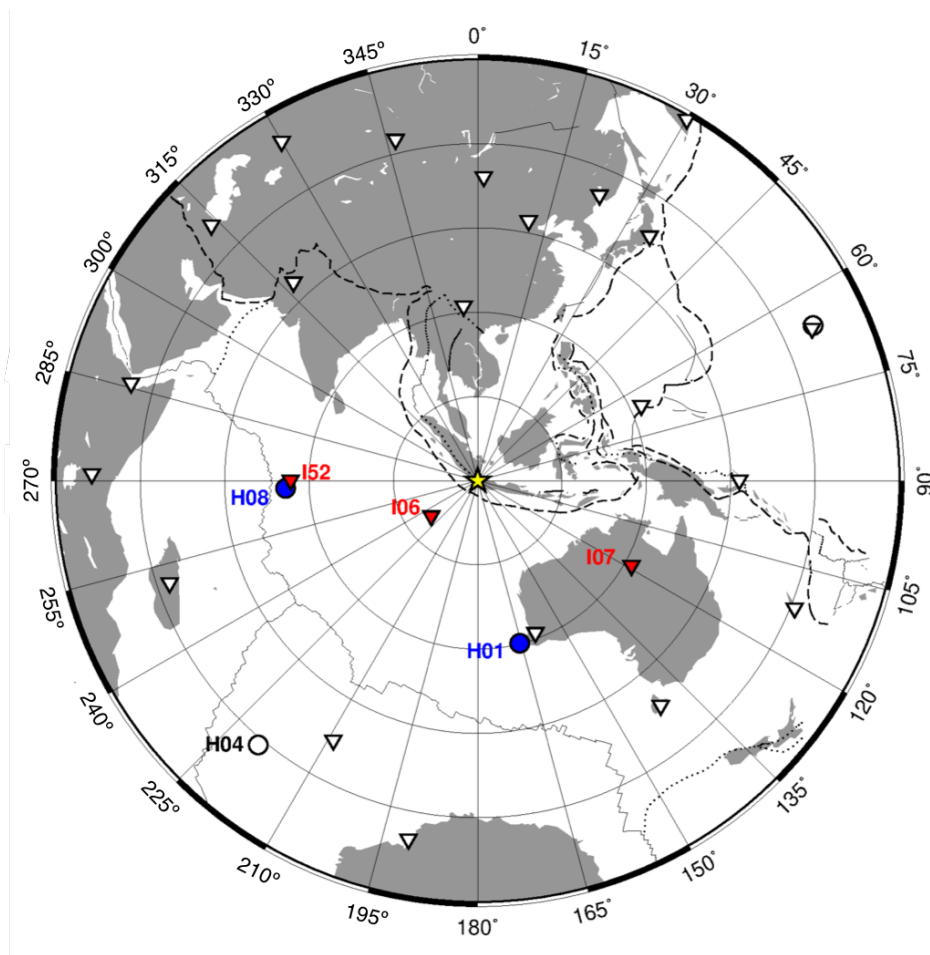


Figure 3.2: Azimuthal equidistant projection map showing the location of Anak Krakatau volcano (yellow star) in relation to the three IMS infrasound stations used in this study (red inverted triangles; IS06, IS07, and IS52) and the two IMS hydroacoustic stations used in this study (blue circles; H01W and H08S). The gridlines are spaced at 15° for both longitude and latitude.

To create spectrograms we band-pass filter the infrasound data from 0.7-4 Hz to reduce microbarom and surf noise, and beamform the data using a time-delay beamformer developed by Matoza et al. [2007]. The beamformer calculates the time delays between

sensors, applies a time-shift, stacks the traces together, and divides by the number of sensors. This allows the station to detect a signal arriving from a particular direction and at a specified velocity and thus reduces noise by boosting the azimuthally and move-out corrected coherent signal.

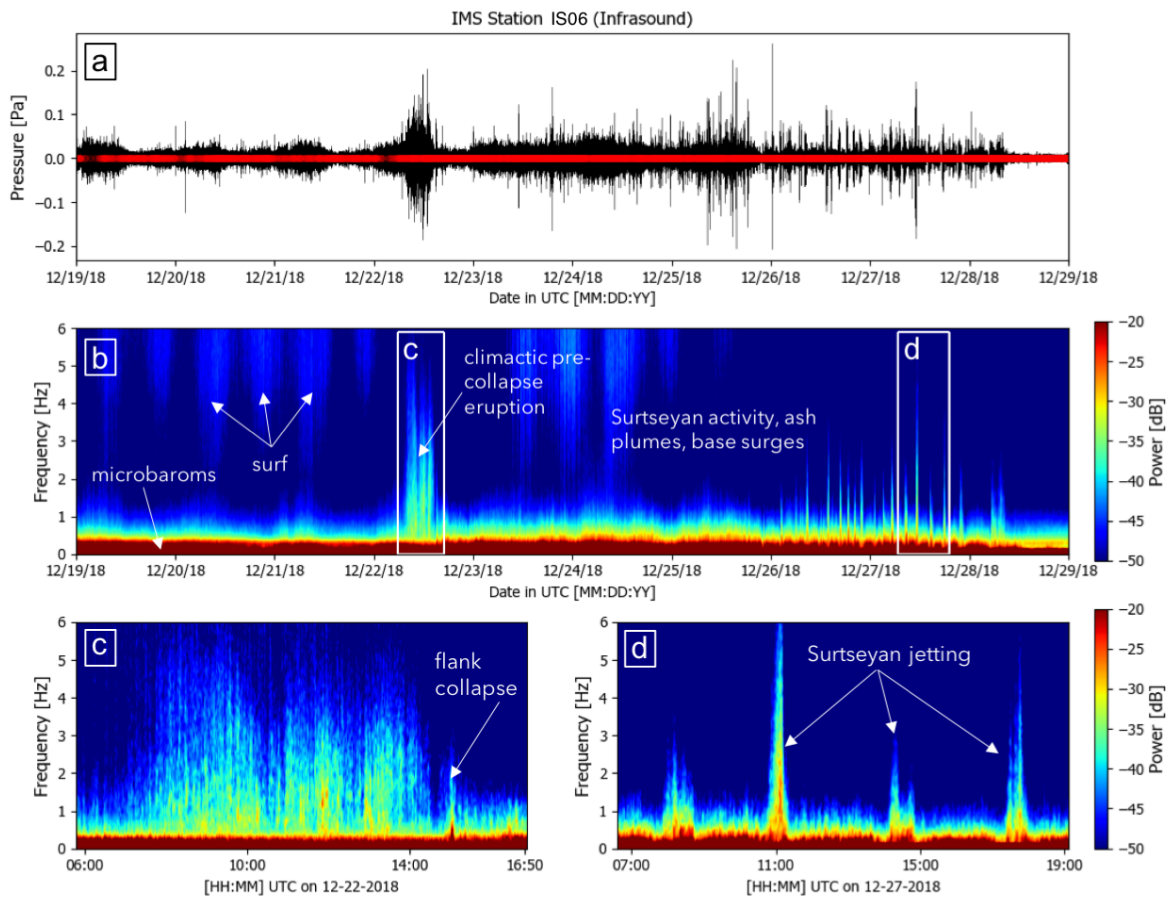


Figure 3.3: Infrasound station IS06 waveforms and spectrograms for a 10-day period, showing the beginning of the climactic eruption phase and flank collapse on December 22, 2018, and 6 days of signals interpreted as Surtseyan activity, base surges, and ash plumes based on eyewitness observations of the volcano reported by the GVP [Global Volcanism Program, 2019]. Panel a) shows the signal which has been beamformed to increase the signal-to-noise ratio and bandpass filtered from 0.7-4 Hz to exclude microbarom and surf noise, with red circles indicating times when coherent signal was detected by PMCC as arriving at IS06 from the back-azimuth of Anak Krakatau (55.5°). Panel b) shows the raw spectrogram from sensor I06H1 for the 10-day timespan. Panels c) and d) show spectra details for the time of the high energy pre-collapse eruption and flank collapse, and the Surtseyan jetting signals, respectively.

The climactic eruption phase beginning on December 22, 2018 is clearly visible in the waveforms, spectrograms, and PMCC detections at IS06 (Figure 3.3). A high-amplitude signal with broadband frequency content is present on December 22, 2018, lasting ~ 7.5 hours, followed by a lower amplitude, low-frequency signal representing the flank collapse. Broadband pulses through December 28, 2018, likely due to Surtseyan activity caused by the vent being submerged by seawater. Base surges and ash plumes were also reported during this time [Global Volcanism Program, 2019]. Broadband noise is present on the spectrogram on (Figure 3.3), likely caused by local surf activity due to station I06H's location on the Cocos Islands. The low frequency signal in the 0.1-0.5 Hz band is due to microbaroms, which are infrasonic waves generated by nonlinear interaction of ocean waves with the atmosphere at the sea surface [Waxler and Gilbert, 2006; Garces et al., 2010].

We present PMCC bulletin (i.e., summary) detections for the closest infrasound station, IS06, on Figure 3.4. Intermittent eruptive activity is visible in the PMCC detections for station IS06 throughout the new eruptive phase, from late June 2018 until the December 22, 2018 flank collapse event. This activity prior to the flank collapse consists of small explosive events occurring consistently at the Anak Krakatau back-azimuth between quiet periods of days or weeks, which generally align with visual and seismic observations recorded in the GVP bulletin for Anak Krakatau [Global Volcanism Program, 2018a]. Figure 3.5 presents detail of these infrasound detections, showing the detections from June 1, 2018 through January 31, 2019, as well as magnified bulletin detections, waveforms, and spectrograms for two of the more powerful sequences of prior eruptive activity (sequence **a** and sequence **b**). Sequence **a** consists of three sustained bursts of activity across 6 days (from August 4-9, 2018), during which time eyewitnesses at Anak Krakatau reported dense ash plumes, Strombolian activity, incandescent ejecta, and a lava flow entering the ocean, and the Anak Krakatau seismic network recorded contin-

uous tremor [Global Volcanism Program, 2018a]. Sequence **b** consists of two sustained bursts of activity over 2 days (from October 8-9, 2018). Sentinel-2 thermal satellite images show incandescence in the crater and emission of ash throughout the month of October, 2018, including October 7 and October 10, 2018 [Modified Copernicus Sentinel Data, 2019]. At least 6 other sequences of eruption detections are visible in the months prior to the flank collapse, which are similar in frequency content and duration to the two magnified sequences, and were all of generally higher frequency than the post-flank collapse eruption. These sequence **b** detections highlight the utility of remote infrasound data, especially where visual observations are unavailable.

The climactic eruption and flank collapse sequence is visible on the IS06 infrasound PMCC bulletin detections as a consistent, high number of detections starting December 22, 2018, and continuing through January 5, 2019. These detections represent explosions, Surtseyan activity, base surges, and ash plumes that were reported by the GVP during the climactic eruption phase. During this time interval, PMCC identified a high density of detections arriving from the back-azimuth of Anak Krakatau, as shown in the histogram of detections in Figure 3.4. Signal that is identified as coherent by PMCC but is not associated with suspected volcanic activity (i.e. not the signals of interest) is considered “clutter” [Matoza et al., 2013]. At station IS06, bands of clutter are visible from approximately 170° - 350° back-azimuth. We interpret the low frequency clutter with wide azimuthal range as microbaroms, and clutter with stationary back-azimuth and higher frequency as anthropogenic noise.

PMCC bulletin detections for infrasound station IS07 are plotted on Figure 3.6. The climactic eruption is not visible in the PMCC detections at this station. Since infrasound propagation is strengthened when atmospheric winds are directed along the same direction as the wave propagation (especially stratospheric winds for long-range infrasound), and inhibited by wind in the opposite direction [Mutschlecner and Whitaker,

2010; de Groot-Hedlin et al., 2010], the signal was likely attenuated before reaching station IS07. Subsequently, the highest number of detections on Figure 3.6 are the result of microbarom clutter, and no detection packets are visible from the direction of Anak Krakatau at IS07.

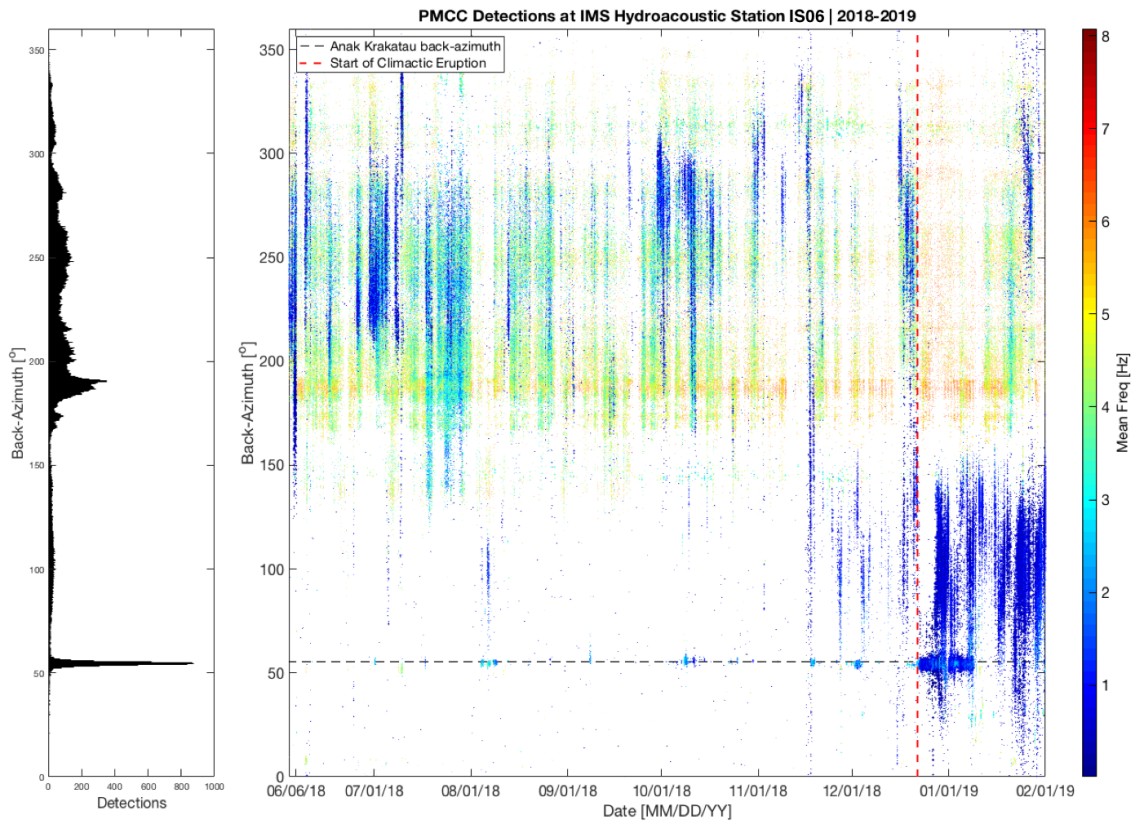


Figure 3.4: PMCC array processing bulletin detections for infrasound station IS06, from June 5, 2018, through January 31, 2019. The dashed black line indicates the back-azimuth direction of Anak Krakatau, and the dashed red line indicates the date of the start of the climactic eruption phase. The plot shows detections intermittently during the 6 months leading up to the climactic phase, and a large number of detections during the climactic phase from December 22, 2018 through January 5, 2019. Left: histogram plot of number of PMCC detections for each back-azimuth, with the largest spike in detections in the direction of Anak Krakatau.

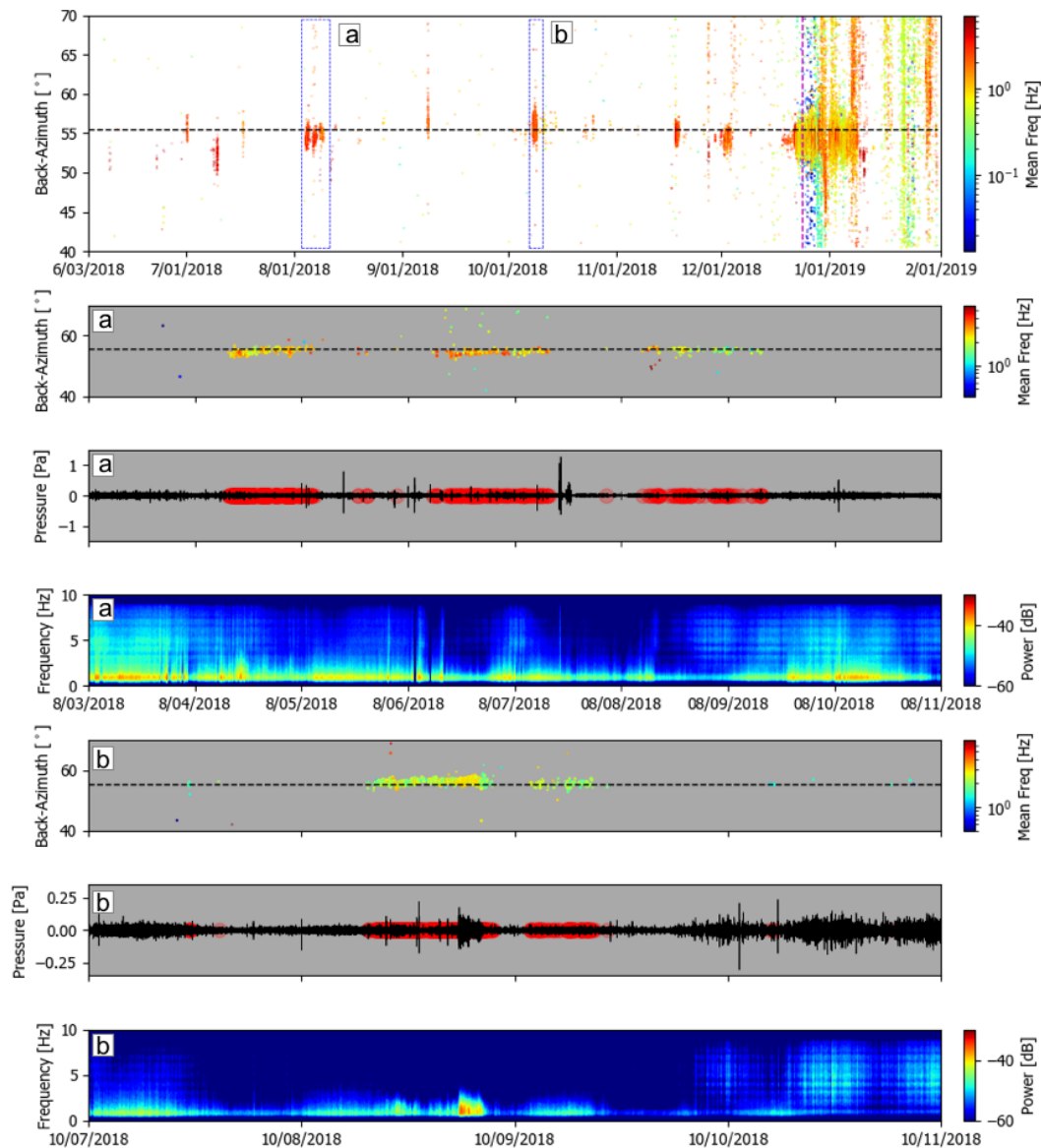


Figure 3.5: Station IS06 infrasound detections of eruptive activity in the months prior to the flank collapse at Anak Krakatau. The first panel presents PMCC bulletin detections for infrasound activity at Anak Krakatau from June 1, 2018, through January 31, 2019. Two sequences of eruptive infrasound in the months prior to the flank collapse are highlighted blue dashed rectangles and detailed in the lower panels. Panels 2-4 show PMCC bulletin detections, the waveform, and spectrogram for activity sequence **a** from August 3-11, 2018. Panels 5-7 show PMCC bulletin detections, the waveform, and spectrogram for activity sequence **b** from October 7-11, 2018. The waveforms and spectrograms were beamformed and high-pass filtered at 0.7 Hz to remove low-frequency microbarom clutter. The horizontal black dashed lines on each PMCC detection figure show the back-azimuth direction of Anak Krakatau, and the red circles on the waveforms represent PMCC bulletin detections that were within $\pm 3^\circ$ of the Anak Krakatau back-azimuth.

PMCC bulletin detections for infrasound station IS52 are plotted on Figure 3.7. At station IS52, microbarom clutter dominates the PMCC bulletin detections (Figure 3.7). However, there is a distinct increase in detections from the back-azimuth of Anak Krakatau at approximately twice the expected background number, indicating that some activity was captured by IS52 from the volcano.

Figure 3.8 compares PMCC bulletin results for the three infrasound stations for the timeframe of the main eruption, flank collapse, and ensuing Surtseyan eruption. A strong infrasonic signal is visible at IS06 from the Anak Krakatau back-azimuth, which evolves noticeably from higher mean frequency content to lower mean frequency content at the time of the flank collapse. The change in frequency content is likely due to a change in morphology at the vent, with larger diameter vents producing lower frequency infrasound than smaller diameter vents [Seiner, 1984]. Figure 3.8 also shows higher frequency pulses during the later Surtseyan activity. At IS52, there is a band of consistent detections present underneath the microbarom clutter that arrive from $\sim 5^\circ$ clockwise of the true back-azimuth of the volcano, which we interpret as volcanic signal with a typical azimuth deviation caused by atmospheric effects (e.g., Matoza et al. [2011a], Matoza et al. [2018]). The detections at station IS52 begin ~ 26 hours after the detections at IS06 first appear, a delay likely caused by low SNR at IS52.

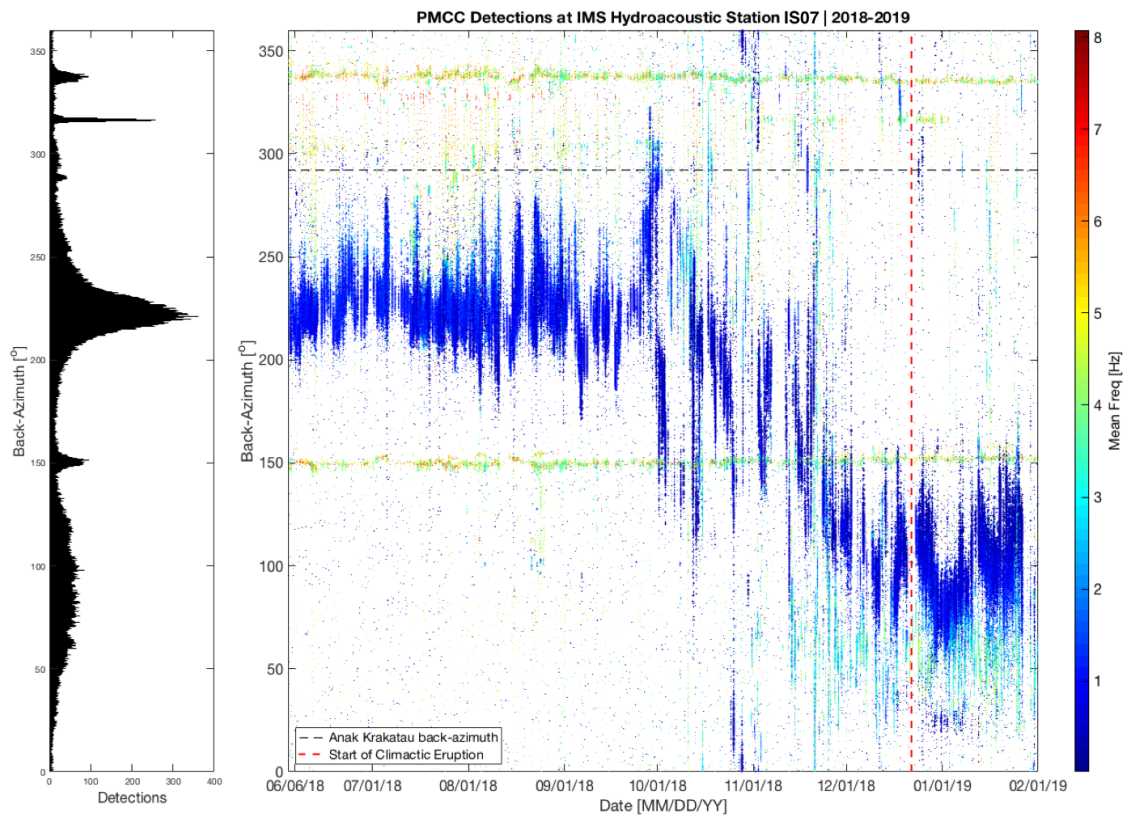


Figure 3.6: PMCC array processing bulletin (summary) detections for infrasound station IS07, from June 5 through January 31, 2019. Though there are short-duration detections at this station from the Anak Krakatau back-azimuth, including low-frequency detections in the days after the flank collapse (dashed red line), these are not continuous enough along the Anak Krakatau back-azimuth (dashed black line) to distinctly separate from background clutter. Seasonally changing clutter from low-frequency (~ 0.1 - 0.5 Hz) microbaroms (dark blue) is present throughout the timeframe, which may be caused by open-ocean swells generated by seasonally changing ocean storm patterns [Evers and Haak, 2001; Garcés et al., 2004; Le Pichon et al., 2006]. The continuous higher frequency detections from 150° and 340° are likely anthropogenic clutter. Left: histogram plot of the number of PMCC detections for each back-azimuth. No significant increase in detections is visible from the direction of Anak Krakatau.

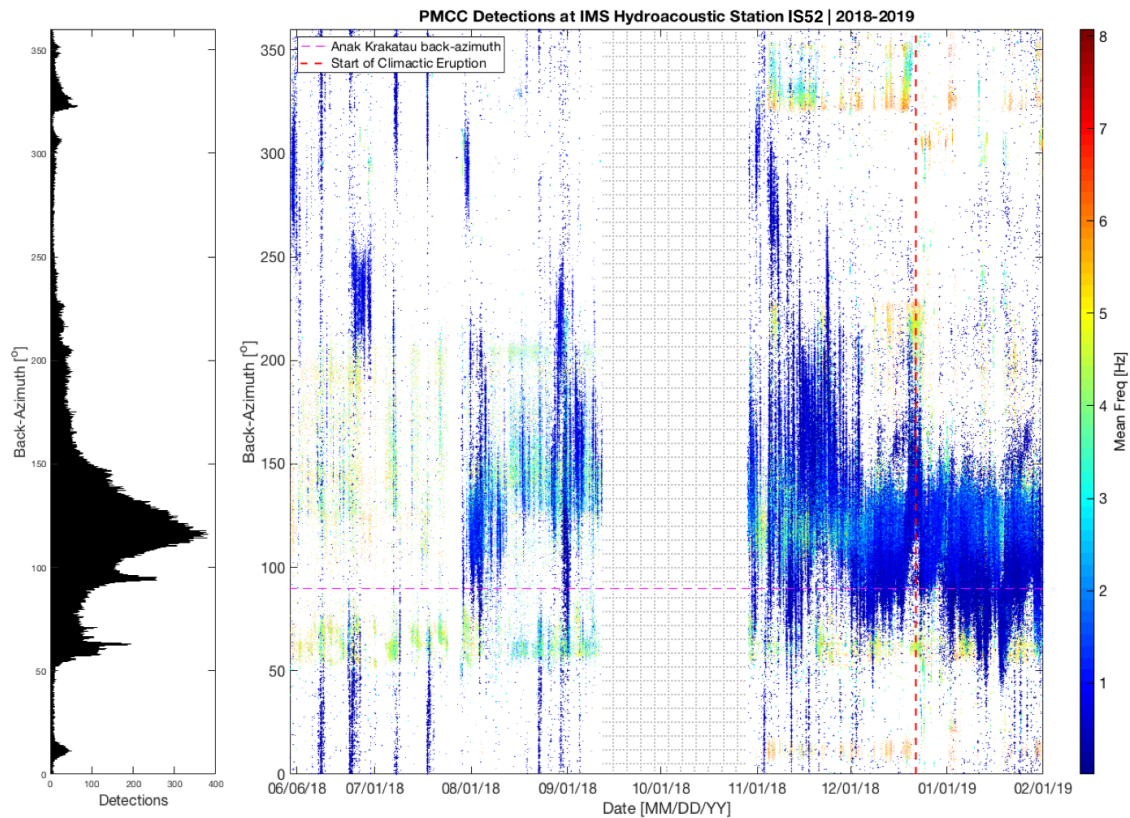


Figure 3.7: Right: PMCC array processing bulletin (summary) detections for the infrasound station IS52, from June 5 through January 31, 2019. The $< \sim 2$ Hz detections which are distributed mainly across the $\sim 50^\circ$ - 200° range are interpreted as clutter from microbaroms. This microbarom clutter obscures the time of the flank collapse at the Anak Krakatau back-azimuth on this plot, but detections from Anak Krakatau are visible when zoomed into the time and back-azimuth range of the volcano (see Figure 3.8). Data was not available from September 13 through October 27 (gray hatched area). Left: histogram plot of the number of PMCC detections for each back-azimuth. Though the most detections are from the microbarom clutter, there is an increase in detections from the back-azimuth of Anak Krakatau on the histogram.

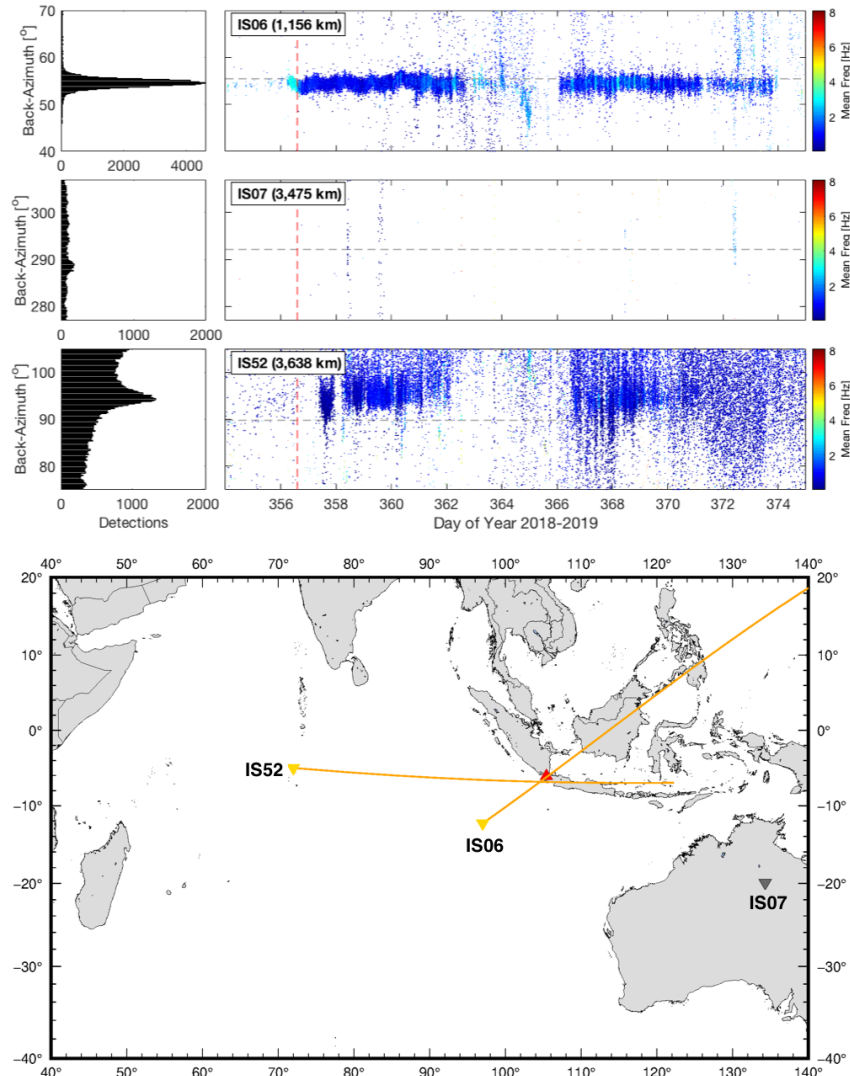


Figure 3.8: Comparison of PMCC bulletin detections at stations IS06, IS07, and IS52. The upper three panels show ± 15 degrees from each respective Anak Krakatau back-azimuth (black dashed lines), with a vertical red dashed line indicating the flank collapse event. A large number of detections are present at station IS06, beginning on day 356 (December 22, 2018) and continuing to early January 2019. Station IS07 does not show sustained detections from Anak Krakatau. Station IS52 detected continuous detections near the correct back-azimuth of the volcano for this time frame, though these don't capture the start of the eruption or flank collapse and are partially obscured by microbarom clutter. Bottom panel: detection cross-bearings for the two infrasound stations where coherent detections were observed. The mean back-azimuth of PMCC detections attributed to Anak Krakatau were calculated for IS06 and IS52, and the great circle paths at those back-azimuths are indicated by solid orange lines. The location of Anak Krakatau is indicated by a red triangle. The back-azimuth intersection location is 124 km from true. Station IS07 is indicated by a gray inverted triangle and no detection path shown due to lack of coherent sustained infrasound from the eruption at this station.

3.3 Hydroacoustic Data and Chronology

Of the three IMS hydroacoustic stations located in the Indian Ocean, we use only H01W and H08S in this study, located at distances of 3,307 km and 3,720 km from Anak Krakatau, respectively (Figure 3.2). Both stations consist of a triplet of hydrophones in a triangular configuration with ~ 2 km horizontal separation between each station, moored at or near the SOFAR channel axis. We exclude hydrophone station H04 due to preliminary analysis showing no identifiable hydroacoustic signal from the Anak Krakatau direction recorded at this station. Of the two sensor triplets of station H08, we use only the southern triplet H08S due to lack of available data for the northern triplet H08N at the Incorporated Research Institutions for Seismology (IRIS) Data Management Center (DMC).

We analyze hydroacoustic and infrasound data for the 8 months from the beginning of the new eruptive phase in June 2018 through January 2019 using waveforms, spectrograms, and PMCC array processing to detect coherent signal from the direction of Anak Krakatau. Waveforms and spectrograms from hydroacoustic stations H08S and H01W were inspected for signs of the climactic eruption phase or evidence of the flank collapse or tsunami, but no clear signal from these events was detected in the < 120 Hz frequency range allowed by the 250 Hz sample rate of the hydroacoustic sensors (Figure 3.9). This is consistent with the conclusions of Perttu et al. [2020], and may be caused by one or more factors: that the climactic eruption period was predominantly subaerial and did not produce significant hydroacoustic energy, did not radiate sound at sufficient angle or depth to be captured and guided by the SOFAR channel, or that background noise at the hydroacoustic stations obscured the signal.

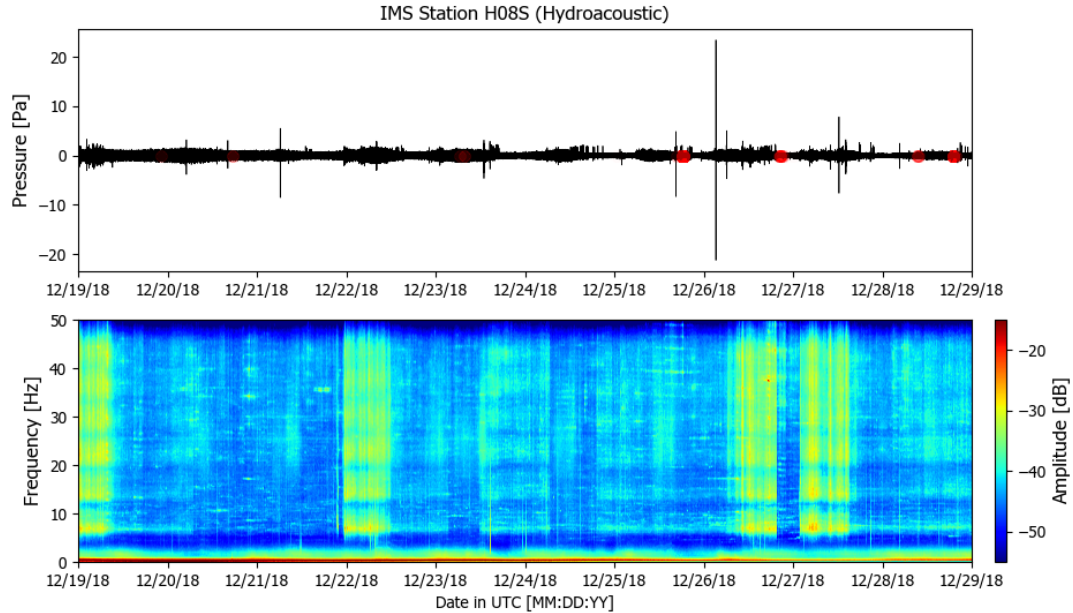


Figure 3.9: Hydroacoustic waveform and spectrogram of H08S for 10 days around the time of the main eruption and flank collapse on December 22, 2018. We applied a 0.5 Hz high-pass filter to the hydroacoustic data and beamformed the data to reduce noise. The spectrogram is raw, from sensor H08S3 which had the highest signal-to-noise ratio. Red circles on the waveform represent PMCC detections from the Anak Krakatau direction $\pm 3^\circ$, and do not appear to show sustained, coherent signal from the main eruption phase. The ~ 12 -hour broadband signals on the spectrogram are likely marine seismic airgun surveys in the Indian Ocean (see Section 3.3.2).

We perform PMCC array processing on the 8 months of data for H08S and H01W, and the bulletin detection results for H08S and H01W are presented on Figures 3.13 and 3.14, respectively. PMCC results confirm that these stations did not record the main eruption or flank collapse. However, detection results show a 12 day long swarm of nearly continuous hydroacoustic signals arriving at H08S from the back-azimuth of Anak Krakatau (89.4°) beginning 24 days before the flank collapse and tsunami, from November 29 through December 11, 2018 (Figure 3.11). Hydroacoustic waveforms and spectrograms corresponding to these detections show discrete impulsive signals from the back-azimuth of Anak Krakatau from November 29 through December 11 at station H08S

(Figure 3.10). From November 30 through December 4, 2018 consistent detections also arrived at H01W from approximately the Anak Krakatau back-azimuth from this station of 342.3° . We interpret this sequence as a submarine eruption signal due to several characteristics which are discussed below.

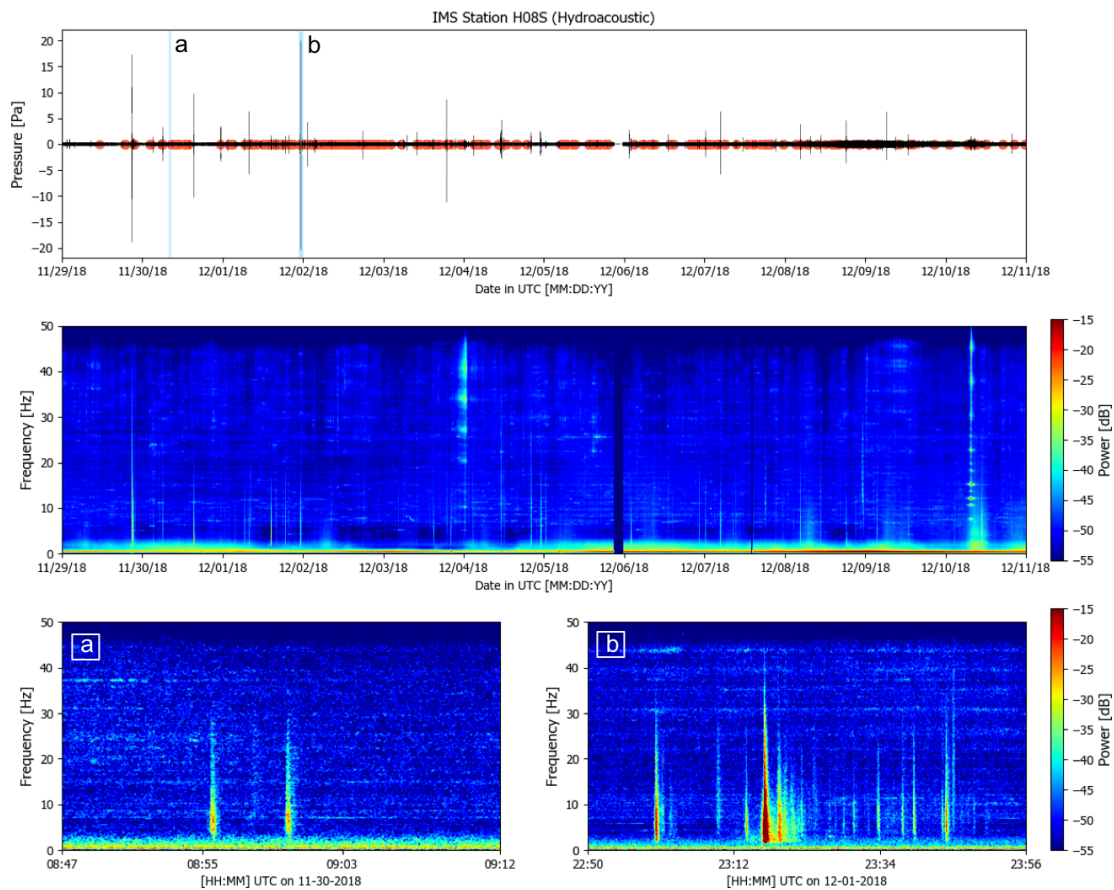


Figure 3.10: Hydroacoustic waveform and spectrogram of H08S data from November 29, 2018 to December 11, 2018, encompassing 24-12 days before the onset of the climactic eruption and flank collapse. The raw waveform and spectrogram have been beamformed to reduce noise. Red circles on the waveform indicate coherent PMCC detections from the direction of Anak Krakatau, indicating submarine eruption activity was occurring during this time. The light blue lines on the waveform panel correspond to the zoomed-in panels (a) and (b) on the bottom of the figure. These panels show that the hydroacoustic events with corresponding PMCC detections tend to be band-limited from ~ 1 -40 Hz.

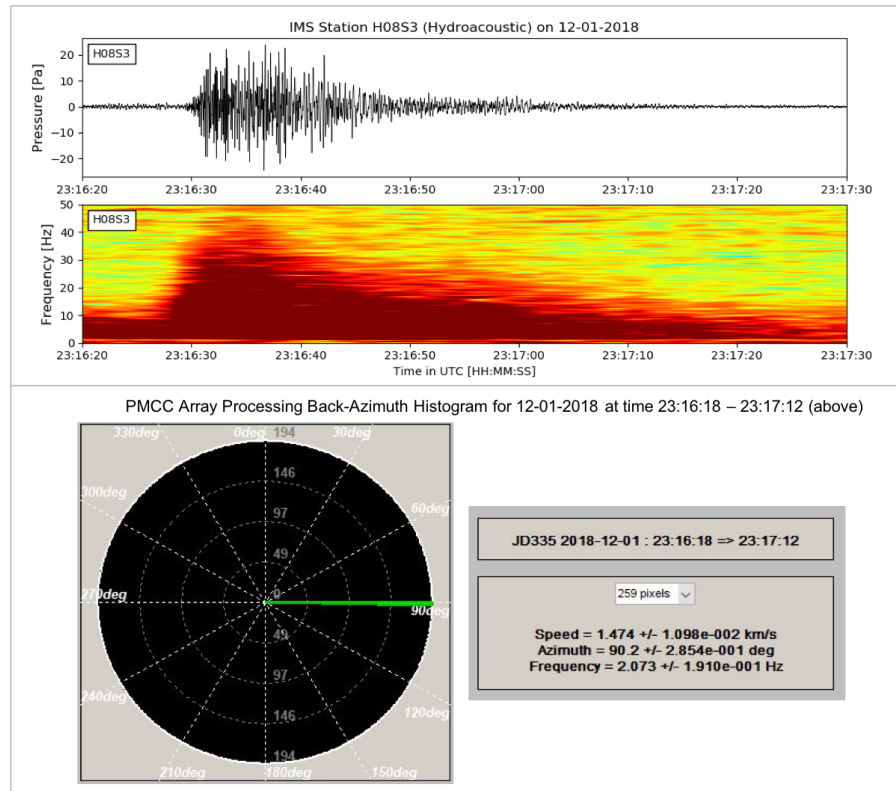


Figure 3.11: Top: hydroacoustic waveform and spectrogram for a time-windowed explosion signal on December 01, 2018, recorded by IMS station H08S3. Bottom: Corresponding WinPMCC back-azimuth histogram, showing the average back-azimuth, speed, and frequency of the signal.

In addition to possible volcanic signals, many types of hydroacoustic clutter are observed. At station H08S, bands of clutter are visible at approximately 30°-40° and 50°-60° back-azimuth, which we interpret as noise generated by ships traversing the Strait of Malacca at the northern tip of Sumatra, where 30% of the world’s trade passes each year [UNCTAD, 2015], as well as noise from marine seismic surveying and other anthropogenic noise. The band of clutter at ~140°-220° on station H08S is consistent with iceberg cracking and calving in the southern Indian Ocean found by Evers et al. [2013] (Figure 3.12), which used satellite observations and hydroacoustic data from the same two IMS stations to monitor iceberg breakup. Detections which transit across a range

of back-azimuths are interpreted to be passing ships or marine wildlife such as whales, as these sources move through the oceans whereas volcanoes remain in a single location emitting a continuous signal from a one back-azimuth direction.

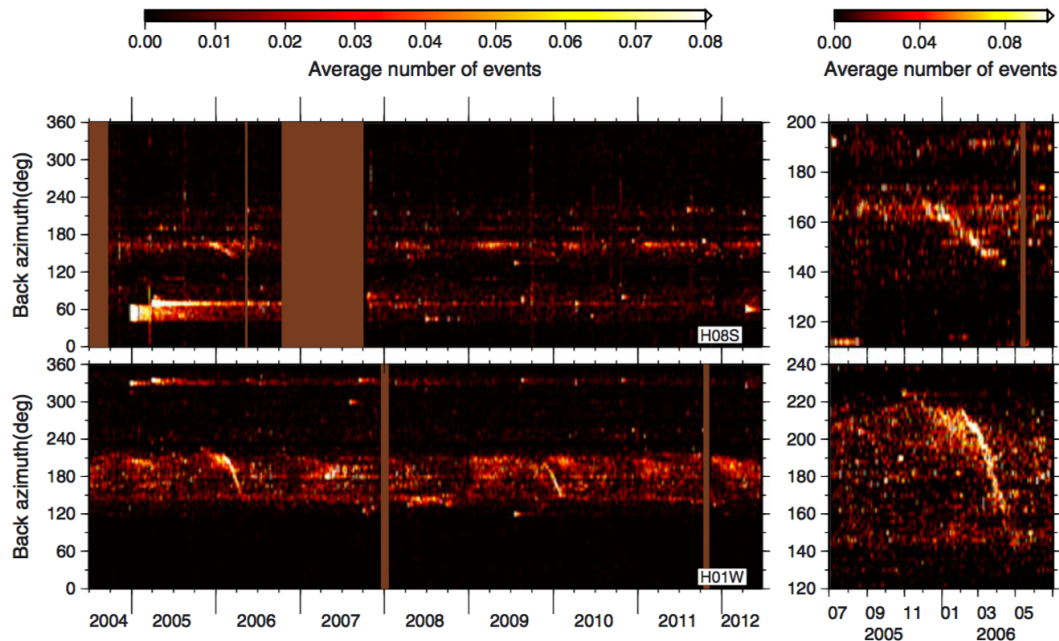


Figure 3.12: Figure reproduced and modified from Evers et al. [2013] showing the IMS International Data Center detections at stations H08S and H01W from July 1, 2004, through June 21, 2012 on the left panels and July 1, 2005 to July 1, 2006 on the right panels. Evers et al. [2013] compared the detection back-azimuths vs time to satellite imagery and found that they corresponded to movements of large iceberg transportation and breakup in the southern Indian Ocean.

At station H01W, the majority of PMCC bulletin detections are attributed to southern Indian Ocean iceberg cracking and breakup, which is again consistent with iceberg signals detected at this station by Evers et al. [2013] from 2004 to 2012. The visible increase in detections in the last weeks of 2018 through the beginning of 2019 corresponds with the signal seasonality seen by Evers et al. [2013], as the Austral summer causes warmer conditions and accelerated iceberg calving and breakup and produces more frequent and powerful hydroacoustic noise. We attribute signals which transit across a range

of back-azimuths to shipping and marine animal noise, similar to that seen at station H08S.

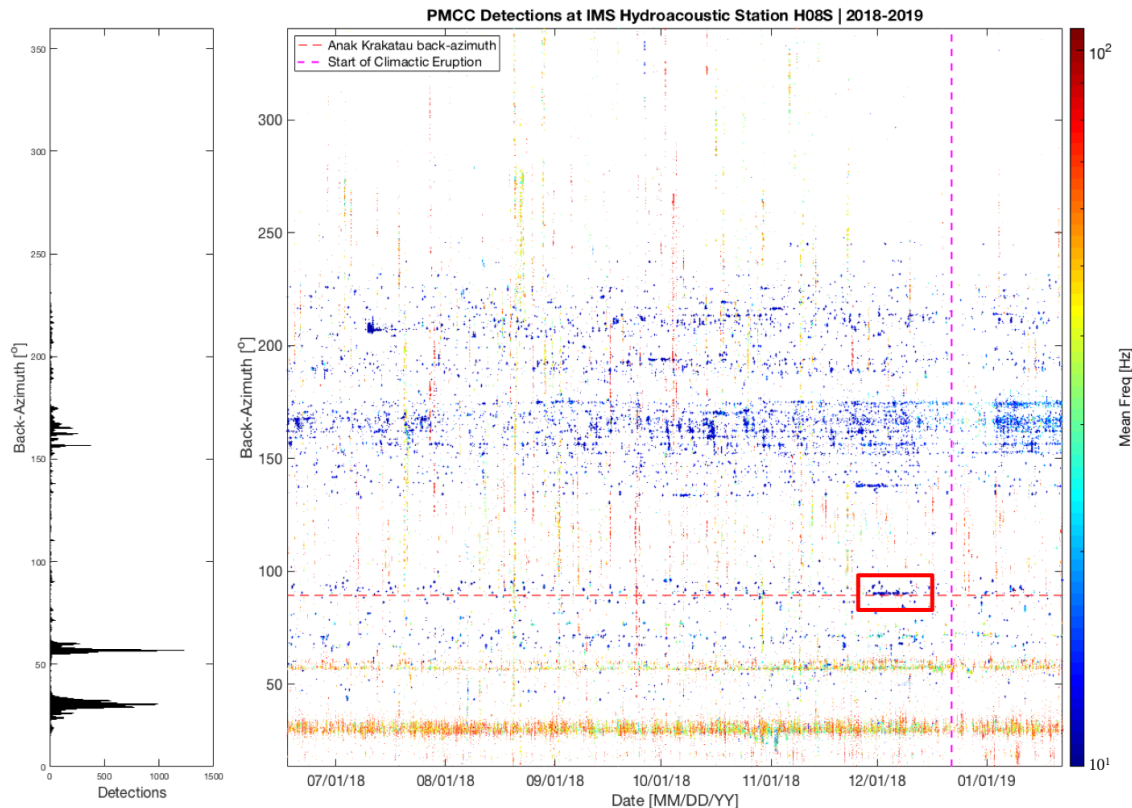


Figure 3.13: PMCC bulletin detection results for hydroacoustic station H08S, with colors representing mean frequency of the signal detections in log scale to give contrast, and detections with mean frequency less than 10 Hz removed to reduce clutter. The solid red box shows the location of the 12-day hydroacoustic swarm signal from Anak Krakatau. We also observe intermittent low-frequency detections from June to December of 2018 in the Anak Krakatau back-azimuth direction, but cannot confidently interpret these as hydroacoustic signals from Anak Krakatau because they are not sustained and therefore may be clutter from other sources such as seismic events along the Java Trench. Clutter bands centered at 30° and 60° are interpreted as shipping noise and other anthropogenic noise. There is a broad clutter band from 140° to 220° which we interpret as glacier and iceberg cracking noise in the southern Indian Ocean. Left: histogram plot of number of PMCC detections at each back-azimuth.

Figure 3.15 compares PMCC bulletin detections for the two hydroacoustic stations H08S and H01W, narrowing the field of view of the detections to the timeframe of the flank collapse and preceding weeks, and the back-azimuth to $\pm 15^\circ$ of Anak Krakatau

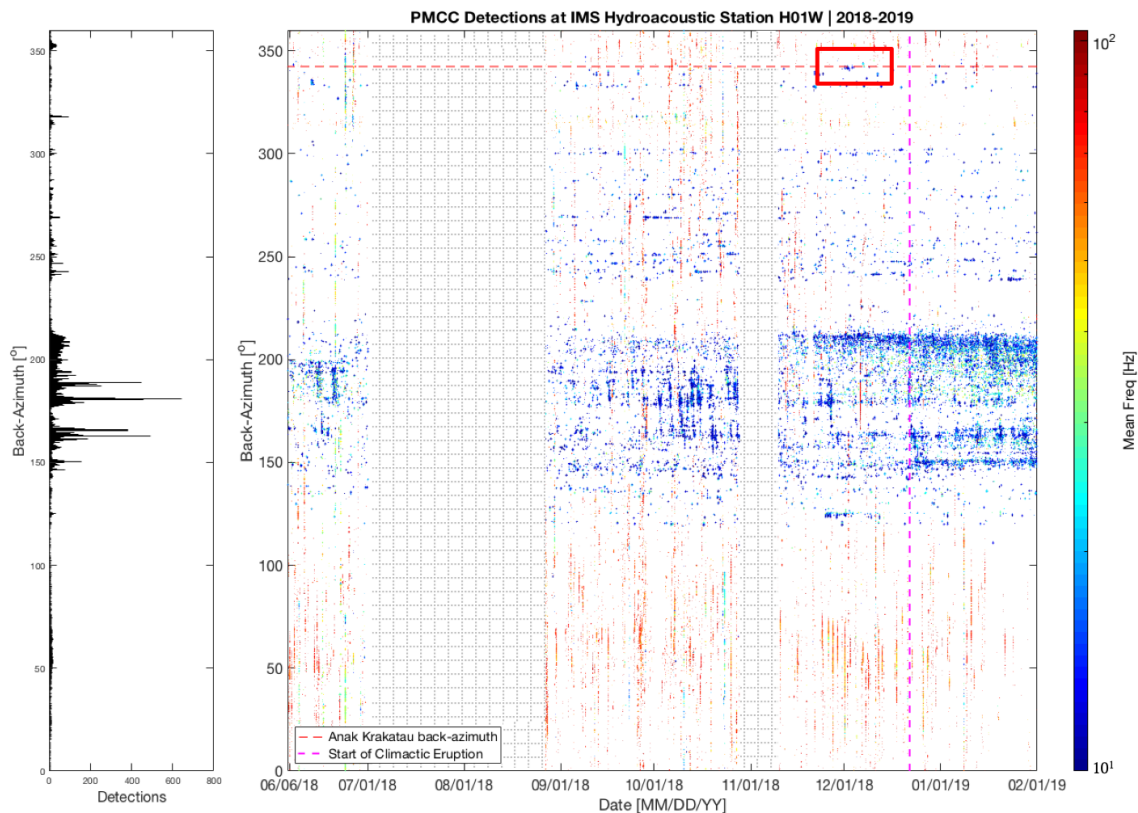


Figure 3.14: Right: PMCC array processing bulletin detections for hydroacoustic station H01W, from June 6, 2018 through January 31, 2019. The November 30 - December 4, 2018 hydroacoustic detections from Anak Krakatau are indicated by the solid red rectangle. Data was not available from July 2 through August 25, 2018 and October 29 through November 7, 2018, so no PMCC detections are shown during these date ranges. There is a broad clutter band from 130° - 220° which we interpret as glacier and iceberg noise from the direction of Antarctica. Although no continuous detections arrived from the back-azimuth of Anak Krakatau during the climactic eruption, PMCC detects hydroacoustic activity from November 30 through December 4, corresponding to the hydroacoustic swarm seen at H08S (Figure 3.13). Left: histogram plot of number of PMCC detections at each back-azimuth.

for each station. This figure shows continuous hydroacoustic detections at H08S from the volcano back-azimuth for 12 days from November 29 - December 11, 2018, and corresponding detections at H01W for a shorter period from November 30 - December 4, 2018. A shorter signal duration may have been captured at station H01W due to lower SNR or scattering by bathymetric obstructions such as seamounts, ridges, and the Cuvier Plateau in the path from volcanic source to receiver. The cross-bearings paths of

the two stations are centered near the Sunda Strait at the lower tip of Sumatra, close to the location of Anak Krakatau.

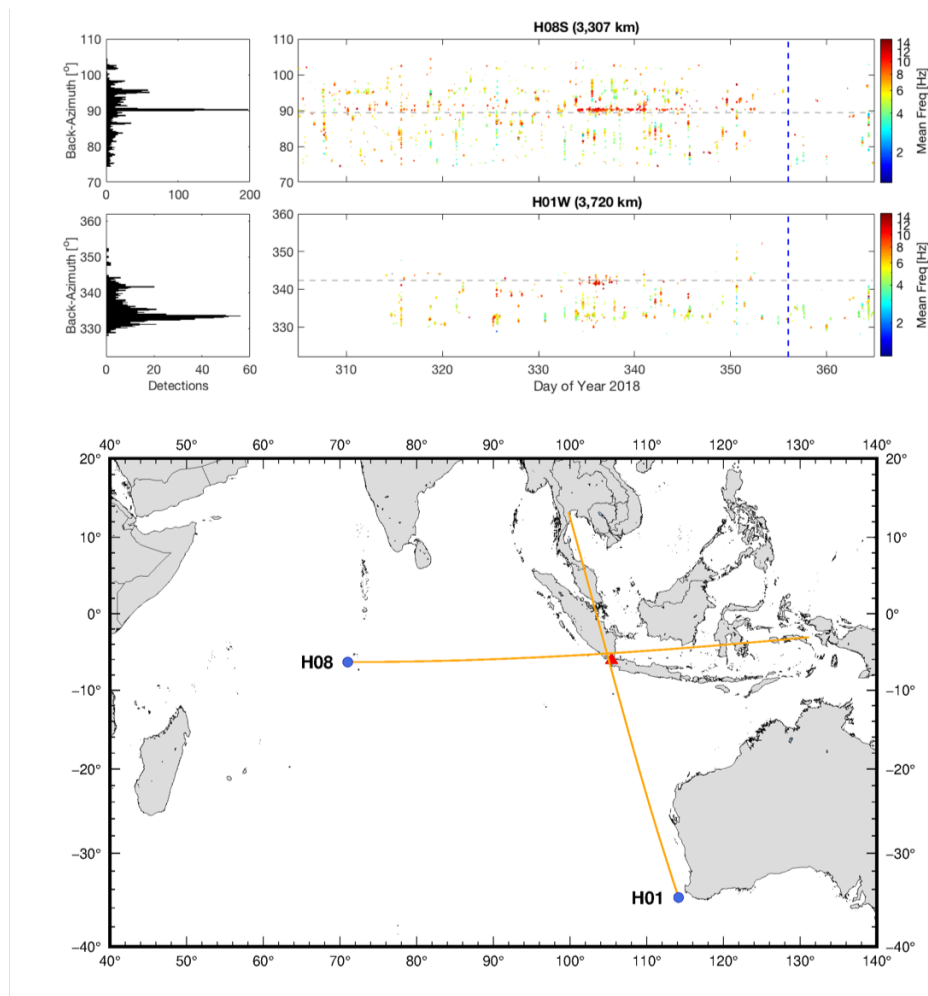


Figure 3.15: Comparison of PMCC hydroacoustic detections at H08S and H01W and detection cross-bearings. PMCC bulletin detections are present prior to the flank collapse eruption at both stations. The back-azimuth to Anak Krakatau is indicated by a gray dashed line and the time of the flank collapse is indicated by a vertical blue dashed line on each PMCC detections plot. The flank collapse eruption phase was not detected, possibly due to predominantly subaerial eruptive activity. The bulletin detections were filtered from 1 to 15 Hz mean frequency to reduce clutter (coherent signals besides the signals of interest). Bottom panel: locations of stations H08 and H01 are indicated by blue circles, and the location of Anak Krakatau is indicated by a red triangle. The mean back-azimuth of PMCC detections attributed to Anak Krakatau was calculated for each station, and the great circle paths projected in the direction of the mean back-azimuths are indicated by solid orange lines. The hydroacoustic swarm signals from the two stations overlap near the location of Anak Krakatau, 119 km from true.

3.3.1 Infrasound and Hydroacoustic Signal Comparison

PMCC bulletin detections for stations H08S (the closest hydroacoustic station) and IS06 (the closest infrasound station) show detections arriving from the back-azimuth of Anak Krakatau during two distinct temporal ranges. To increase the resolution of the hydroacoustic signal, we plotted the PMCC families detections (i.e. each pixel in each family) on Figure 3.16 and calculated the detection density (number of detections per 24 hours and 0.1 degrees back-azimuth) to resolve whether signal content changed from predominantly hydroacoustic to predominantly infrasonic over time. We observe hydroacoustic detections from November 29 through December 11, 2018 (days 333 - 345) from the back-azimuth of Anak Krakatau, while infrasound detections are only observed from November 30 through December 4, 2018 (days 334 - 338). This difference indicates that the eruption was occurring subaqueously and subaerially during this time, but continued subaqueously for 5 days longer than the subaerial component of the signal. The flank collapse and tsunami occurred on December 22, 2018 (day 356), which was not detected at the hydroacoustic station H08S, but was strongly detected at the infrasound station IS06. This indicates that the main eruption and flank collapse produced powerful infrasound but did not have a significant submarine component in the 0.5-120 Hz frequency band we investigated.

We interpret the hydroacoustic sequence as a submarine eruption signal due to several factors. Firstly, the continuous nature of the signal is consistent with a series of explosions or tremor over several days as observed at other submarine eruptions (e.g., Green et al. [2013], Metz et al. [2016], Tepp et al. [2019a]). Tectonic earthquakes, which are a major source of hydroacoustic energy in the ocean, are of much shorter duration on the order of seconds to minutes. Secondly, subaerial and submarine volcanic eruptions have fixed point source locations, and signals generated by these eruptions will originate

from approximately the same back-azimuth over the course of the eruption. In contrast, some other sources of continuous hydroacoustic energy such as passing ships or vociferous marine animals may traverse a wide range of back-azimuths.

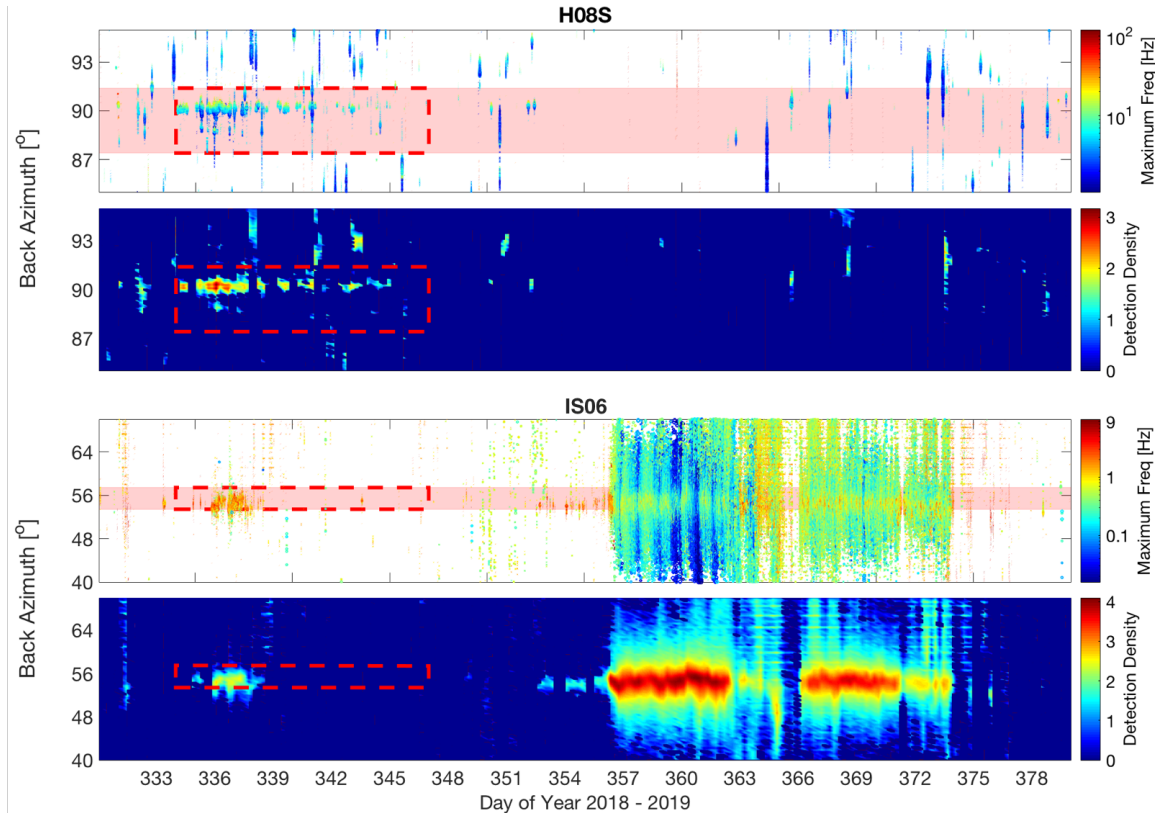


Figure 3.16: Comparison of PMCC families detections and density of detections at hydroacoustic station H08S and infrasound station IS06. H08S shows a hydroacoustic swarm extending from day 333 to 347, with no activity during the climactic phase. IS06 shows infrasound detections from day 334 to 339, partially overlapping the H08S hydroacoustic swarm, followed by a period of quietude until day 352. This is followed by 5 days of higher-frequency infrasound, and then onset of the main eruption phase and flank collapse on day 356. This suggests that activity at Anak Krakatau may have evolved from a more submarine to more subaerial in the weeks preceding the climactic phase.

The hydroacoustic signals we observe have a consistent back-azimuth, especially at H08S where a longer duration signal was detected. Thirdly, we can rule out several other sources of marine sound: the cross-bearings of both stations place the source location in the vicinity of the Sunda Strait near the equator (Figure 3.15), which makes iceberg

or glacier noise improbable. Coastal anthropogenic noise, as seen in the two fixed high-frequency noise bands on Figure 3.13, is typically continuous over the entirety of the studied time-range, which is not true of our observed hydroacoustic signal (which appears and then disappears 12 days later). This signal is also inconsistent with marine seismic surveying, which is broadband and perfectly repetitive (see Section 3.3.2 for discussion of marine seismic survey clutter in this dataset). Lastly, the temporal coincidence with the highest hydroacoustic swarm detection density with an infrasound sequence that was detected at IS06 suggests that the volcano was erupting subaerially, and could also have been erupting subaqueously. Based on these characteristics and the cross-bearings location of this signal near the location of Anak Krakatau, we interpret a submarine eruption is the most likely source of this hydroacoustic signal.

3.3.2 Marine Seismic Survey Clutter

One source of anthropogenic submarine noise is marine seismic surveying, which is characterized by sharp, consistently repeating broadband signals on waveforms and spectrograms. Marine seismic surveys use airguns to release a quantity of highly pressurized air approximately every 10 to 60 seconds, resulting in series of loud pulses at frequencies of approximately 2 to 188 Hz at the source location [Nieukirk et al., 2012]. At H08S, we observe broadband pulses arriving from 60° back-azimuth (i.e. 30° from the direction of Anak Krakatau) approximately every 20 seconds at frequencies of ~5-120 Hz, consistent with airgun survey characteristics. These consistent broadband pulses are visible intermittently the H08S hydroacoustic data, including on the day of the main eruption and flank collapse (December 22, 2018), which raised the noise floor during that time. Though these bursts are present at the highest levels for the first 12 hours of December 22, the noise continues at lower amplitude through the timeframe of the flank collapse and

tsunami and through the end of the day on December 22, suggesting a possible change in direction of the survey ship. We eliminate these pulses from consideration as volcanic signals due to their constant repetition and arrival back-azimuths inconsistent with the direction of Anak Krakatau. We also identify repetitive broadband signals interpreted as seismic airgun survey clutter intermittently throughout the 8 months of hydroacoustic data analyzed.

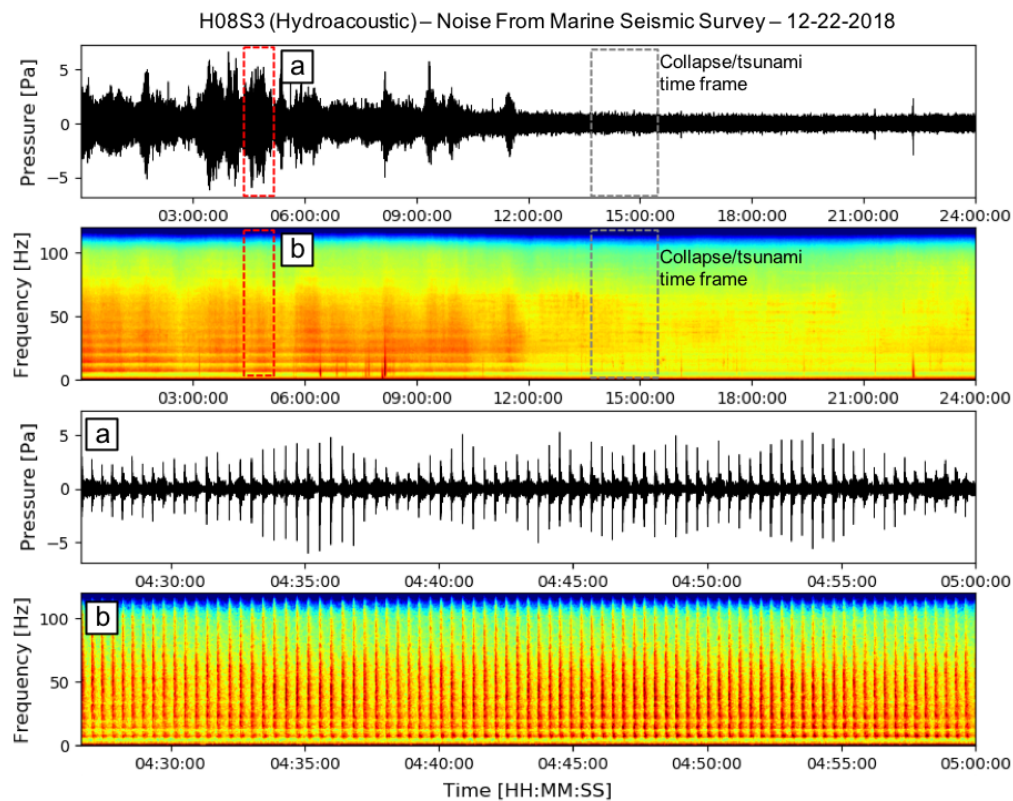


Figure 3.17: Waveforms and spectrograms from sensor H08S3 on December 22, 2018, showing repetitive broadband signal pulses which are interpreted to be from a marine seismic airgun survey. These surveys are present intermittently in the data. Panels (a) and (b) show a shorter time window from 04:25 through 05:00 UTC on which a series of repeating, impulsive airgun blasts are visible at a period of ~ 20 seconds.

3.3.3 A Check of the PMCC Method

As a check of the PMCC array processing algorithm method, a time window of hydroacoustic signal from station H08S during the hydroacoustic swarm on December 1, 2018, was beamformed and used to create an root-mean-square (RMS) grid-search plot to find best-fitting signal velocity and back-azimuth. The time-windowed hydroacoustic explosion signal and resultant beamformed signal are shown on Figure 3.18.

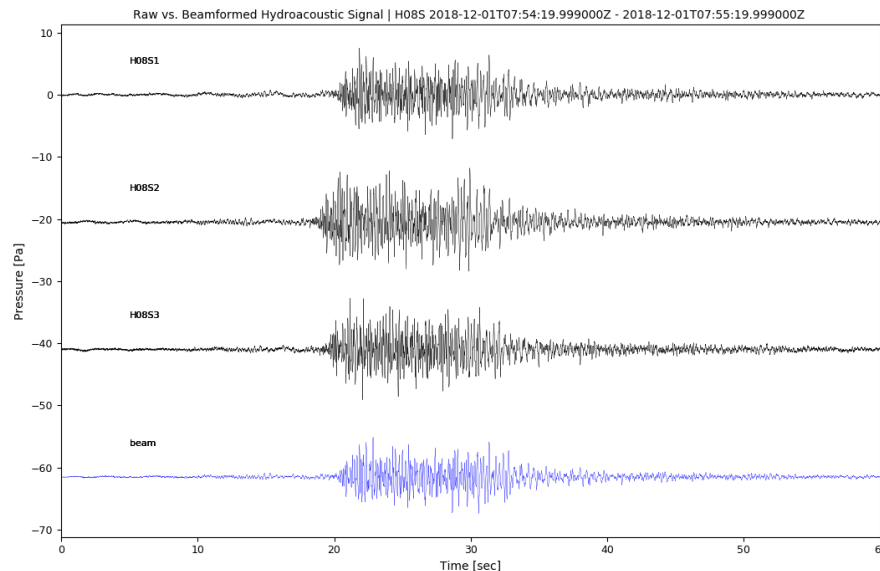


Figure 3.18: Raw hydroacoustic signal (black) from H08S triplet on December 01, 2018, during the time of the hydroacoustic swarm, compared to beamformed signal (blue) created using a time-delay beamformer to reduce noise and input from signals propagating in different directions.

Next, we applied a grid-search method using the beamformer to the explosion signal at a range of apparent velocity and back-azimuth values (Figure 3.19). We then calculated the RMS for each beamformed signal in the grid, and converted the RMS values to decibels with the accepted reference of $1 \mu\text{Pa}$ for underwater acoustics using

the following conversion formula [Jensen et al., 2011]:

$$P_{dB} = 20\log_{10}\left(\frac{P_{rms}}{\max(P_{rms})}\right) \quad (3.2)$$

The RMS decibel plot indicates that the best-fit apparent velocity is 1525 m/s, which is within the expected realm for a long-distance hydroacoustic signal, and the best-fit back-azimuth is approximately 90.8 degrees, which is in agreeance with the PMCC estimate of approximately 90.2 average back-azimuth, providing a check for the PMCC algorithm and providing guidance on the angular resolution.

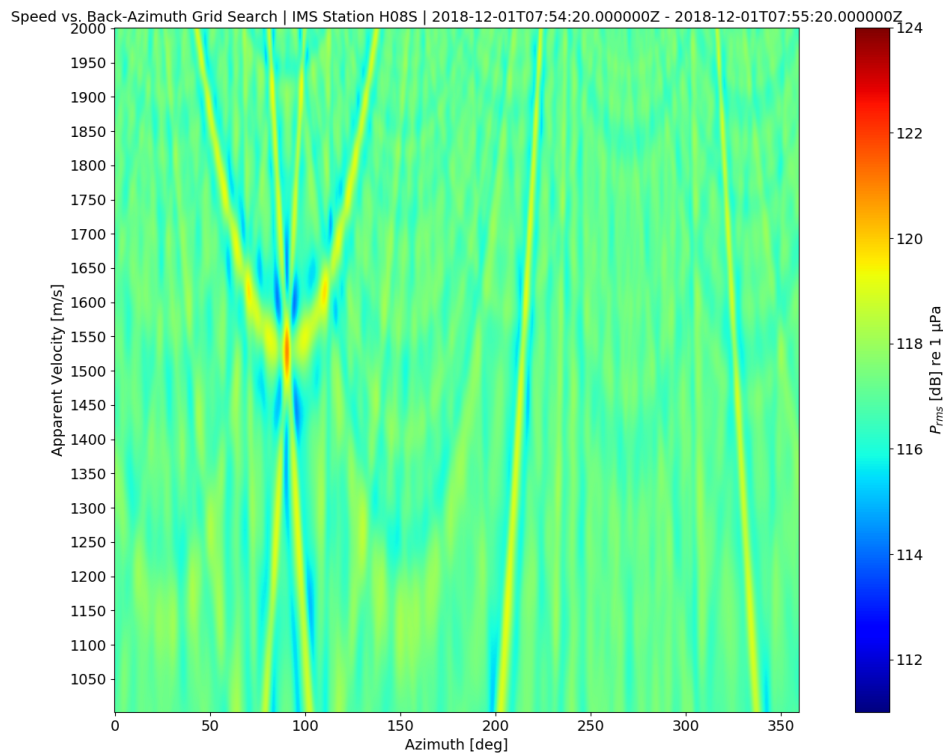


Figure 3.19: Grid search plot showing the best-fit hydroacoustic velocity and back-azimuth for the explosion signal from Figure 21. The signal was beamformed using possible velocity values of 1000 m/s to 2000 m/s and back-azimuths 0°-360°, and the RMS value of the beam calculated for each velocity-azimuth pair. The resulting RMS values for acoustic pressure were converted to decibels, with the warmest colors indicating the best-fitting velocity and azimuth of the signal.

Waveform Cross Correlation and Clustering

Waveform similarity (multiplet) analysis has been used for seismic data at subaerial volcanoes to identify stable low-frequency earthquake sources [Stephens and Chouet, 2001; Green and Neuberg, 2006; Petersen, 2007; Matoza and Chouet, 2010] and with acoustic data at submarine volcanoes to classify generation mechanisms of hydroacoustic events [Green et al., 2013]. Highly repetitive events which exhibit strongly correlated waveforms suggest a distinct, stable, non-destructive source, with the energy propagating along an almost identical path to reach the sensor. Events for which the waveforms evolve over time reflect a changing source pressure, geometry, or source location (e.g., Stephens and Chouet [2001]). We apply this method following Green and Neuberg [2006] and Green et al. [2013] to both infrasound and hydroacoustic signals from Anak Krakatau to investigate waveform similarity and resolve whether physical eruption processes may be linked to systematic changes in the waveform shapes produced.

4.1 Infrasound Waveform Similarity

4.1.1 Infrasound Event Selection

To investigate waveform similarity, we use the network short-term average/ long-term average (STA/LTA) method to detect events within continuous IS06 infrasound signal. Network STA/LTA calculates the ratio between the short-term average and the long-term average amplitude of the signal at each sensor in the network in moving time windows to automatically pick events when amplitude ratios that exceed a specified threshold value. For this analysis, we use the elements of station IS06 as if they are a ‘network’. Six of the seven sensors of IS06 had to be individually triggered for the signal to be recorded to the master event list. During preliminary work using this method, some erroneous events were detected which did not correspond to PMCC detections. To remediate this, all event triggers which did not fall within the time window of a PMCC bulletin detection ± 10 seconds at IS06 were discarded. A series of STA/LTA ratios, time window lengths, filters, and trigger ratio thresholds were also tested to determine which combination produced the clearest result. This method was used to identify all events which could be associated with eruption activity at Anak Krakatau, without regard for event waveform shape similarity.

This network STA/LTA plus PMCC cross-check method was applied to 10 days of picked infrasound events from December 19 - 29, 2018, with an STA/LTA ratio of 3/40s and a trigger ratio threshold of 1.5. The events were windowed from 1 second prior to the trigger time to 5 seconds post-trigger. This window length was chosen to record individual events, but avoid interference from neighboring events. The signal was pre-filtered with a 0.7-4 Hz Butterworth bandpass filter to reduce noise from microbaroms and because this band contains the majority of the signal power from the eruption (Figure 4.1).

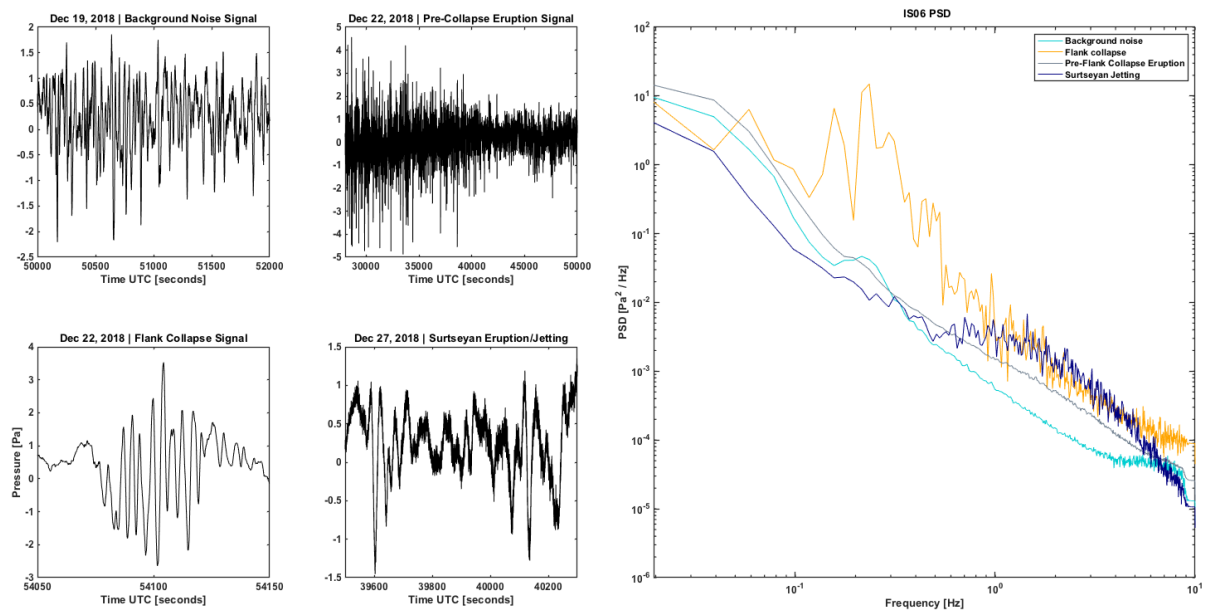


Figure 4.1: Waveforms recorded at IS06 for background noise, the intense Strombolian pre-collapse eruption, the flank collapse signal, and Surtseyan eruption activity. Power spectral densities (PSDs) for each of the signal windows are shown in the panel on the right, with a background noise spectrum shown for comparison. The flank collapse signal has a strong low-frequency component which significantly exceeds the noise floor, while the pre-collapse and Surtseyan eruptions are stronger in higher frequencies.

Figure 4.2 shows an example one day of signal from December 22, 2018, the day of the start of the climactic phase and flank collapse. PMCC bulletin detections are plotted at their respective positions along the waveform, and triggered events are shown by blue vertical lines. As shown, only triggered events corresponding to PMCC bulletin detections were kept. There is a scattering of events in the first two hours of the figure, and then approximately 4 hours of noise with no PMCC detections, wherein no event triggers were logged. The climactic eruption phase began at approximately 06:40 UTC [Perttu et al., 2020]. On Figure 4.2, the infrasound PMCC detections become consistent and the amplitude of the waveform increases. The flank collapse and tsunami reportedly occurred between 13:55-14:00 UTC [Perttu et al., 2020], and the PMCC signals become less consistent and more sporadic.

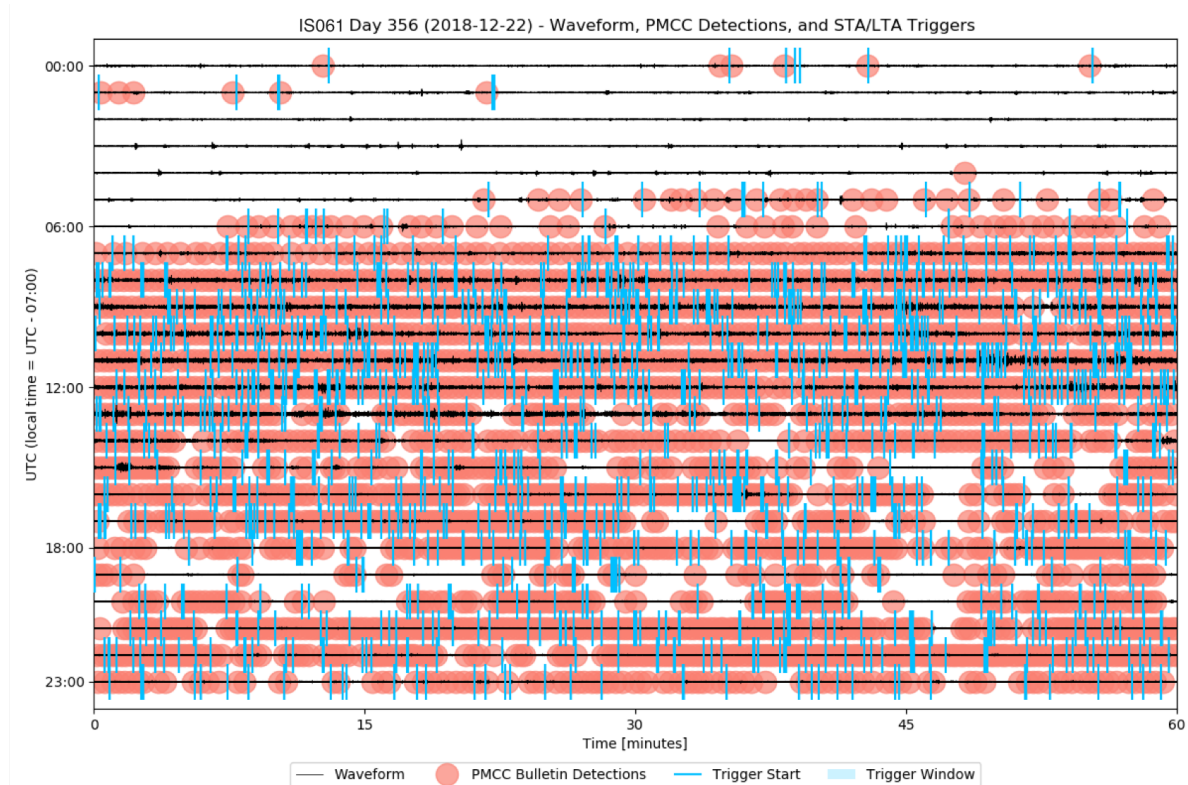


Figure 4.2: Example dayplot of 24 hours of IS06 infrasound waveform data, with PMCC bulletin detections identified by pink circles, triggered event start times indicated by blue vertical lines. Events were only triggered if they corresponded to PMCC bulletin detections ± 10 s. A period of quiescence with occasional intermittent PMCC detections is visible until around 06:00-07:00, at which point the signal becomes more consistent and the signal amplitude increases. The climactic eruption occurred from 06:40 to $\sim 13:55$ UTC, with the flank collapse and tsunami occurring from 13:55-14:00 UTC [Perttu et al., 2020], after which the signal amplitude decreases and becomes slightly less consistent.

This method produced an event detection list of 10324 events, which were then used for waveform cross correlation analysis. The events are plotted by maximum amplitude on Figure 4.3, and four satellite images are shown for reference. A period of weak, intermittent activity was present from December 19 to December 22, during which the satellite imagery shows the volcanic edifice and cone was still intact. Then on December 22 the events became strong and consistent with increased amplitudes, corresponding to a period of intense Strombolian activity reported at the volcano. Event amplitudes decreased sharply with the flank collapse, with the first post-collapse satellite imagery

8 hours later showing that at least one large landslide had carried a sizable section of the flank into the ocean. The satellite image shows concentric rings in the seawater around Anak Krakatau, possibly caused by continuing mass-wasting at the volcano or expanding base surges. After the flank collapse, the eruption entered a period with a continuous, pulsing ash plume, explosions, base surges, and Surtseyan phreatomagmatic activity [Global Volcanism Program, 2019], corresponding to sharp event amplitude peaks on Figure 4.3. One possible cause of the high-amplitude pulses from December 26 to 28 is that there was Surtseyan jetting of material as the vent was inundated with seawater, as these pulses exhibit a broader frequency range than the background volcanic signal during this timeframe. The final SAR satellite image, taken at 22:41:40 UTC, shows the submerged vent of Anak Krakatau began to close off from seawater as tephra was deposited around the vent. By January 2, 2019, the tephra formed a rim which barred ocean water from entering the vent and formed a crater lake where Surtseyan activity continued continuously until mid-January (infrasound from this Surtseyan activity is visible in the PMCC detections on 3.4, as well as observed by eyewitnesses at the volcano [Global Volcanism Program, 2019]).

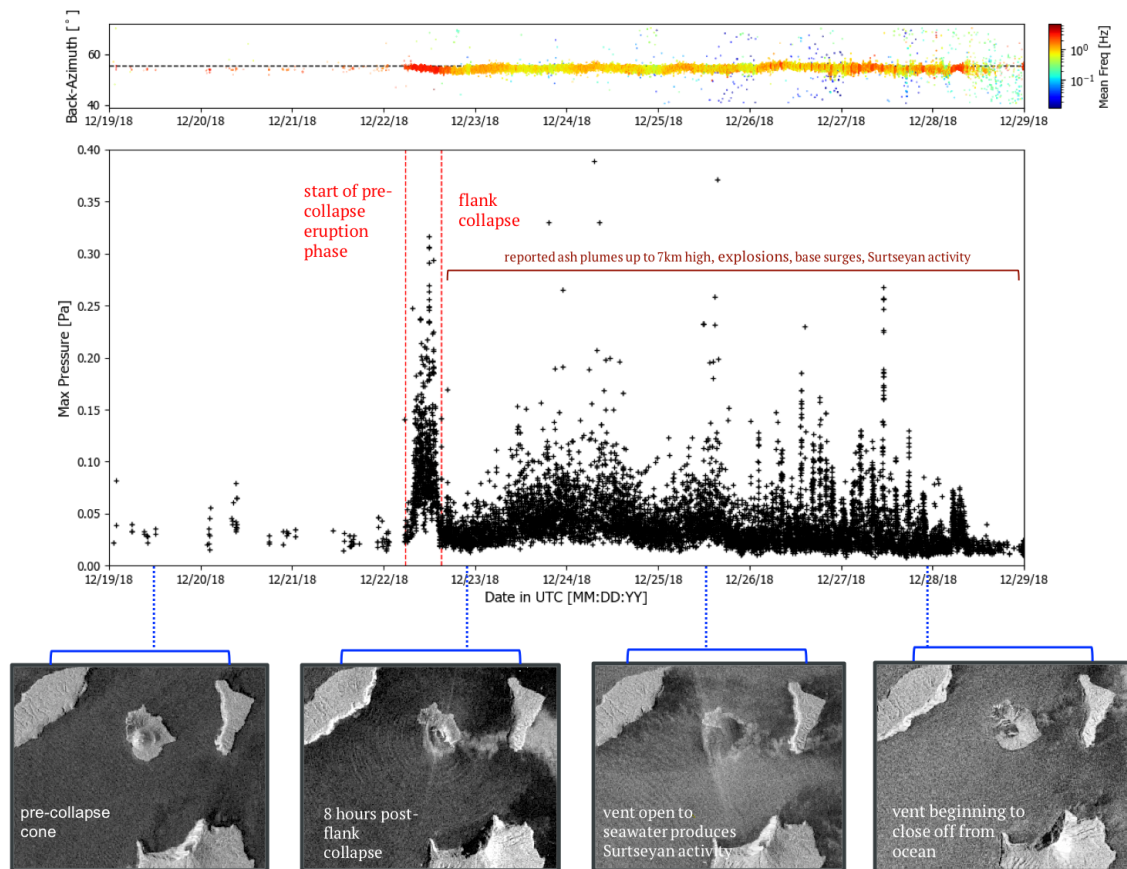


Figure 4.3: Summary of IS06 infrasound events from December 19 - 29, 2018. Top panel: PMCC bulletin detections, with colors representing mean frequency of the detection in log scale. The black dashed line is the back-azimuth of Anak Krakatau, 55.5° . Middle panel: the 10324 infrasound events picked using a network STA/LTA with PMCC cross-checking method. The events are plotted by maximum amplitude of the signal. The sustained high-amplitude sequence of events on December 22 represents the climactic eruption phase, and amplitude decreases upon the collapse of the flank. Subsequent events likely represent a sustained ash plume, base surges, explosions, and Surtseyan activity that were reported by eyewitnesses [Global Volcanism Program, 2019]. The row of panels below show Sentinel-1 synthetic-aperture radar (SAR) ground range detected (GRD) satellite imagery captured at intervals throughout the eruption [Modified Copernicus Sentinel Data, 2019].

4.1.2 Infrasound Event Cross-Correlation

We calculate event similarity using cross-correlation for each of the 10324 waveforms included in the IS06 event detection list, using the cross correlation function:

$$\rho_{xy}(i, i-l) = \frac{\sum_{i=1}^n (x_i - \bar{x})(y_{i-l} - \bar{y})}{\sqrt{\sum_{i=1}^n (x_i - \bar{x})^2} \sqrt{\sum_{i=1}^n (y_{i-l} - \bar{y})^2}} \quad (4.1)$$

where ρ_{xy} is the cross-correlation value, x_i is the i^{th} sample of signal x , y_{i-l} is the $i^{\text{th}} - l$ sample of y (where l is the lag number of samples between signals x and y), \bar{x} is the mean value of signal x , \bar{y} is the mean value of signal y , and n is the number of samples of the windowed signals. Using this function as a measurement of similarity, we employ an algorithm which cross-correlates each waveform with every other waveform in the event list, normalizing the waveforms to quantify waveform shape but disregard the amplitude of the events. This allows quantitative comparison of the source variability of the events, but not of their magnitude.

Two events that are perfectly correlated will produce an ρ_{xy} value of 1, and events that are entirely uncorrelated will have an ρ_{xy} value of 0. As the sample lag value l is changed, the position of signal y with respect to signal x is varied, and the correlation is recorded at each position. We log the maximum correlation coefficient value between each pair of signals and the lag l at the maximum correlation, and use the cross-correlation values to build a maximum correlation coefficient matrix with m rows and m columns, where m is the number of events in the list, in this case 10324 events (Figure 4.4). This cross correlation shows that the events identified during the intense Strombolian pre-collapse eruption had generally low correlation values, so were not highly repetitive within the 6-second interval of the events.

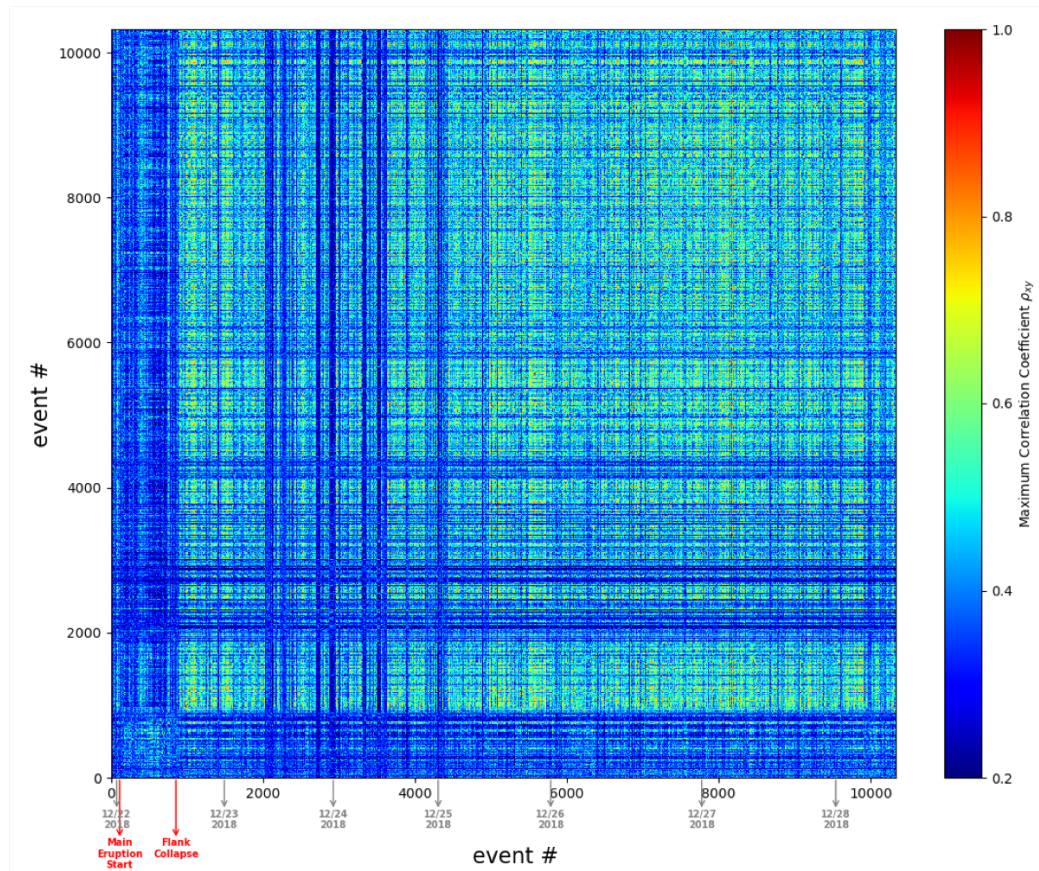


Figure 4.4: Matrix showing maximum cross correlation coefficient values between each pair of picked IS06 infrasound signal events from December 19 - 29, 2018. During the pre-collapse eruption the events did not have high correlation (i.e. were not repetitive). After the flank collapse, the events are more highly correlated with each other, possibly representing discrete Surtseyan explosions. They are well correlated throughout the remainder of the eruption and do not appear to evolve significantly over time, suggesting the process of their generation is constant.

4.1.3 Infrasound Event Clustering

We cluster the IS06 infrasound events into groups of similar signals (or “multiplets”) based on their cross-correlation values, using a clustering algorithm based on the method of Matoza and Chouet [2010]. The algorithm identifies the most correlated pair in the maximum correlation matrix and assigns it to the first multiplet. Next, any event that is correlated with the best pair above a specified cross-correlation threshold is added to the

multiplet. Events assigned to the multiplet are removed from the maximum correlation matrix until no events remain that correlate with the best pair above the threshold. The algorithm then finds the most correlated pair of the new matrix, and repeats the process to assign events to a second multiplet and so on until no events correlate with each other above the threshold. The result is a list of identified multiplets and their constituent events.

The threshold for cross-correlation was set at 0.65, to balance identifying as many waveforms belonging to a multiplet as possible, but excluding those with poor signal-to-noise ratios. In tests conducted in Green and Neuberg [2006] for a volcano-seismic dataset, in which 600 synthetic events corresponding to different families were created and then used to compute which correlation coefficients classified the events correctly, a correlation coefficient of 0.65 resulted in the highest percentage of events classified correctly before the event families began to merge. That study went on to use a coefficient of 0.70 to improve signal-to-noise ratio, though it identified slightly less events. Preliminary testing of the Anak Krakatau IS06 infrasound events suggested there were a high number of events in the 0.65-0.70 correlation range which would not be attributed to multiplets if the 0.70 value was used, so slightly higher signal-to-noise ratio was traded for a more complete event classification.

Using the cross-correlation threshold of 0.65, the algorithm generated a total of 574 multiplets which contained 8722 (84.5%) of the 10324 IS06 infrasound events. A matrix representing all 8722 events assigned to multiplets and aligned by cross correlation is presented in Figure 4.5, along with matrices for the events of two largest multiplets. Multiplet 1, presented in the upper left panel, is the largest multiplet with 1709 events. Multiplet 2 is the second largest, with 839 events, and shows the same number of peaks and troughs as Multiplet 1, but with a lower frequency. The majority of events in both of the largest multiplets occurred after the Anak Krakatau flank collapse. The

right panel shows all 8722 waveforms that were well correlated enough to be assigned to multiplets. From the beginning of the climactic phase to the flank collapse the event waveforms are less well correlated, suggesting that the infrasound was dominated by non-repetitive eruption processes related to the intense Strombolian eruption, lava flow, and ash emissions that eyewitnesses reported during this time [Global Volcanism Program, 2019]. After the flank collapse, the events appear more uniform, suggesting a transition to short, repeating explosions rather than continuous fluctuating eruption tremor.

To ensure that similar waveforms were classified together despite poor signal-to-noise ratios, the algorithm further groups the multiplets into families. For this procedure, the mean waveform (or “stack”) for each multiplet is calculated, and each multiplet stack is cross-correlated with each other stack using Equation 4.1 in the same manner used to cross-correlate individual events. Multiplets with stacks that correlated with other multiplet stacks above a cross-correlation threshold of 0.75 are merged into “families”. A higher correlation threshold was used to boost classification accuracy and achieve a similar total correlation to Green and Neuberg [2006] and Green et al. [2013] which used 0.7 for both cross-correlation into multiplets and then into families. After lists of waveforms belonging to each family were calculated, the waveforms within each family were once again cross-correlated to determine which event was most highly correlated with every other event in the family. The waveforms in the family were ordered chronologically and aligned to the most correlated event.

The families classification procedure generated 487 families, with the four largest families containing 5394 (61.8%) of the 8722 multiplet events. The four largest families with their stacked waveforms and aligned event matrices are presented in Figure 4.6. We calculate PSDs for each of the events in the family and the mean waveform of each family, and each of the events in the family are identified on a plot of event amplitude vs. time. A four families are presented in Figure 4.7. To gauge the similarity between families, the

waveforms from each family were stacked, and the stacks were cross-correlated. A cross-correlation matrix for the largest 16 event families, each containing 50 or more events, is shown on Figure 4.8. The families on this figure are ordered by number of events in each family.

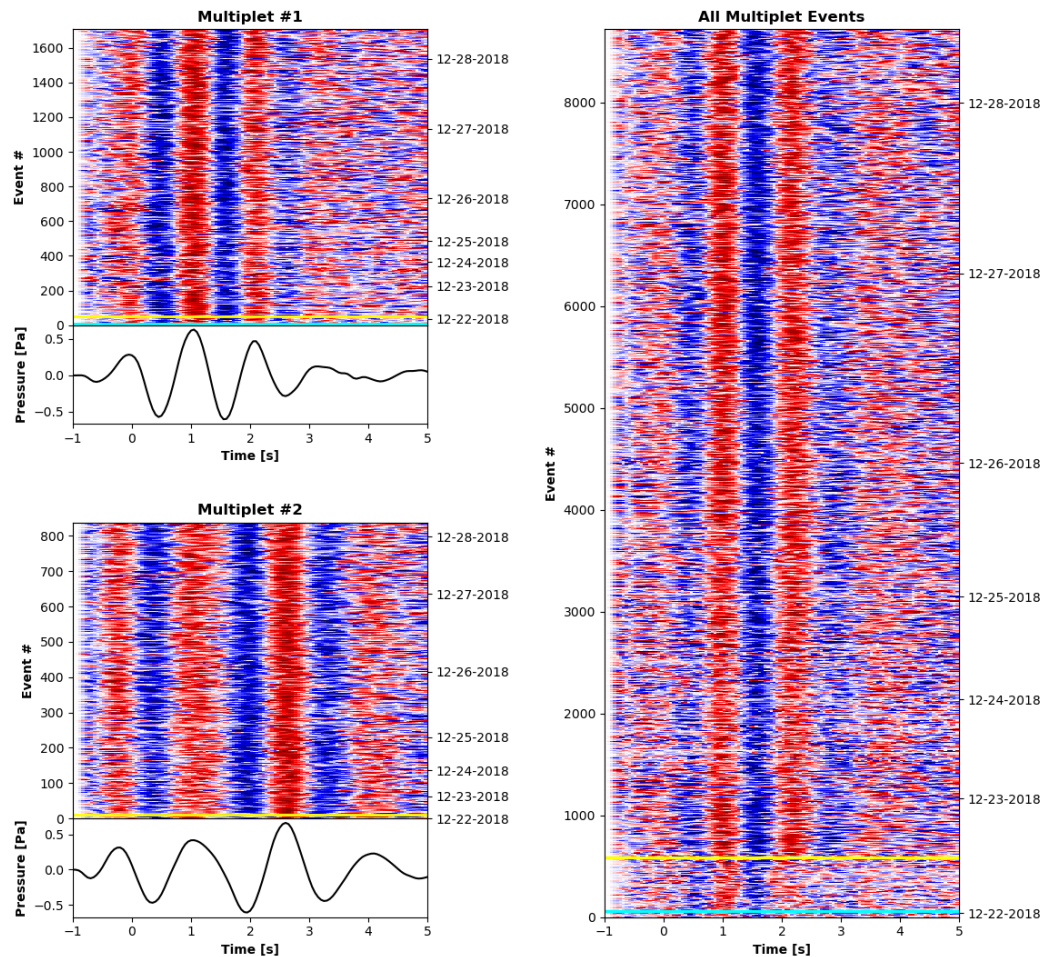


Figure 4.5: Multiplier waveforms of station IS06 infrasound signal in temporal order starting at Event 0, aligned by cross-correlation. The upper left panel shows the largest multiplier, Multiplier 1, with 1709 events, where each row of the matrix shows an event waveform with red colors indicating positive pressure and blue colors indicating negative pressure of the wave. Below the waveform matrix is the mean waveform stack for the multiplier. The lower left panel shows the second-largest multiplier, Multiplier 2, with 839 events, and its corresponding stack. The right panel shows every event that was assigned to a multiplier. The time of the beginning of the climactic phase of the eruption is indicated by a cyan horizontal line. The time of the flank collapse and tsunami is indicated by a yellow horizontal line.

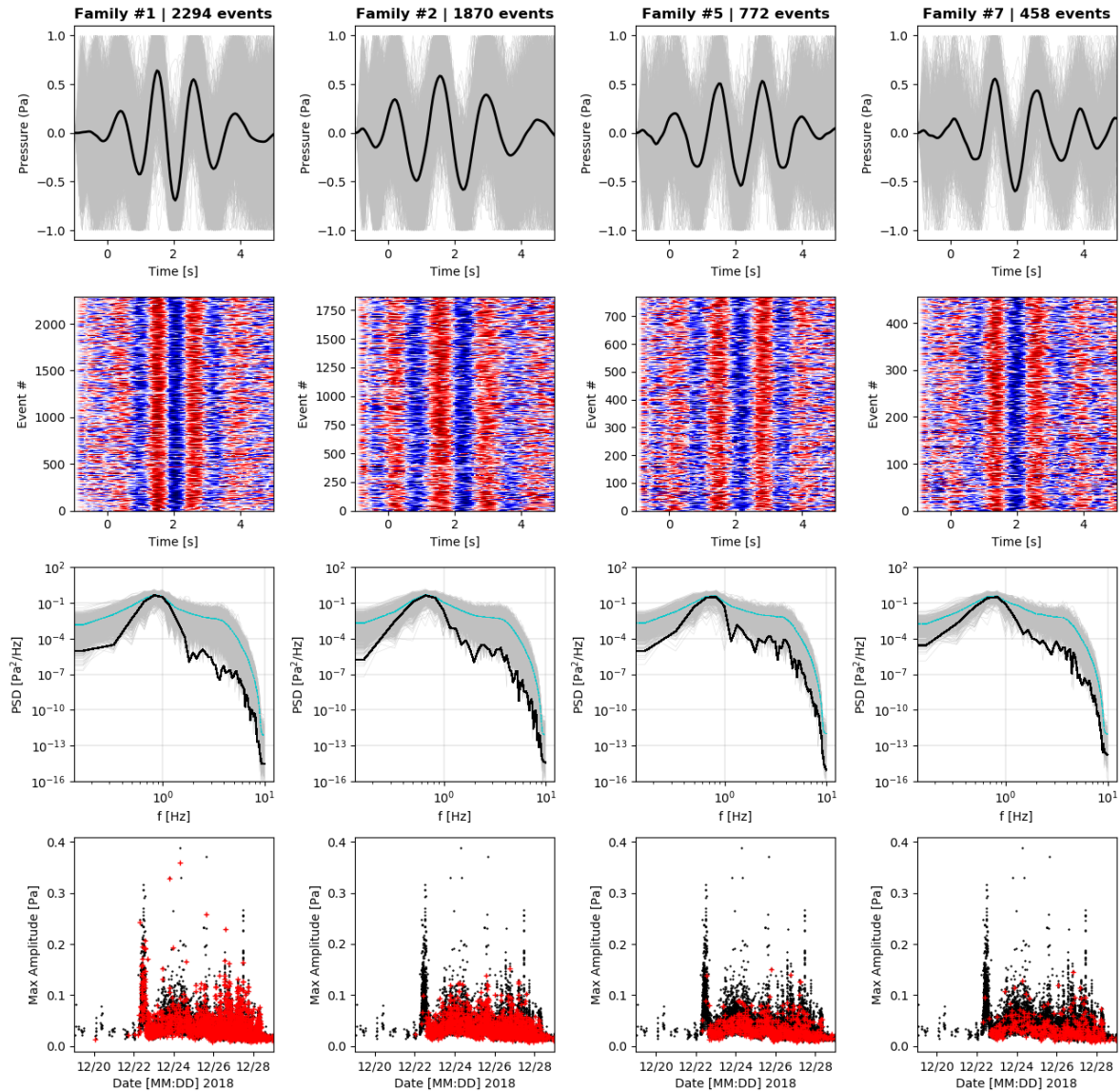


Figure 4.6: The four largest families of events identified at IS06 (infrasound). The first row of panels show individual waveforms of the family in gray, and the master waveform stack of the family as a solid black line. The second row of panels show event matrices for the families in chronological order with the first event at 0. The events are aligned via cross correlation to the best-correlated waveform in the family. The third row of panels show the PSDs for each family. Individual PSDs for each event are shown in gray, the average PSD is shown in turquoise, and the PSD of the waveform master stack is shown in black. The fourth row of panels shows every event as the maximum amplitude of the event vs the time of the event (black dots) and identifies the events assigned to the family (red dots). The master waveforms for each family appear qualitatively similar, but have variable frequency content.

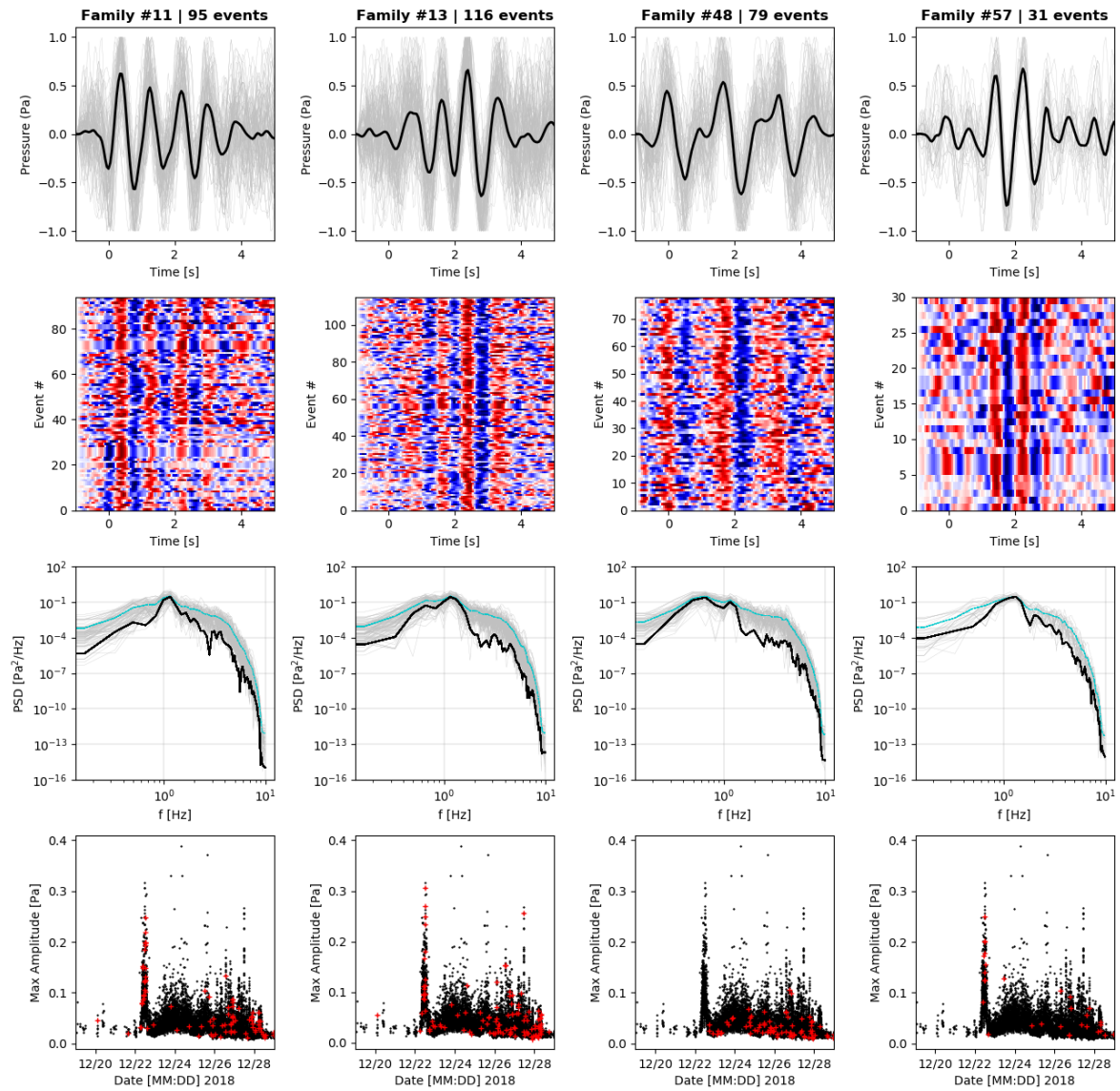


Figure 4.7: As Figure 4.6, but for four smaller waveform families of IS06 infrasound that appear qualitatively different than the four largest families. The master waveform stacks appear qualitatively unique from one another, with clearly different frequency content.

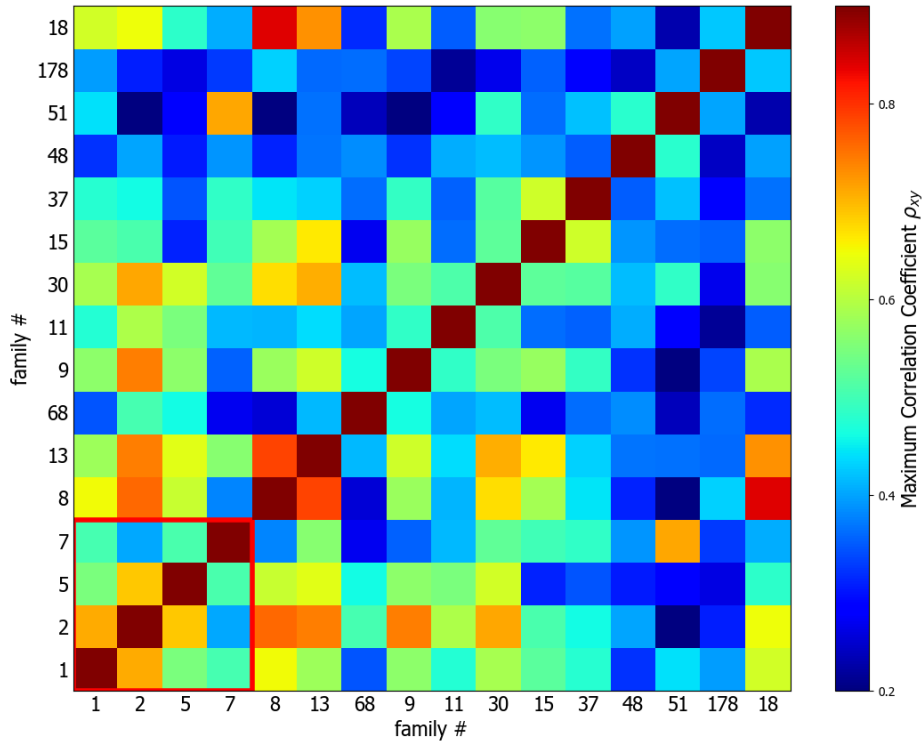


Figure 4.8: Cross-correlation matrix for the 16 IS06 infrasound event families that contain 50 or more events, ordered by number of events in each family from most events (Family 1; 2294 events) to least events (Family 18; 56 events). The four largest waveform families from Figure 4.6 are outlined in red. Colors represent the maximum value for the correlation coefficient ρ_{xy} for each pair of family mean waveforms.

4.1.4 Discussion

The mean waveforms of the largest four event families have qualitatively similar shapes, but small differences in frequency content are visible. Family 1 and Family 2, for example, show a similar pattern of waveform peaks and troughs but their corresponding power spectral density plots show that Family 1 has an overall higher frequency. Families 5 and 7 have similar waveform shapes to the two largest families, but also vary in frequency and relative amplitude of the peaks and troughs. Figure 4.8 reveals the similarity between the four largest families, with Family 1 and 2 being most correlated, followed by Family 2 and Family 5, indicating that events in these families are related. Families

1,2, and 5 are also well correlated with smaller families such as Families 8, 9, and 13, suggesting a larger relationship between some families exists.

Due to their short and repetitive nature, events in the larger families likely represent repeated explosions from Anak Krakatau, consistent with reports of intense Strombolian activity at the volcano during this timeframe. Family 1 events are notably present during the pre-collapse intense Strombolian activity and after the flank collapse (Figure 4.6, bottom left), while Family 2 events mostly occur after the flank collapse and tsunami. This may indicate a variation in the source mechanism of the explosions, such as Family 1 representing subaerial Strombolian explosions and Family 2 caused by magma coming into contact with water, generating small phreatomagmatic explosions. This is in agreement with the study of a shallowly submerged vent at Bogoslof volcano by Lyons et al. [2020], which found that the most significant effect of seawater submerging the vent which had previously been subaerial was a decrease in frequency content of the infrasound produced. However, the long-range (1,156 km) propagation path of the infrasound signals from source to receiver makes using the waveforms to determine exact source processes challenging. Most long-range infrasound will have traveled through the stratosphere or thermosphere, and heterogeneities in temperature, wind speeds, and wind direction in these layers results in multi-pathing and scattering of the acoustic waves along the propagation path [Kulichkov, 2004]. Thus, the apparent differences in waveform shape and frequency between well-correlated waveform families such as Family 1 and Family 2 could simply be due to variations in the atmospheric propagation path. Hydroacoustic waveforms are more stable over long range, and may assist in determining eruption source processes more reliably.

4.2 Hydroacoustic Waveform Similarity

4.2.1 Hydroacoustic Event Selection

We investigate hydroacoustic event similarity to determine whether repetitive signals could be identified and interpreted for information on submarine eruption source processes at Anak Krakatau. Twelve days of hydroacoustic data from November 29 to December 11, 2018 hydroacoustic swarm was beamformed and filtered with a 1-4 Hz Butterworth bandpass filter. This filter was chosen as a result of PSD analysis (Figure 4.9), to balance between analyzing the frequency band with the highest signal power ($\sim 1-11$ Hz) and the fact that higher frequency waveforms will be more affected by noise and invariably have lower correlation. During initial analysis, the same procedure implemented to select IS06 infrasound events was used to automatically pick H08S hydroacoustic events. However, the STA/LTA picking was not effective in discerning a substantial number of hydroacoustic events that were flagged by PMCC array processing, probably due to its lower signal to noise ratio. Therefore, events were picked manually from the filtered and beamformed signal, and picks were only made where there were concurrent PMCC detections indicating the signal was within ± 3 degrees of the Anak Krakatau back-azimuth. There were 2169 event picks made over the 12 day swarm signal duration. The events were windowed from 1 second prior to the event pick time to 5 seconds after the picked event time. The events are plotted by maximum amplitude on Figure 4.10 and compared to PMCC detections and satellite images from the same timespan. A thermal satellite image shows incandescence in the crater on November 29, but visual or thermal imagery was not available after that day due to cloud cover so the other three satellite images shown are Sentinel-1 SAR images. The SAR images show the volcanic cone and surrounding islands, but do not show whether ash plumes or explosions were occurring.

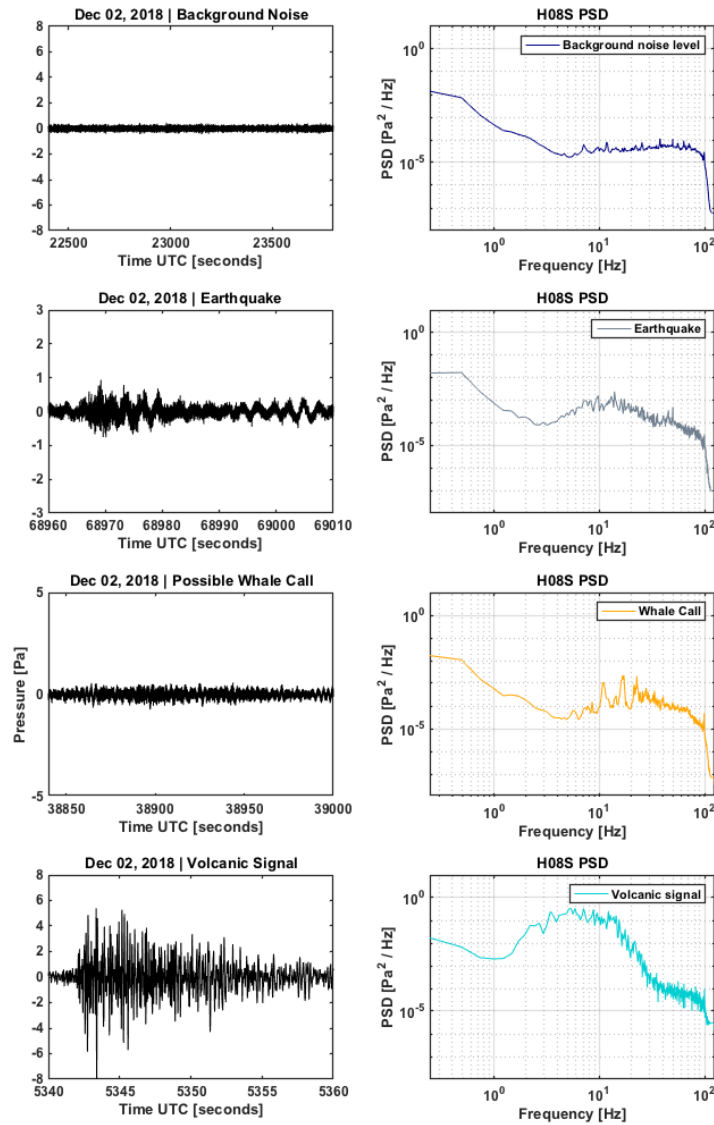


Figure 4.9: Waveforms and power spectral densities for a variety of H08S hydroacoustic signals observed on December 2, 2018. The first set of panels show background noise from a stretch of time where no volcanic signals were detected by PMCC. The second set of panels shows the waveform and PSD trace of what was likely a tectonic earthquake caused by subduction in the Java trench, and was not associated with PMCC detections from the direction of Anak Krakatau. The third set of panels shows an example of a whale call, indicated by the three main harmonics on the PSD, again not associated with PMCC detections. The last set of panels shows a hydroacoustic signal identified by PMCC during the hydroacoustic swarm, with its corresponding PSD showing that the majority of the signal is contained in the 1-11 Hz range.

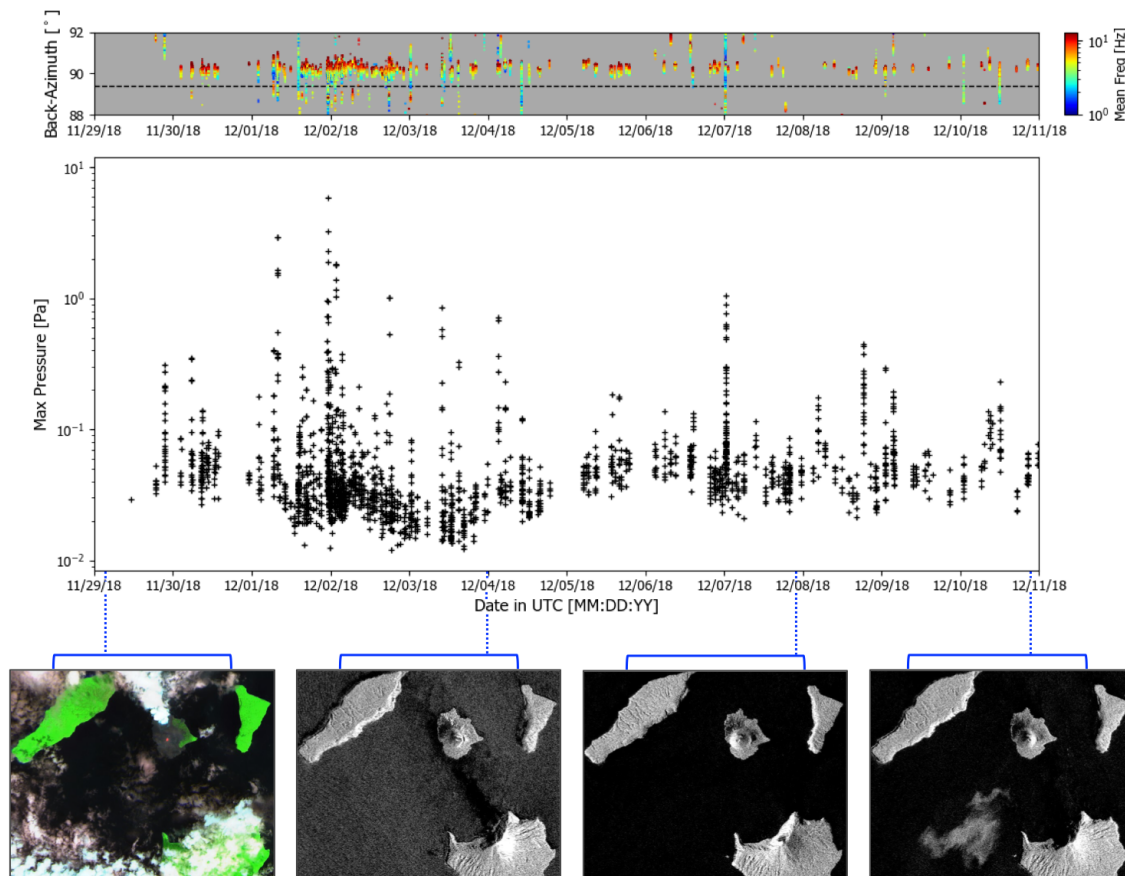


Figure 4.10: Summary of H08S hydroacoustic swarm events from November 29 - December 11, 2018. Top panel: PMCC families detections, with colors representing mean frequency of the detection in log scale. The black dashed line is the back-azimuth of Anak Krakatau, 84.9° . Middle panel: the 2169 manually picked hydroacoustic events (with PMCC cross-checking), plotted by maximum amplitude of the signal. During this timeframe, seismic events and ash plumes were recorded on December 1-3 and December 7-9, 2018 [Global Volcanism Program, 2018b,c]. The row of panels below show Sentinel satellite imagery, the first panel showing a thermal anomaly in the crater on November 29, 2018 from the Sentinel-2 L1C SWIR band, and the right three panels showing Sentinel-1 SAR GRD satellite imagery [Modified Copernicus Sentinel Data, 2019].

4.2.2 Hydroacoustic Event Cross-Correlation

Using the same procedure as with the IS06 infrasound data, we cross-correlate hydroacoustic events to determine event waveform similarity. Each event waveform is normalized and cross-correlated with each of the other normalized events, and the calculated

correlation coefficients used to construct a cross-correlation matrix (Figure 4.11). Though the maximum correlation values for the event pairs are generally lower than those of the infrasound signals, many pairs exceed a 0.6 correlation value. Overall the events appear less repetitive than the IS06 infrasound events, which may be due to a lower signal to noise ratio or simply greater signal variability.

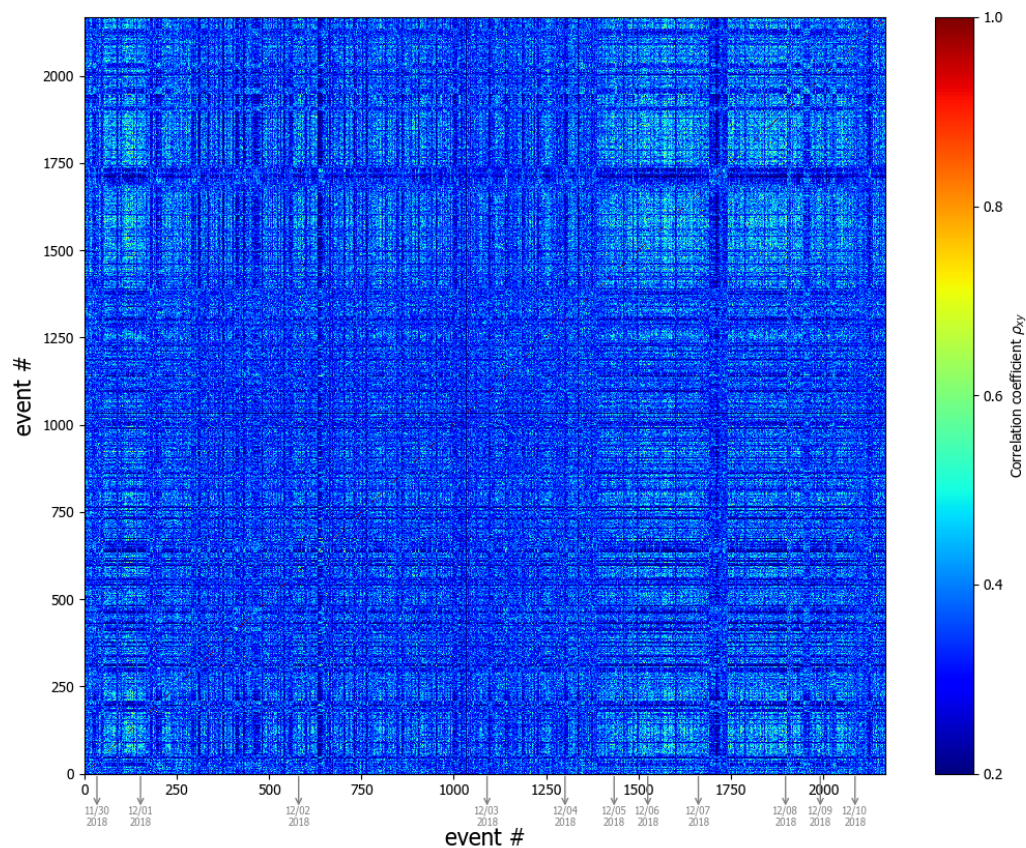


Figure 4.11: Matrix showing maximum cross-correlation values between each pair of H08S hydroacoustic signal events from November 29 through December 10, 2018.

4.2.3 Hydroacoustic Event Clustering

We group the hydroacoustic signals into multiplets based on their cross-correlation values in the same manner described for the IS06 infrasound events in section 4.1.3.

The threshold for cross-correlation was set to 0.6, as the signal-to-noise ratio for the hydroacoustic signal was lower than the infrasound signal and there were a large number of events in the 0.6-0.65 range that would have been excluded by using the infrasound threshold value of 0.65. The threshold value of 0.6 is considered the acceptable limit, as below this value events may begin to converge. Using this method, 261 multiplets are identified which contained 67.7% of the picked events. A matrix showing each of the events aligned by cross-correlation is presented on Figure 4.12, along with matrices containing waveform data for the two largest multiplets.

The number of events assigned to each multiplet was comparatively fewer than the infrasound multiplets, which was expected due to the lower correlation values. Multiplets were further grouped into families to show more broadly which multiplets were similar to each other, and to reduce the effect of the lower signal-to-noise ratio of the hydroacoustic events. Multiplets with stacks correlating with other multiplet stacks above a threshold of 0.6 were assigned into families. The events in each family were again cross-correlated to determine which event was most similar to the most other events, and the waveforms were ordered temporally and aligned to the most correlated event in the family. The families classification procedure yielded 153 families. The four largest families and their mean waveforms with aligned event waveform matrices are presented in Figure 4.13. PSDs were calculated for the families, and the events in each family are plotted against all picked events to show their timing. A second group of families are shown in Figure 4.14 to show some of the waveform variability among the hydroacoustic families.

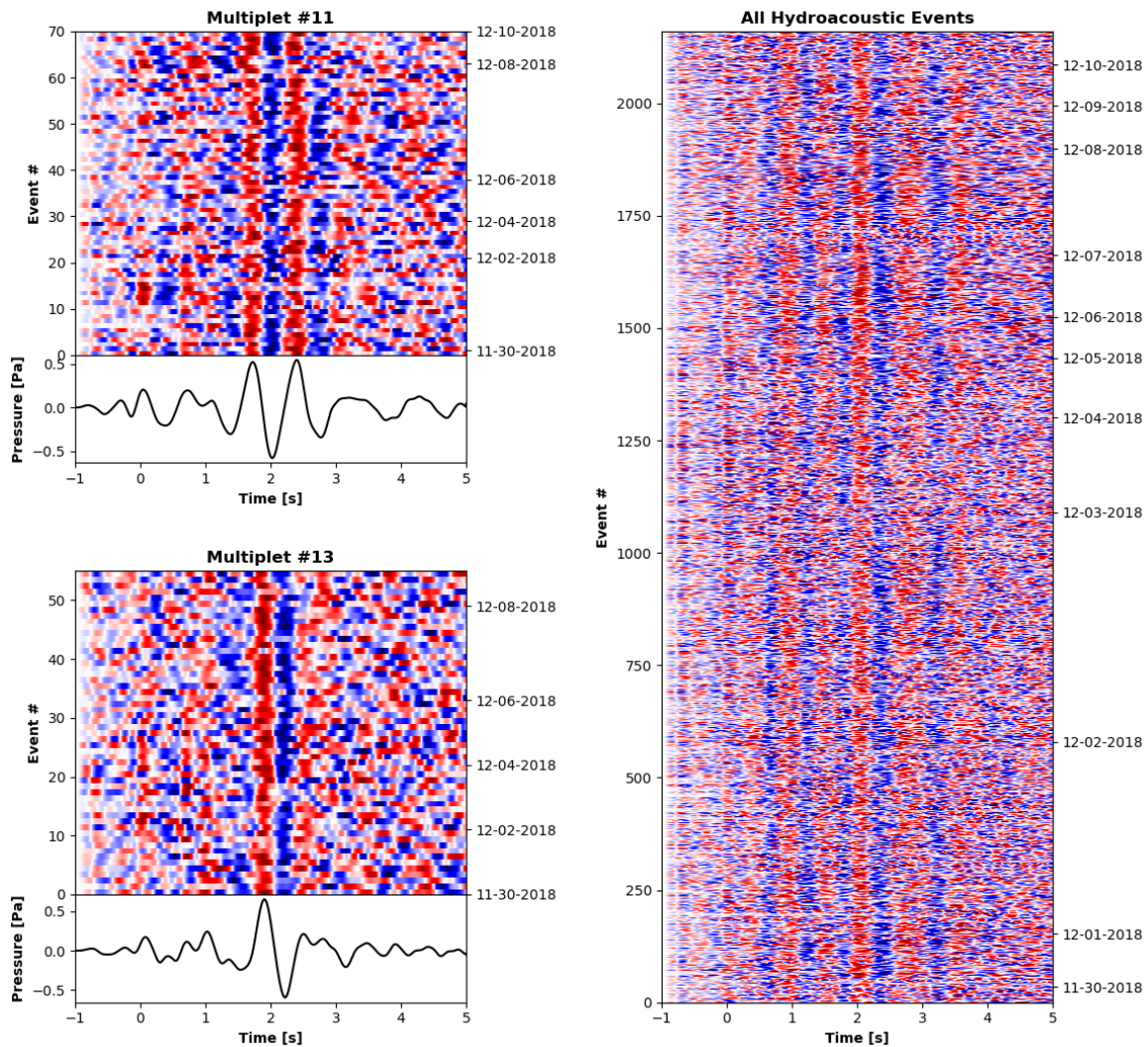


Figure 4.12: Right panel: all 2169 hydroacoustic event waveforms in temporal order starting at Event 0, aligned by cross correlation. Each row of the matrix represents an event waveform, with red colors indicating positive pressure and blue colors indicating negative pressure of the signal. Top left panel: event matrix for the largest multiplet, Multiplet 11, with 71 events, and its corresponding mean waveform stack. Bottom left panel: event matrix for the second largest multiplet, Multiplet 13, with 56 events, and its corresponding mean waveform stack.

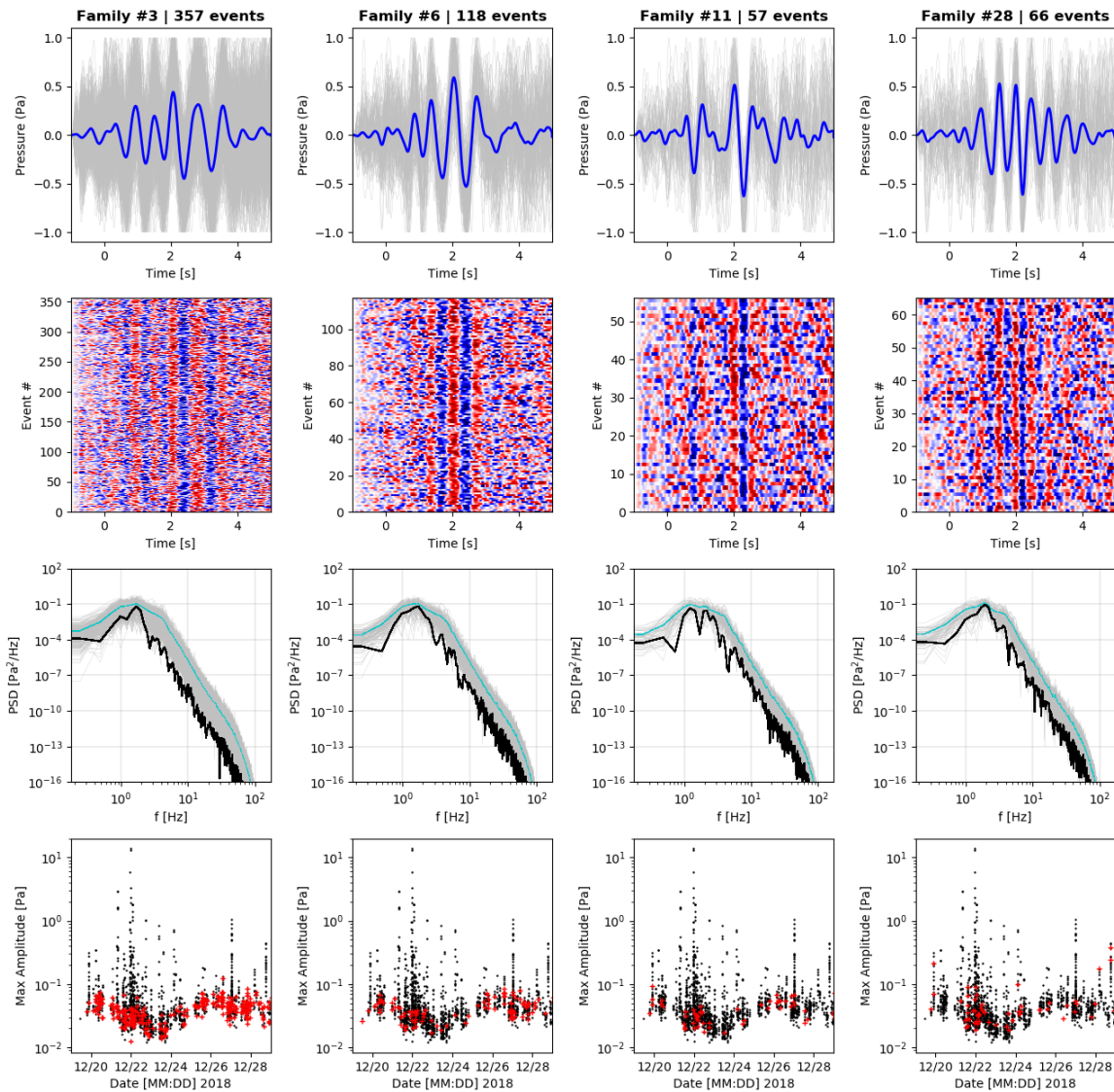


Figure 4.13: The four largest families of hydroacoustic events picked from station H08S hydroacoustic data. The first row of panels show individual waveforms of the family in gray, and the master waveform stack of the family in solid blue. The second row of panels show event matrices for the families in temporal order, aligned by cross-correlation to the best-correlated waveform in the family. The third row of panels show the PSDs for each family, with the individual PSDs for each event in gray, the average PSD shown in turquoise, and the PSD of the mean family stack in black. The fourth row of panels shows the plot of all events, where events are plotted by their maximum amplitude vs. time, and identifies events assigned to the family in red.

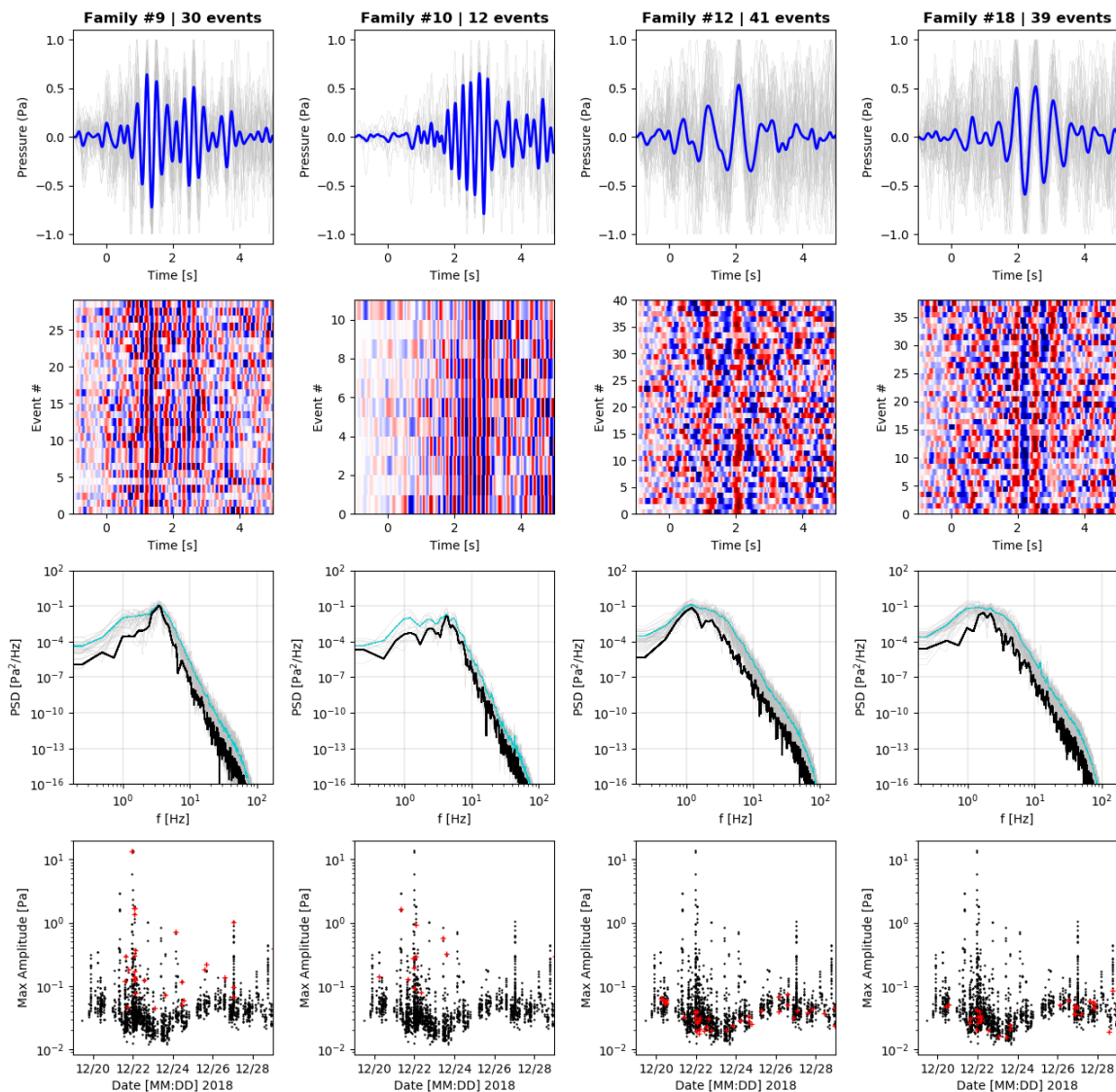


Figure 4.14: As Figure 4.13, but additional families of hydroacoustic events picked from station H0SS hydroacoustic data, which show the waveform variability between families.

The largest waveform family, Family 3, has a frequency peak at 2 Hz with events of ~ 4 s in duration. The second largest family, Family 6, also has a frequency peak at about 2 Hz but a shorter duration of ~ 2.5 s. Each of the four largest families consist predominantly of events with lower maximum amplitude, and do not include many of the high-amplitude events (Figure 4.6). In contrast, two of the smaller families, depicted

on Figure 4.7, consist mostly of the high-amplitude events. These families, Family 9 and Family 10, have peak frequencies of ~ 3 Hz and ~ 4 Hz, respectively. Family 9 displays an initial pulse, followed by two smaller amplitude pulses, which is likely a propagation signature rather than a source feature given the remote source-receiver distance.

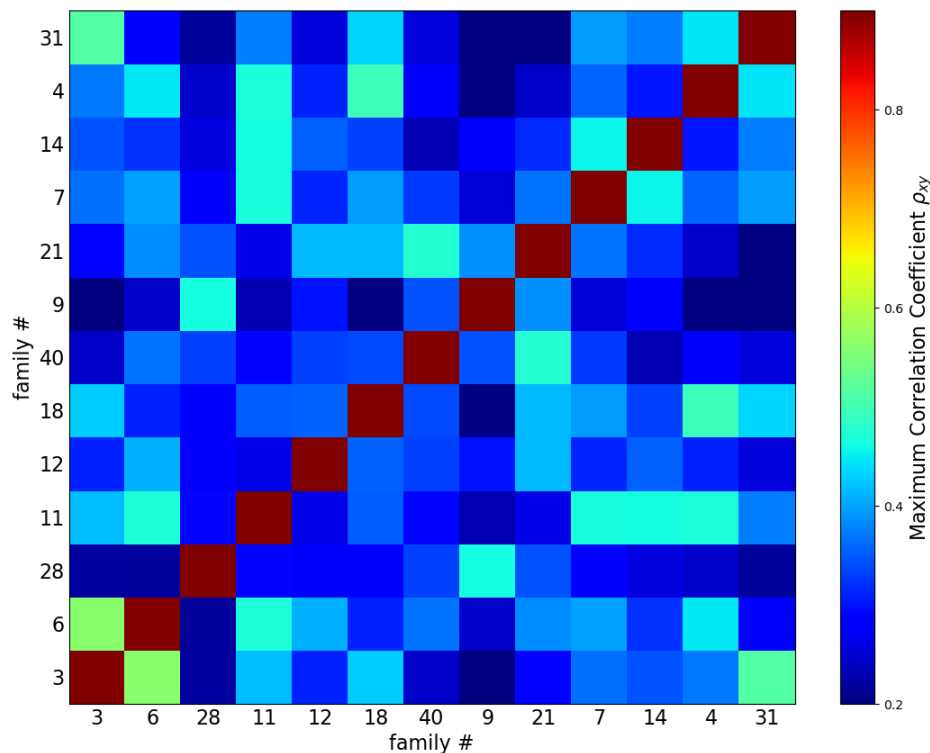


Figure 4.15: Cross-correlation matrix for the 13 hydroacoustic event family mean waveform stacks that contain 20 or more events, ordered by number of events in each family from most events (Family 3; 357 events) to least events (Family 31; 22 events). Colors represent the maximum value for the correlation coefficient ρ_{xy} for each pair of family stacks.

To assess whether any of the hydroacoustic families are closely related, we again cross-correlate the mean waveform stacks for each family and the maximum cross correlation between each pair of family stacks is used to create a cross-correlation matrix for the largest 13 families (Figure 4.15). Each family contains 20 or more events, and most of the families are shown not to be well correlated. The highest correlation between these

13 largest families is between Family 3 and Family 6, which have a maximum correlation coefficient of 0.56. This suggests that the waveforms are appropriately grouped into families depending on their similarity, and similarity between families is not high.

4.2.4 Hydroacoustic Envelopes

Since many of the high-amplitude hydroacoustic events exhibited a longer duration than the 6-second cross-correlation time-window, we conduct hydroacoustic signal envelope analysis to determine similarity of the longer signals. This analysis is based on a method used by [Talandier and Okal, 2001], which used hydroacoustic T-phase signal envelopes to distinguish between subduction zone earthquakes, volcanic earthquakes, and explosive submarine events (Figure 4.16). The hydroacoustic signal was first filtered from 1-15 Hz to capture the most signal from the volcano, and then beamformed to improve the signal-to-noise ratio. Eight high amplitude events which corresponded to consistent PMCC detections from the back-azimuth of Anak Krakatau, as well as eight high-amplitude events without corresponding PMCC detections, were picked manually on days 335 and 336 (December 1-2, 2018) of the eruption. The envelope for each 120 s signal was calculated using the ObsPy filter envelope function [Beyreuther et al., 2010], which adds the squared amplitudes of the function and its Hilbert transform and computes the square root. The 5-second rolling mean of each envelope was then calculated to smooth the envelope and remove rapid fluctuations, which was chosen based on trial and error. The normalized, smoothed envelopes for the 2 days of manually picked signals are presented on Figure 4.17. The volcanic signal envelopes are all approximately 20 s in duration with a sharp onset, with a few exhibiting a notch at the peak of the envelope. The signal envelopes that did not correspond to PMCC detections resemble the subduction-zone earthquake envelope in Figure 4.16, so are possibly attributable to

T-phases from subduction zone earthquakes in the Indian Ocean basin. Indeed, there is a band of low-frequency PMCC detections in the 45° - 100° range, which align with the back-azimuth position of the Java Trench. This indicates that seismic energy from subduction zone earthquakes along the Java Trench is able to couple into the water column and propagate as hydroacoustic waves to station H08S.

Talandier and Okal [2001] attributed the frequencies and envelope shapes of each type of event to its source process characteristics. The low frequencies and long durations of subduction zone earthquakes were ascribed to the hypocenter of the earthquakes being kilometers below the ocean floor, resulting in a long propagation path before conversion to T-waves in the water column. The solid-earth propagation path would likely also produce multi-pathing, resulting in a longer event waveform. Additionally, larger subduction zone earthquakes can release energy for many seconds, which would further increase the duration of the T-phases. In contrast, volcanically-triggered earthquakes are typically small magnitude, near-surface events with shorter solid-earth seismic paths which can retain their higher frequency content and produce a more broadband spectrum. The steep slopes of many volcanoes also offer efficient transmission of seismic energy into the water column, which may produce more impulsive events with shorter duration. Volcanogenic explosions, on the other hand, generally occur at the magma-water interface and directly release acoustic energy into the water column. The resultant T-waves are often of short duration, and the lack of a solid-earth propagation path means they will often retain their high frequencies (although some volcanoes can produce explosions with band-limited spectra) [Talandier and Okal, 2001].

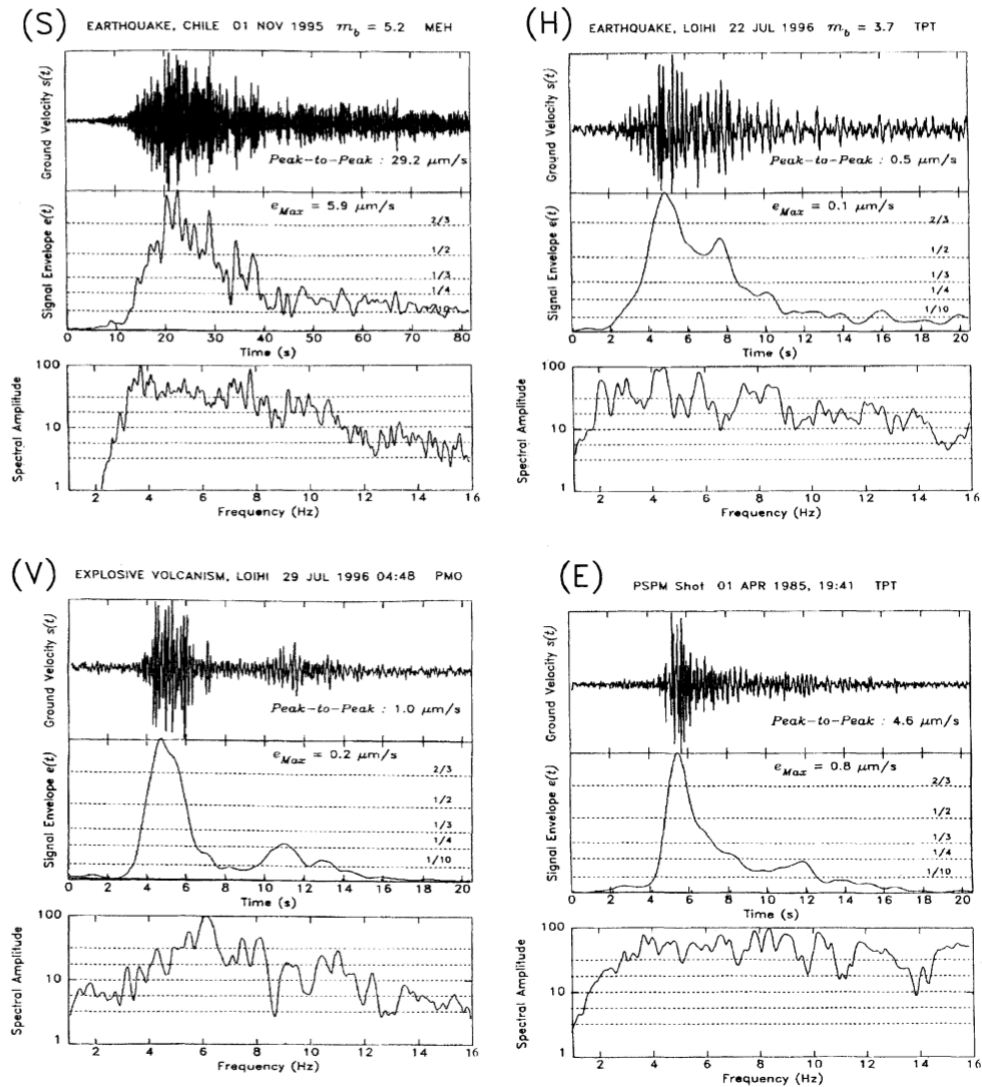


Figure 4.16: Figure reproduced from Talandier and Okal [2001], showing selected waveforms, signal envelopes, and spectral amplitudes of four T-phase signals detected at seismic stations of the Polynesian Seismic Network. The waveforms have a sampling rate of 0.02 s, and were high-pass filtered above 2 Hz. The envelopes were smoothed using a 1-second rolling average, with the 1-second window chosen based on trial and error. To calculate spectral amplitudes, the signal was band-pass filtered from 1-16 Hz due to limitations of the seismic sensors.

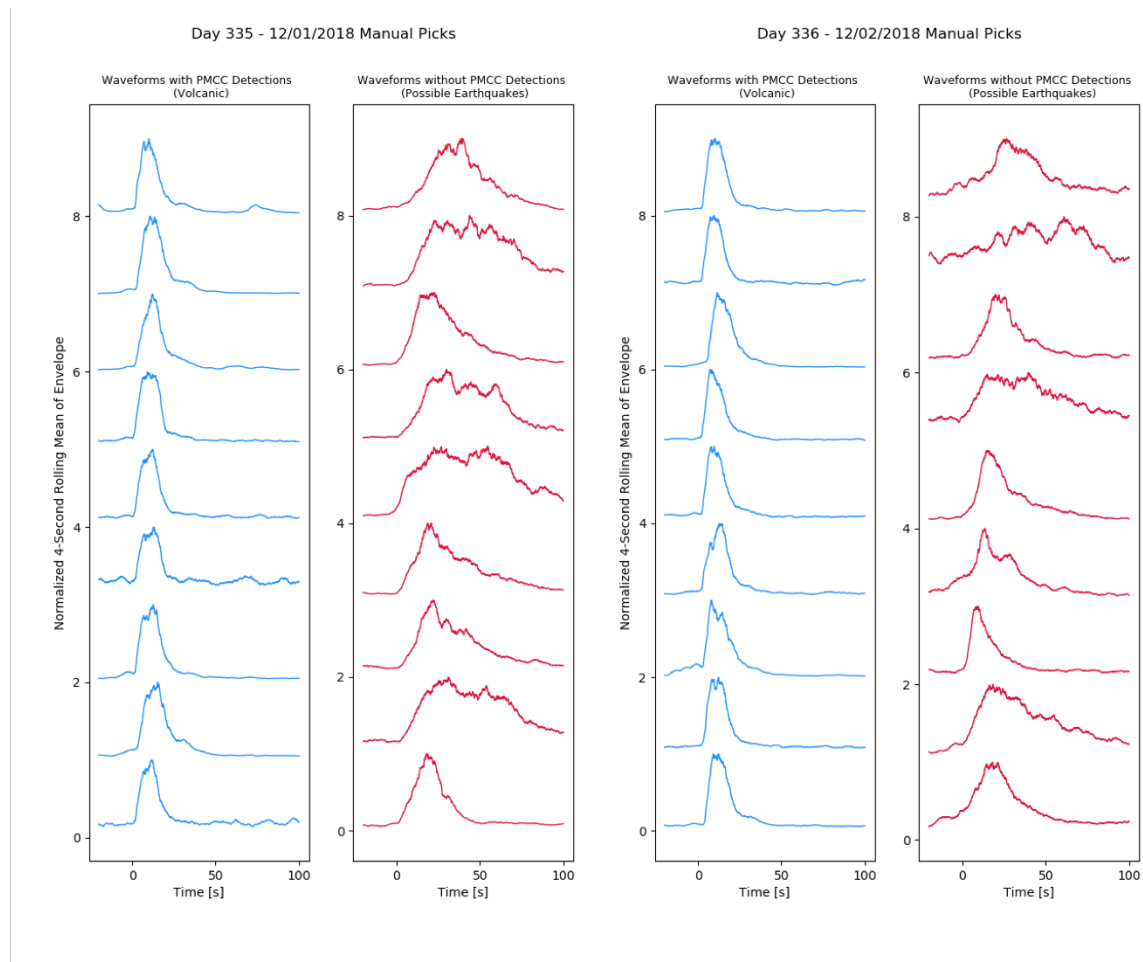


Figure 4.17: Hydroacoustic signal envelopes for manually-picked 120 second sections of signal from sensor H08S2, the sensor with the highest signal-to-noise ratio for the Anak Krakatau hydroacoustic swarm signals. The first two panels are manually selected events from day 335 (December 1, 2018), and the last two panels are manually selected events from day 336 (December 2, 2018). Envelopes colored blue were calculated from events with concurrent PMCC detections from the Anak Krakatau back-azimuth, which we attribute to submarine volcanic activity. Envelopes colored red are from events which had no PMCC detections from the Anak Krakatau direction, which were possibly generated by subduction-zone earthquakes along the Java trench.

4.2.5 Discussion

Due to the challenges of data collection and visual observation in a submarine environment, many questions remain regarding source mechanisms and conditions of submarine explosive volcanism. Therefore, the discussion presented here is speculative and repre-

sents one set of possible interpretations of eruption events at the volcano. Several factors must be considered when investigating the physical source mechanisms which produced the recorded hydroacoustic signal, which include the frequency, duration, continuity, recurrence interval, waveform similarity, and visual observations at the ocean surface. Firstly, the static back-azimuth of these events over 12 days (established by PMCC results) is typical of a volcanic source, and rules out many possible sources of transitory hydroacoustic signal (animal sources, ships, storms, etc.). The minutes-to-hours long interval of quiescence between successive events and lack of perfectly repeating waveforms further rules out seismic surveying as the source. A timeline of the eruption and summary of the PMCC detections, picked events, satellite imagery, and available detections of seismic activity, thermal anomalies, eruption plumes, lava flows, and surtseyan activity is presented on Figure 4.18. Seismicity from the volcano was detected throughout the eruption by PVMBG, and seismic events were reported on most days with infrasound or hydroacoustic signal from Anak Krakatau. There was a thermal anomaly present at the crater for the majority of the eruption, though the satellite imagery was mostly obscured by cloudy weather from December 2018 to early January 2019. The lava flows reported from August to October, 2018 were not accompanied by major infrasound activity, suggesting activity may have been more effusive than explosive. Ash plumes were intermittent, and mostly correspond to periods of seismic or thermal activity. The reported Surtseyan activity reported by Global Volcanism Program [2019] from after the flank collapse on December 22, 2018 to January 9, 2019 overlaps well with the infrasound detections from IS06 and IS52 suggesting this activity was a major source of infrasound, though no continuous hydroacoustic detections were observed at that time.

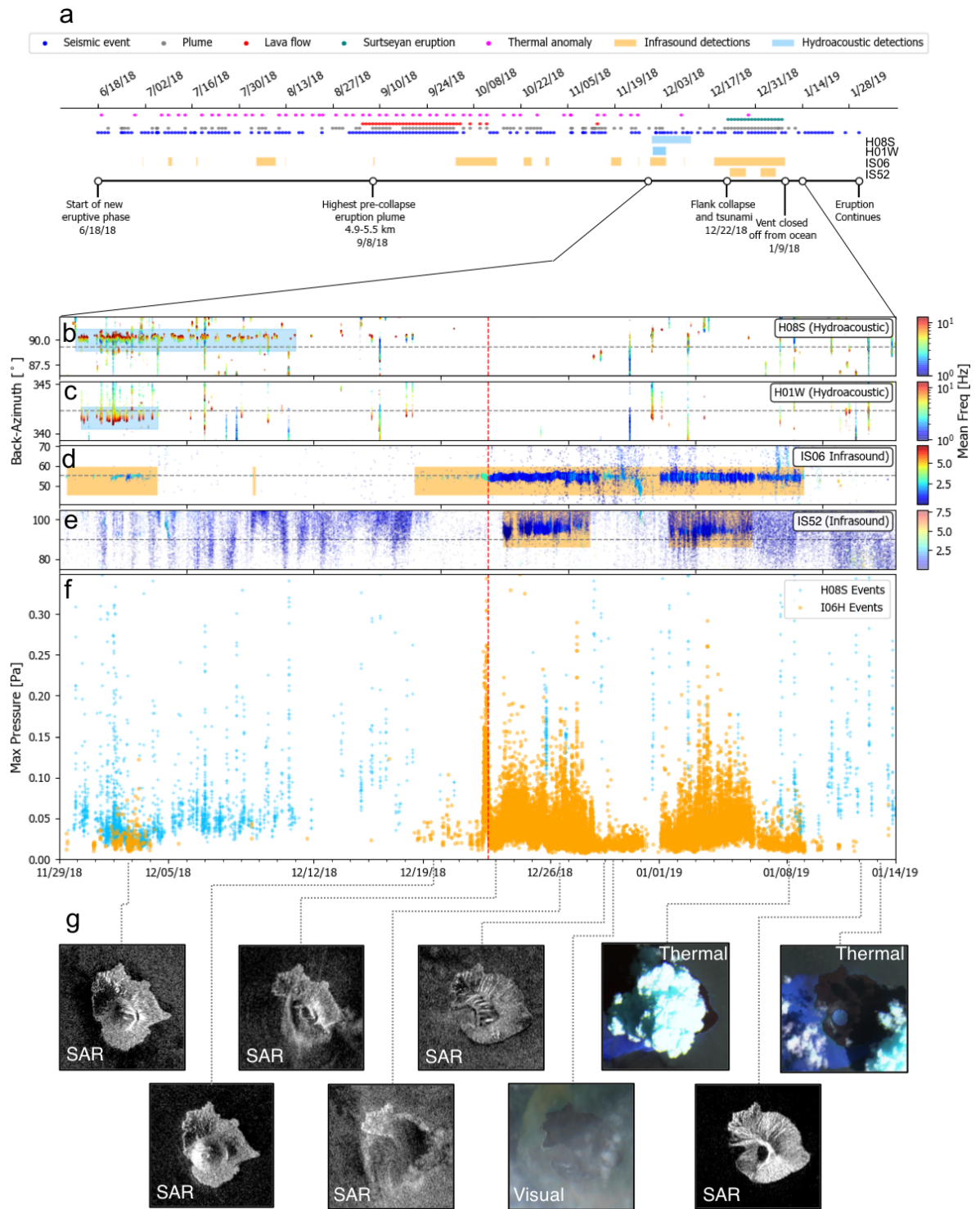


Figure 4.18: (a) Timeline of eruption. Magenta circles indicate days where Sentinel-2 satellite detected a thermal anomaly [Modified Copernicus Sentinel Data, 2019], teal circles indicate reported Surtseyan eruption [Global Volcanism Program, 2019], red circles indicate days where lava flows were reported [Global Volcanism Program, 2019], gray circles indicate days with eruption plumes reported [Global Volcanism Program, 2019], and blue circles indicate days on which volcanic seismic events or eruption tremor at Anak Krakatau were reported by PVMBG [Pusat Vulkanologi dan Mitigasi Bencana Geologi, 2018]. Blue rectangles show the duration of hydroacoustic PMCC detections from H08S and H01W, and orange rectangles show duration of infrasound detections from IS06 and IS52. (b,c) PMCC hydroacoustic families detections. (d,e) PMCC infrasound bulletin detections. Horizontal dashed black line on panels (b-e) indicates back-azimuth direction of Anak Krakatau, and vertical red dashed lines indicate the approximate time of the flank collapse which triggered the tsunami. (f) Infrasound (IS06) and hydroacoustic (H08S) events. Infrasound events were picked using network STA/LTA with PMCC cross-checking method, while hydroacoustic events were picked manually corresponding to PMCC detections. (g) SAR satellite imagery from Sentinel-1 and thermal and visual satellite imagery from Sentinel-2 showing the effects of the eruption on the morphology of the volcanic edifice [Modified Copernicus Sentinel Data, 2019].

Reports of events recorded by seismic, infrasound, and hydroacoustic sensors at other submarine or partially submerged volcanoes typically divide eruption signals into two categories: impulsive events, and sustained events. Impulsive events have been attributed to in-water phreatomagmatic explosions produced by the opening of a vent (e.g., Bohnenstiehl et al. [2012], Tepp et al. [2019a]), phreatomagmatic explosions as a result of dome building and collapse (e.g., Green et al. [2013]), small to large diameter magmatic gas bubbles bursting (comparable to terrestrial Strombolian explosions; e.g., Chadwick et al. [2008], Dziak et al. [2015], Lyons et al. [2020]), or discrete, shallow volcanic earthquakes coupled into the water column (e.g., Dziak and Fox [1999], Tepp et al. [2019b]). More continuous, sustained eruptive events have been interpreted as tremor from degassing [Dziak et al., 2015]), eruption tremor from continuous phreatomagmatic explosions [Bohnenstiehl et al., 2012; Tepp et al., 2019a], sustained jetting of material at an underwater dome or vent [Lyons et al., 2020], or harmonic tremor of magma oscillating in a near-surface chamber [Dziak and Fox, 2002b].

The hydroacoustic swarm events from Anak Krakatau are typically confined to the 1-

40 Hz frequency range (with the highest energy in the 1-12 Hz range), and less than 30 s in duration, with minutes to hours between events. The waveform similarity analysis in Section 4.2.3 indicate that the 6 s hydroacoustic event waveforms are less well correlated than the later explosive infrasound events from the main eruption at Anak Krakatau, which may be due to the longer signal propagation path, typically longer event duration, higher frequencies of the hydroacoustic signal or a more variable range of source mechanisms. However, there are several families which have dozens to hundreds of events with good waveform similarity, suggesting one or more repetitive source processes. The fact that the largest 13 families are not particularly well correlated to each other implies that more than one source process is producing the events (i.e., that the signal could be originating from a mix of sources such as shallow volcanic earthquakes and water-magma interface explosions, rather than a single source). The hydroacoustic envelope comparison in Figure 4.17 indicates that the ~ 20 s duration signals are highly similar, and thus are probably being generated by a single source. These envelopes have similar sharp onsets and overall shapes to the volcanic earthquake and explosive volcanism envelopes in Figure 4.16, but the Talandier and Okal [2001] envelopes are of shorter duration. In any case, they have a clearly different shape than the example of a subduction zone earthquake, which has a more emergent onset and long tail.

There is no evidence of harmonic tremor in the H08S hydroacoustic swarm signal. Since most of the events are <30 s in duration, we classify them as impulsive signals. Due to their generally 1-40 Hz band-limited character, we cannot immediately classify them as phreatomagmatic explosions, which typically display a broadband spectrum. However, there is the possibility that high-frequencies may have attenuated during the path from source to receiver. This has been shown to occur at long-distance hydroacoustic sources such as Metz et al. [2016], where the hydroacoustic arrivals from phreatomagmatic explosions arrived at a hydrophone $\sim 15,800$ km away with frequencies of predominantly

2-20 Hz. Modeling would be required to determine whether the comparably shorter path from Anak Krakatau to H08S (3,307 km) would have resulted in a similarly significant loss of high frequencies. If the events are from phreatomagmatic explosions, they could arise from a scenario similar to the periodic dome-building and collapse at South Sarigan volcano in 2010 (proposed in Green et al. [2013]). This scenario, however, as well as a scenario in which the impulsive events are caused by fragmentation explosions is not explicitly supported by visual observations. To our knowledge, no reports of seawater discoloration (which is a typical feature of a shallow explosive submarine eruption) around Krakatau were made prior to the December 22, 2018 flank collapse. However, such reports would have to have come from eyewitnesses around the volcano, as Sentinel-2 visual-band and thermal satellite imagery is obscured due to clouds and ash plumes during the entire duration of the November 29 - December 10, 2018 hydroacoustic signal period, so we cannot identify such discoloration after the fact.

Another plausible interpretation may be that the impulsive signals are caused by the bursting of magmatic gas bubbles at the opening of a conduit on the flank of Anak Krakatau, similar to that observed at NW Rota-1 volcano [Chadwick et al., 2008], West Mata volcano [Dziak et al., 2015], and Bogoslof volcano [Lyons et al., 2020]. In-situ hydrophone recordings and coincident remotely operated vehicle (ROV) video at West Mata (vent located ~ 1200 m beneath sea surface) show 50-100 cm radius, short-duration magmatic gas bubble bursts with signal frequencies of 1-40 Hz [Dziak et al., 2015]. At 550-560 m deep NW Rota-1, ~ 10 -30 cm magmatic gas bubble bursts were also recorded by portable hydrophone and ROV with durations of 21 to 656 seconds, with the highest signal amplitudes between 10-50 Hz in frequency. Lyons et al. [2020] reported infrasound signals from extremely large magmatic gas bubble bursts at the shallowly submerged vent of Bogoslof volcano, with diameters of 100-440 m. The signal was converted from hydroacoustic to infrasound at the ocean-atmosphere interface, resulting in the loss of

higher frequencies, with the resulting signals having frequencies of 0.1-1 Hz with durations generally <4 minutes. However, although the signal frequency ranges of these case studies somewhat agrees with the frequency ranges at Anak Krakatau, the magmatic gas bubble bursts are reported to have somewhat longer durations on average, and shorter quiescent intervals.

A final possibility for the source of the hydroacoustic impulsive events is that they are seismic signals from shallow volcanic earthquakes which have coupled into the water column. As noted by Hanson et al. [2001], T-phases from tectonic earthquakes are generally minutes in duration, and band-limited from 2-40 Hz. Although our impulsive hydroacoustic swarm signals are limited to approximately this same band, they lack the duration of tectonic earthquakes. Volcanic earthquakes can be much shallower and transmit energy efficiently to T-phases, resulting in generally much shorter event duration. This could be a viable possibility based on the band-limited spectra, short duration, and lack of discolored water at Anak Krakatau. Additional analysis from local seismic arrays could help distinguish between volcanic earthquake, volcanic explosion, or magmatic gas bubble burst sources.

Based on the variability in shape and duration of the waveform families, it is possible that any or all of these processes were occurring within the same timeframe. Since tectonic earthquakes are shown not to be a plausible cause of these impulsive events and a volcanic source is likely, this analysis shows that remote hydroacoustic signal analysis may be useful in identifying volcanic events that were not flagged by other geophysical methods.

Conclusion

To add an additional case study to this emerging field, we used hydroacoustic data from IMS stations H08S and H01W, as well as infrasound data from IMS stations IS06, IS07, and IS52, to study the chronology and characteristics of 2018-2019 eruptive activity at Anak Krakatau. Waveform and spectrograms were analyzed for these stations and PMCC array processing was conducted from June 2018 through January 2019 to determine velocity and propagation direction of detected signals. By examining detections since the start of the new eruptive phase in June 2018, the hydroacoustic stations detected a hydroacoustic swarm indicative of submarine eruption activity from November 29 through December 11, 2018, which to our knowledge is a new contribution to the characterization of this eruption. The hydroacoustic stations did not detect the climactic eruption phase and major flank collapse, indicating that this part of the eruption was primarily subaerial or that the signal to noise ratio was too low to resolve this event. Eruption activity was also detected at infrasound station IS06, overlapping with the hydroacoustic swarm, but with a shorter duration indicating the eruption may have evolved from having both submarine and subaerial components to becoming entirely subaerial in that time. Infrasound events from the climactic eruption phase timeframe were picked using an STA/LTA with PMCC cross-check method, and hydroacoustic events were picked manually. We used these events to conduct waveform cross-correlation simi-

larity analysis, by clustering similar waveforms into multiplets and then families above a cross-correlation threshold. The infrasound events were impulsive and highly repetitive, indicating the presence of one or more sources of repeating explosions at the volcano, consistent with eyewitness reports of intense Strombolian and Surtseyan activity. The hydroacoustic events were less well correlated, with a few moderate sized event families. Their generally 1-40 Hz band-limited character and short durations have several possible interpretations, including earthquakes generated by volcanic activity, discrete phreatomagmatic explosions, or bursting magmatic gas bubbles at a submarine vent on the volcanic flank. Relationships such as these between source mechanisms and generated seismo-acoustic signal may be of future utility in the design of systems to automatically detect submarine volcanism, to warn ships and aircraft of possible volcanic hazards. Automated detection of intense eruption or flank collapse signals could also be added to existing tsunami early warning systems to improve their volcanogenic tsunami detection capability, to target volcanic eruptions as possible tsunami sources in addition to earthquake sources [Strunz et al., 2011]. These findings highlight the role that remote infrasound and hydroacoustic technology can play in the detection and characterization of eruptive activity at submarine and partially submerged volcanoes.

Bibliography

- Alyotech (2014). User Manual of PMCC 4.3.
- Auker, M. R., Sparks, R. S. J., Siebert, L., Crossweller, H. S., and Ewert, J. (2013). A statistical analysis of the global historical volcanic fatalities record. *Journal of Applied Volcanology*, 2(1):1–24.
- Balachandran, N. K. and Donn, W. L. (1971). Characteristics of Infrasonic Signals from Rockets. *Geophysical Journal of the Royal Astronomical Society*, 26(1-4):135–148.
- Beyreuther, M., Barsch, R., Krischer, L., Megies, T., Behr, Y., and Wassermann, J. (2010). ObsPy: A Python Toolbox for Seismology. *Seismological Research Letters*, 83(3):530–533.
- Bohnenstiehl, D. R., Dziak, R. P., Matsumoto, H., and Lau, T.-K. A. (2012). Underwater acoustic records from the March 2009 eruption of Hunga Ha’apai-Hunga Tonga volcano in the Kingdom of Tonga. *Journal of Volcanology and Geothermal Research*.
- Campus, P. and Christie, D. (2010). Worldwide Observations of Infrasonic Waves. In *Infrasound Monitoring for Atmospheric Studies*, pages 185–234. Springer Science + Business Media.
- Cansi, Y. (1995). An automatic seismic event processing for detection and location: the P.M.C.C. method. *Geophysical Research Letters*, 22(9):1021–1024.
- Cansi, Y. and Klinger, Y. (1997). An automated data processing method for mini-arrays.
- Caplan-Auerbach, J., Fox, C. G., and Duennebier, K. (2001). Detection of submarine landslides on Kilauea volcano. *Geophysical Research Letters*, 28(9):1811–1813.
- Caplan-Auerbach, J. and Duennebier, F. (2001). Seismic and acoustic signals detected at Loihi seamount by the hawaii. *Geochemistry Geophysics Geosystems*, 2(5).
- Carey, R., Adam Soule, S., Manga, M., White, J. D., McPhie, J., Wysoczanski, R., Jutzeler, M., Tani, K., Yoerger, D., Fornari, D., Caratori-Tontini, F., Houghton, B., Mitchell, S., Ikegami, F., Conway, C., Murch, A., Fauria, K., Jones, M., Cahalan, R., and McKenzie, W. (2018). The largest deep-ocean silicic volcanic eruption of the past century. *Science Advances*, 4(1):1–7.

- Chadwick, W. W., Cashman, K. V., Embley, R. W., Matsumoto, H., Dziak, R. P., de Ronde, C. E., Lau, T. K., Deardorff, N. D., and Merle, S. G. (2008). Direct video and hydrophone observations of submarine explosive eruptions at NW Rota-1 volcano, Mariana arc. *Journal of Geophysical Research: Solid Earth*, 113(8):1–23.
- Christie, D. and Campus, P. (2010). The IMS Infrasound Network: Design and Establishment of Infrasound Stations. In *Infrasound Monitoring for Atmospheric Studies*, chapter 2, pages 29–75. Springer.
- Committee on Potential Impacts of Ambient Noise in the Ocean on Marine Mammals, N. R. C. (2003). *Ocean Noise and Marine Mammals*. National Academy of Sciences, Washington D.C.
- Coombs, M., Wallace, K., Cameron, C., Lyons, J., Wech, A., Angeli, K., and Cervelli, P. (2019). Overview, chronology, and impacts of the 2016–2017 eruption of Bogoslof volcano, Alaska. *Bulletin of Volcanology*, 81(11).
- Dabrowa, A. L., Green, D. N., Rust, A. C., and Phillips, J. C. (2011). A global study of volcanic infrasound characteristics and the potential for long-range monitoring. *Earth and Planetary Science Letters*, 310(3-4):369–379.
- Dahren, B., Troll, V. R., Andersson, U. B., Chadwick, J. P., Gardner, M. F., Jaxybulatov, K., and Koulakov, I. (2011). Magma plumbing beneath Anak Krakatau volcano, Indonesia: evidence for multiple magma storage regions. *Contributions to Mineralogy and Petrology*, (163):631–651.
- Davy, C., Barruol, G., Fontaine, F. R., Sigloch, K., and Stutzmann, E. (2014). Tracking major storms from microseismic and hydroacoustic observations on the seafloor. *Geophysical Research Letters*, 41(24):8825–8831.
- de Groot-Hedlin, C., Hedlin, M., and Drob, D. (2010). Atmospheric Variability and Infrasound Monitoring. In *Infrasound Monitoring for Atmospheric Studies*, chapter 15, pages 475–509. Springer.
- de Groot-Hedlin, C. D. (2020). Seismic T-Wave Observations at Dense Seismic Networks. *Seismological Research Letters*.
- Denes, S. L., Warner, G., Austin, M. E., and Macgillivray, A. (2016). Hydroacoustic Pile Driving Noise Study - Comprehensive Report Document 001285, Version 2.0. Technical report, U.S. Department of Transportation, Federal Highway Administration.
- Dietz, R. and Sheehy, M. (1954). Transpacific detection of Myojin volcanic explosions by underwater sound. *Bulletin of the Geological Society of America*, 55:941–956.
- Donn, W. L. (1978). Exploring the atmosphere with sonic booms. *American Scientist*, 66(6):724–733.

- Drob, D. P., Garcés, M., Hedlin, M., and Brachet, N. (2010). The temporal morphology of infrasound propagation. *Pure and Applied Geophysics*, 167(4-5):437–453.
- D’Vincent, C. G., Nilson, R. M., and Hanna, R. E. (1985). Vocalization and coordinated feeding behavior of the humpback whale *Megaptera novaeangliae* in Southeastern Alaska, USA. *Scientific Reports of the Whale Research Institute Tokyo*, 36(36):41–47.
- Dziak, R. P. and Fox, C. G. (1999). The January 1998 earthquake swarm at axial volcano, Juan de Fuca ridge: Hydroacoustic evidence of seafloor volcanic activity. *Geophysical Research Letters*, 26(23):3429–3432.
- Dziak, R. P. and Fox, C. G. (2002a). Evidence of harmonic tremor from a submarine volcano detected across the Pacific Ocean basin. *Journal of Geophysical Research*, 107(B5):2085.
- Dziak, R. P. and Fox, C. G. (2002b). Evidence of harmonic tremor from a submarine volcano detected in the Pacific Ocean basin. *Article in Journal of Geophysical Research Atmospheres*.
- Dziak, R. P., Bohnenstiehl, D. R., Baker, E. T., Matsumoto, H., Caplan-Auerbach, J., Embley, R. W., Merle, S. G., Walker, S. L., Lau, T. K., and Chadwick, W. W. (2015). Long-term explosive degassing and debris flow activity at West Mata submarine volcano. *Geophysical Research Letters*, 42(5):1480–1487.
- Evers, L. G. and Haak, H. W. (2001). Listening to sounds from an exploding meteor and oceanic waves. *Geophysical Research Letters*, 28(1):41–44.
- Evers, L. G. and Haak, H. W. (2010). The Characteristics of Infrasound, its Propagation and Some Early History. In *Infrasound Monitoring for Atmospheric Studies*, chapter 1, pages 3–27. Springer.
- Evers, L. G., Green, D. N., Young, N. W., and Snellen, M. (2013). Remote hydroacoustic sensing of large icebergs in the southern Indian Ocean: Implications for iceberg monitoring. *Geophysical Research Letters*, 40(17):4694–4699.
- Ewing, M. and Worzel, J. L. (1948). Long-range sound transmission. *Memoir of the Geological Society of America*, 27:1–32.
- Fee, D., Garcés, M., and Steffke, A. (2010). Infrasound from Tungurahua Volcano 2006–2008: Strombolian to Plinian eruptive activity. *Journal of Volcanology and Geothermal Research*, 193(1-2):67–81.
- Fee, D., Matoza, R. S., Gee, K. L., Neilsen, T. B., and Ogden, D. E. (2013). Infrasonic crackle and supersonic jet noise from the eruption of Nabro Volcano, Eritrea. *Geophysical Research Letters*, 40(16):4199–4203.

- Garcés, M., Hetzer, C., Merrifield, M., Willis, M., and Aucan, J. (2003). Observations of surf infrasound in Hawai'i. *Geophysical Research Letters*, 30(24):3–5.
- Garcés, M., Willis, M., Hetzer, C., Le Pichon, A., and Drob, D. (2004). On using ocean swells for continuous infrasonic measurements of winds and temperature in the lower, middle, and upper atmosphere. *Geophysical Research Letters*, 31(19):1–4.
- Garces, M., Willis, M., and Le Pichon, A. (2010). Infrasonic Observations of Open Ocean Swells in the Pacific: Deciphering the Song of the Sea. In Le Pichon, A., Blanc, E., and Hauchecorne, A., editors, *Infrasound Monitoring for Atmospheric Studies*, pages 235–248. Springer, Dordrecht.
- Georges, T. M. and Beasley, W. H. (1977). Refraction of infrasound by upper-atmospheric winds. *Journal of the Acoustical Society of America*, 61(1):28–34.
- Giachetti, T., Paris, R., Kelfoun, K., and Ontowirjo, B. (2012). Tsunami hazard related to a flank collapse of Anak Krakatau Volcano, Sunda Strait, Indonesia. *Geological Society Special Publication*, 361(1):79–90.
- Global Volcanism Program (1972). Card 1466 (16 October 1972).
- Global Volcanism Program (1986). Report on Additional Reports (Unknown) (McClelland, L., ed.).
- Global Volcanism Program (2011). Report on Krakatau (Indonesia) - August 2011. *Bulletin of the Global Volcanism Network*.
- Global Volcanism Program (2012). Report on Krakatau (Indonesia) - December 2012. *Bulletin of the Global Volcanism Network*, 37(12).
- Global Volcanism Program (2013). Volcanoes of the World, v. 4.9.0 (04 Jun 2020).
- Global Volcanism Program (2017). Report on Krakatau (Indonesia) (Venzke, E., ed.). *Bulletin of the Global Volcanism Network*, 42(9).
- Global Volcanism Program (2018a). Report on Krakatau (Indonesia) (Crafford, A.E., and Venzke, E., eds.). *Bulletin of the Global Volcanism Network*, 43(10).
- Global Volcanism Program (2018b). Report on Krakatau (Indonesia). In: Sennert, S K (ed.), Weekly Volcanic Activity Report, 28 November-4 December 2018.
- Global Volcanism Program (2018c). Report on Krakatau (Indonesia). In: Sennert, S K (ed.), Weekly Volcanic Activity Report, 5 December-11 December 2018.
- Global Volcanism Program (2019). *Report on Krakatau (Indonesia) (Krippner, J.B., and Venzke, E., eds.)*, volume 44.

- Global Volcanism Program (2020). Report on Krakatau (Indonesia). In: Sennert, S K (ed.), Weekly Volcanic Activity Report, 8 April-14 April 2020. Technical report, Smithsonian Institution and US Geological Survey.
- Green, D. N. and Neuberg, J. (2006). Waveform classification of volcanic low-frequency earthquake swarms and its implication at Soufrière Hills Volcano, Montserrat. *Journal of Volcanology and Geothermal Research*, 153(1-2):51–63.
- Green, D. N., Matoza, R. S., Vergoz, J., and Le Pichon, A. (2012). Infrasonic propagation from the 2010 Eyjafjallajkull eruption: Investigating the influence of stratospheric solar tides. *Journal of Geophysical Research Atmospheres*, 117(21):1–19.
- Green, D. N., Evers, L. G., Fee, D., Matoza, R. S., Snellen, M., Smets, P., and Simons, D. (2013). Hydroacoustic, infrasonic and seismic monitoring of the submarine eruptive activity and sub-aerial plume generation at South Sarigan, May 2010. *Journal of Volcanology and Geothermal Research*, 257:31–43.
- Grover, F. H. (1968). A Note on Infrasonics at U.K.A.E.A. Blacknest. *Geophysical Journal of the Royal Astronomical Society*, 16(3):311–315.
- Guilbert, J., Vergoz, J., Schisselé, E., Roueff, A., and Cansi, Y. (2005). Use of hydroacoustic and seismic arrays to observe rupture propagation and source extent of the Mw = 9.0 Sumatra earthquake. *Geophysical Research Letters*, 32(15).
- Hanson, J., Le Bras, R., Dysart, P., Brumbaugh, D., Gault, A., and Guern, J. (2001). Operational Processing of Hydroacoustics at the Prototype International Data Center. *Pure and Applied Geophysics*, 158(3):425–456.
- Hedin, A. E., Fleming, E. L., Manson, A. H., Schmidlin, F. J., Avery, S. K., Clark, R. R., Franke, S. J., Fraser, G. J., Tsuda, T., Vial, F., and Vincent, R. A. (1996). Empirical wind model for the upper, middle and lower atmosphere. *Journal of Atmospheric and Terrestrial Physics*, 58(13):1421–1447.
- Heinrich, P., Boudon, G., Komorowski, J. C., Sparks, R. S. J., Herd, R., and Voighp, B. (2001). Numerical simulation of the December 1997 debris avalanche in Montserrat, Lesser Antilles. *Geophysical Research Letters*, 28(13):2529–2532.
- Helo, C., Longpré, M.-A., Shimizu, N., Clague, D. A., and Stix, J. (2011). Explosive eruptions at mid-ocean ridges driven by CO₂-rich magmas. *Nature Geoscience*, 4:260–263.
- Hildebrand, J. A. (2009). Anthropogenic and natural sources of ambient noise in the ocean. *Marine Ecology Progress Series*, 395:5–20.
- Jensen, F. B., Kuperman, W. A., Porter, M. B., and Schmidt, H. (2011). *Computational Ocean Acoustics*. Springer New York Dordrecht Heidelberg London, second edition.

- Johnson, R. and Norris, R. (1968). Geographic variation of Sofar speed and axis depth in the Pacific Ocean. *Journal of Geophysical Research*.
- Jutzeler, M., Marsh, R., Carey, R. J., White, J. D. L., Talling, P. J., and Karlstrom, L. (2014). On the fate of pumice rafts formed during the 2012 Havre submarine eruption. *Nature Communications*, 5(1):3660.
- Kulichkov, S. N. (2004). Long-range propagation and scattering of low-frequency sound pulses in the middle atmosphere. *Meteorology and Atmospheric Physics*, 85(1-3):47–60.
- Lawrence, M. W. (2004). Acoustic Monitoring of the Global Ocean for the CTBT. Technical Report November, Comprehensive Nuclear-Test-Ban Treaty Organisation.
- Le Pichon, A. and Cansi, Y. (2003). PMCC for Infrasound Data Processing.
- Le Pichon, A., Ceranna, L., Garcés, M., Drob, D., and Millet, C. (2006). On using infrasound from interacting ocean swells for global continuous measurements of winds and temperature in the stratosphere. *Journal of Geophysical Research Atmospheres*, 111(11):1–7.
- Le Pichon, A., Vergoz, J., Blanc, E., Guilbert, J., Ceranna, L., Evers, L., and Brächet, N. (2009). Assessing the performance of the International Monitoring System’s infrasound network: Geographical coverage and temporal variabilities. *Journal of Geophysical Research Atmospheres*, 114(8):25–28.
- Le Pichon, A., Matoza, R. S., Brächet, N., and Cansi, Y. (2010). Recent enhancements of the PMCC infrasound signal detector.
- Liszka, L. (1974). Long-distance propagation of infrasound from artificial sources. *Journal of the Acoustical Society of America*, 56(5):1383–1388.
- Lyons, J. J., Iezzi, A. M., Fee, D., Schwaiger, H. F., Wech, A. G., and Haney, M. M. (2020). Infrasound generated by the 2016–2017 shallow submarine eruption of Bogoslof volcano, Alaska. *Bulletin of Volcanology*, 82(2).
- Manga, M., Fauria, K. E., Lin, C., Mitchell, S. J., Jones, M., Conway, C. E., Degruyter, W., Hosseini, B., Carey, R., Cahalan, R., Houghton, B. F., White, J. D., Jutzeler, M., Soule, S. A., and Tani, K. (2018). The pumice raft-forming 2012 Havre submarine eruption was effusive. *Earth and Planetary Science Letters*, 489:49–58.
- Masson, D. G., Harbitz, C. B., Wynn, R. B., Pedersen, G., and Løvholt, F. (2006). Submarine landslides: Processes, triggers and hazard prediction. *Philosophical Transactions of the Royal Society A: Mathematical, Physical and Engineering Sciences*, 364(1845):2009–2039.
- Mastin, L. and Witter, J. (2000). The hazards of eruptions through lakes and seawater. *Journal of Volcanology and Geothermal Research*, 97(1-4):195–214.

- Matoza, R. S., Hedlin, M. A., and Garcés, M. A. (2007). An infrasound array study of Mount St. Helens. *Journal of Volcanology and Geothermal Research*.
- Matoza, R. S. and Chouet, B. A. (2010). Subevents of long-period seismicity: Implications for hydrothermal dynamics during the 2004-2008 eruption of Mount St. Helens. *Journal of Geophysical Research: Solid Earth*, 115(B12206).
- Matoza, R. S., Le Pichon, A., Vergoz, J., Herry, P., Lalande, J. M., il Lee, H., Che, I. Y., and Rybin, A. (2011a). Infrasonic observations of the June 2009 Sarychev Peak eruption, Kuril Islands: Implications for infrasonic monitoring of remote explosive volcanism. *Journal of Volcanology and Geothermal Research*, 200(1-2):35–48.
- Matoza, R. S., Vergoz, J., Le Pichon, A., Ceranna, L., Green, D. N., Evers, L. G., Ripepe, M., Campus, P., Liszka, L., Kvaerna, T., Kjartansson, E., and Höskuldsson, Á. (2011b). Long-range acoustic observations of the Eyjafjallajkull eruption, Iceland, April-May 2010. *Geophysical Research Letters*, 38(6):1–5.
- Matoza, R. S., Landès, M., Le Pichon, A., Ceranna, L., and Brown, D. (2013). Coherent ambient infrasound recorded by the International Monitoring System. *Geophysical Research Letters*, 40(2):429–433.
- Matoza, R. S., Green, D. N., Le Pichon, A., Shearer, P. M., Fee, D., Mialle, P., and Ceranna, L. (2017). Automated detection and cataloging of global explosive volcanism using the International Monitoring System infrasound network. *Journal of Geophysical Research: Solid Earth*, 122(4):2946–2971.
- Matoza, R. S., Fee, D., Green, D. N., Le Pichon, A., Vergoz, J., Haney, M. M., Mikesell, T. D., Franco, L., Valderrama, O. A., Kelley, M. R., McKee, K., and Ceranna, L. (2018). Local, Regional, and Remote Seismo-acoustic Observations of the April 2015 VEI 4 Eruption of Calbuco Volcano, Chile. *Journal of Geophysical Research: Solid Earth*, 123(5):3814–3827.
- Matoza, R. S., Fee, D., Green, D. N., and Mialle, P. (2019). Volcano Infrasound and the International Monitoring System. In *Infrasound Monitoring for Atmospheric Studies*, chapter 33, pages 1023–1077. Springer International Publishing.
- McCauley, R. D., Day, R. D., Swadling, K. M., Fitzgibbon, Q. P., Watson, R. A., and Semmens, J. M. (2017). Widely used marine seismic survey air gun operations negatively impact zooplankton. *Nature Ecology and Evolution*, 1(7):1–8.
- McDonald, M. A., Hildebrand, J. A., and Wiggins, S. M. (2006). Increases in deep ocean ambient noise in the Northeast Pacific west of San Nicolas Island, California. *The Journal of the Acoustical Society of America*, 120(2):711–718.
- Medwin, H. (1975). Speed of sound in water: A simple equation for realistic parameters. *The Journal of the Acoustical Society of America*, 58(No. 6):1318–1319.

- Metz, D., Watts, A. B., Grevemeyer, I., Rodgers, M., and Paulatto, M. (2016). Ultra-long-range hydroacoustic observations of submarine volcanic activity at Monowai, Kermadec Arc. *Geophysical Research Letters*, 43(4):1529–1536.
- Modified Copernicus Sentinel Data (2019). 2018-2019, Sentinel Hub.
- Moore, J. G., Nakamura, K., and Alcaraz, A. (1966). The 1965 Eruption of Taal Volcano. *American Association for the Advancement of Science*, 151(3713):955–960.
- Moore, J. G. (1967). Base Surge in Recent Volcanic Eruptions*. *Volcanological Bulletin*, 30.
- Moore, J. G., Clague, D. A., Holcomb, R. T., Lipman, P. W., Normark, W. R., and Torresan, M. E. (1989). Prodigious submarine landslides on the Hawaiian Ridge. *Journal of Geophysical Research*, 94(B12).
- Muhari, A., Heidarzadeh, M., Susmoro, H., Nugroho, H. D., Kriswati, E., Supartoyo, Wijanarto, A. B., Imamura, F., and Arikawa, T. (2019). The December 2018 Anak Krakatau Volcano Tsunami as Inferred from Post-Tsunami Field Surveys and Spectral Analysis. *Pure and Applied Geophysics*, 176(12):5219–5233.
- Munk, W. H. (1974). Sound channel in an exponentially stratified ocean, with application to SOFAR. *The Journal of the Acoustical Society of America*, 55(220).
- Mutschlecner, J., Whitaker, R., and Auer, L. (1999). An Empirical Study of Infraonic Propagation.
- Mutschlecner, J. and Whitaker, R. (2010). Some Atmospheric Effects on Infrasound Signal Amplitudes. In *Infrasound Monitoring for Atmospheric Studies*, chapter 14, pages 455–453. Springer.
- Nieukirk, S. L., Mellinger, D. K., Moore, S. E., Klinck, K., Dziak, R. P., and Goslin, J. (2012). Sounds from airguns and fin whales recorded in the mid-Atlantic Ocean, 1999–2009. *The Journal of the Acoustical Society of America*, 131(2):1102–1112.
- NOAA, NASA, and Force, U. A. (1976). *U.S. Standard Atmosphere*. U.S. Government Publishing Office, Washington D.C.
- Norris, R. and Johnson, R. (1969). Submarine Volcanic Eruptions Recently Located in the Pacific By Sofar Hydrophones. *Journal of Geophysical Research*, 74(2):650–664.
- Oshima, S., Tsuchide, M., Kato, S., Okubo, S., Watanabe, K., Kudo, K., and Ossaka, J. (1991). Birth of a Submarine Volcano “Teisi Knoll”. *Journal of Physics of the Earth*, 39(1):1–19.

- Paris, R., Switzer, A. D., Belousova, M., Belousov, A., Ontowirjo, B., Whelley, P. L., and Ulvrova, M. (2014). Volcanic tsunami: A review of source mechanisms, past events and hazards in Southeast Asia (Indonesia, Philippines, Papua New Guinea). *Natural Hazards*, 70(1):447–470.
- Parsons, E. C. M. (2017). Impacts of Navy Sonar on Whales and Dolphins: Now beyond a Smoking Gun? *Frontiers in Marine Science*, 4(295).
- Payne, K. B., Langbauer, W. R., and Thomas, E. M. (1986). Infrasonic calls of the Asian elephant (*Elephas maximus*). *Behavioral Ecology and Sociobiology*, 18(4):297–301.
- Perttu, A., Caudron, C., Assink, J. D., Metz, D., Tailpied, D., Perttu, B., Hibert, C., Nurfiani, D., Pilger, C., Muzli, M., Fee, D., Andersen, O. L., and Taisne, B. (2020). Reconstruction of the 2018 tsunamigenic flank collapse and eruptive activity at Anak Krakatau based on eyewitness reports, seismo-acoustic and satellite observations. *Earth and Planetary Science Letters*, 541:116268.
- Petersen, T. (2007). Swarms of repeating long-period earthquakes at Shishaldin Volcano, Alaska, 2001-2004. *Journal of Volcanology and Geothermal Research*, 166(3-4):177–192.
- Picone, J. M., Hedin, A. E., Drob, D. P., and Aikin, A. C. (2002). NRLMSISE-00 empirical model of the atmosphere: Statistical comparisons and scientific issues. *Journal of Geophysical Research: Space Physics*, 107(A12):1–16.
- Przedpelski, Z. J. and Casadevall, T. J. (1991). Volcanic Ash and Aviation Safety: Proceedings of the First International Symposium on Volcanic Ash Aviation Safety, July 1991. *U.S. Geological Survey Bulletin*, 2047.
- Pusat Vulkanologi dan Mitigasi Bencana Geologi (2018). Daily Geologic Disaster Reports (in Indonesian).
- PVMBG via Detik News (2018). PVMBG: Gunung Krakatau Meletus 423 Kali (In Indonesian).
- Resing, J. A., Rubin, K. H., Embley, R. W., Lupton, J. E., Baker, E. T., Dziak, R. P., Baumberger, T., Lilley, M. D., Huber, J. A., Shank, T. M., Butterfield, D. A., Clague, D. A., Keller, N. S., Merle, S. G., Buck, N. J., Michael, P. J., Soule, A., Caress, D. W., Walker, S. L., Davis, R., Cowen, J. P., Reysenbach, A. L., and Thomas, H. (2011). Active submarine eruption of boninite in the northeastern Lau Basin. *Nature Geoscience*, 4(11):799–806.
- Ripepe, M., Marchetti, E., Delle Donne, D., Genco, R., Innocenti, L., Lacanna, G., and Valade, S. (2018). Infrasonic Early Warning System for Explosive Eruptions. *Journal of Geophysical Research: Solid Earth*, 123(11):9570–9585.

- Rose, G. A. and Leggett, W. C. (1988). Hydroacoustic Signal Classification of Fish Schools by Species. *Canadian Journal of Fisheries and Aquatic Sciences*, 45(4):597–604.
- Seiner, J. M. (1984). Advances In High Speed Jet Aeroacoustics. *AIAA/NASA 9th Aeroacoustics Conference*.
- Self, S. and Rampino, M. R. (1981). The 1883 eruption of Krakatau. *Nature*, 294(5843):699–704.
- Sigurdsson, H., Carey, S., Mandeville, C., and Bronto, S. (1991). Pyroclastic flows of the 1883 Krakatau eruption. *Eos, Transactions American Geophysical Union*, 72(36):377–381.
- Simpson, S. D., Radford, A. N., Nedelec, S. L., Ferrari, M. C., Chivers, D. P., McCormick, M. I., and Meekan, M. G. (2016). Anthropogenic noise increases fish mortality by predation. *Nature Communications*, 7.
- Snodgrass, J. M. and Richards, A. F. (1956). Observations of underwater volcanic acoustics at Bárcena Volcano, San Benedicto Island, Mexico, and in Shelikof Strait, Alaska. *Transactions, American Geophysical Union*, 37(1):97–104.
- Stehn, C. (1929). The geology and volcanism of the Krakatau group. In *Proc Fourth Pacific Sci Congress*, pages 1–55, Batavia.
- Stephens, C. D. and Chouet, B. A. (2001). Evolution of the December 14, 1989 precursory long-period event swarm at Redoubt volcano, Alaska. *Journal of Volcanology and Geothermal Research*, 109(1-3):133–148.
- Strunz, G., Post, J., Zosseder, K., Wegscheider, S., Mück, M., Riedlinger, T., Mehl, H., Dech, S., Birkmann, J., Gebert, N., Harjono, H., Anwar, H. Z., Sumaryono, Khomarudin, R. M., and Muhari, A. (2011). Tsunami risk assessment in Indonesia. *Natural Hazards and Earth System Science*, 11(1):67–82.
- Sutherland, L. C. and Bass, H. E. (2004). Atmospheric absorption in the atmosphere up to 160 km. *The Journal of the Acoustical Society of America*, 115(3):1012–1032.
- Talandier, J. and Kuster, G. (1976). Seismicity and submarine volcanic activity in French Polynesia. *Journal of Geophysical Research*, 81(5):936–948.
- Talandier, J. and Okal, E. A. (1984). The volcanoseismic swarms of 1981-1983 in the Tahiti-Mehetia area, French Polynesia. *Journal of Geophysical Research*, 89(B13):11216–11234.
- Talandier, J. and Okal, E. A. (1987). Seismic detection of underwater volcanism: The example of French Polynesia. *Pure and Applied Geophysics*, 125(6):919–950.

- Talandier, J. and Okal, E. A. (2001). Identification criteria for sources of T waves recorded in French polynesia. *Pure and Applied Geophysics*, 158(3):567–603.
- Tepp, G., Chadwick, W. W., Haney, M. M., Lyons, J. J., Dziak, R. P., Merle, S. G., Butterfield, D. A., and Young, C. W. (2019a). Hydroacoustic, Seismic, and Bathymetric Observations of the 2014 Submarine Eruption at Ahiy Seamount, Mariana Arc. *Geochemistry, Geophysics, Geosystems*, pages 3608–3627.
- Tepp, G., Dziak, R. P., Haney, M. M., Lyons, J. J., Searcy, C., Matsumoto, H., and Haxel, J. (2019b). Seismic and hydroacoustic observations of the 2016–17 Bogoslof eruption. *Bulletin of Volcanology*, 82(1).
- Thorarinsson, S. (1967). The Surtsey eruption and related scientific work. *Polar Record*, 13(86):571–578.
- Tolstoy, I. and Ewing, M. (1950). The T phase of shallow-focus earthquakes. Technical Report 1.
- Trofimovs, J., Sparks, R. S. J., and Talling, P. J. (2008). Anatomy of a submarine pyroclastic flow and associated turbidity current: July 2003 dome collapse, Soufrière Hills volcano, Montserrat, West Indies. *Sedimentology*, 55(3):617–634.
- Ulivieri, G., Ripepe, M., and Marchetti, E. (2013). Infrasound reveals transition to oscillatory discharge regime during lava fountaining: Implication for early warning. *Geophysical Research Letters*, 40(12):3008–3013.
- UNCTAD (2015). Review of Maritime Transport 2015. Technical report, United Nations.
- Urlick, R. J. (1984). Ambient Noise in the Sea. Technical Report 5, Undersea Warfare Technology Office, Naval Sea Systems Command, Department of the Navy.
- Walter, T. R., Haghshenas Haghighi, M., Schneider, F. M., Coppola, D., Motagh, M., Saul, J., Babeyko, A., Dahm, T., Troll, V. R., Tilmann, F., Heimann, S., Valade, S., Triyono, R., Khomarudin, R., Kartadinata, N., Laiolo, M., Massimetti, F., and Gaebler, P. (2019). Complex hazard cascade culminating in the Anak Krakatau sector collapse. *Nature Communications*, 10(1).
- Waxler, R. and Gilbert, K. E. (2006). The radiation of atmospheric microbaroms by ocean waves. *The Journal of the Acoustical Society of America*, 119(5):2651–2664.
- White, J. D., Schipper, C. I., and Kano, K. (2015). *Submarine Explosive Eruptions*. Elsevier Inc., second edi edition.
- White, J. D. L., Smellie, J., and Clague, D. (2003). Introduction: A Deductive Outline and Topical Overview of Subaqueous Explosive Volcanism. *Geophysical Monograph Series*.

- Williams, R., Rowley, P., and Garthwaite, M. C. (2019). Reconstructing the Anak Krakatau flank collapse that caused the December 2018 Indonesian tsunami. *Geology*, 47(10):973–976.
- Ye, L., Kanamori, H., Rivera, L., Lay, T., Zhou, Y., Sianipar, D., and Satake, K. (2020). The 22 December 2018 tsunami from flank collapse of Anak Krakatau volcano during eruption. *Science Advances*, 6(3):1–10.
- Yokoyama, I. (1981). A geophysical interpretation of the 1883 Krakatau eruption. *Journal of Volcanology and Geothermal Research*, 9(4):359–378.